REPORT DOCUMENTATION PAGE

Form Approved OMB NO. 0704-0188

1. REPORT DATE (DD-MM-YYYY)	2. REPORT TYPE	3. DATES COVERED (From - To)
05-01-2016	Final Report	15-Jun-2009 - 14-Jun-2015

4. TITLE AND SUBTITLE
Final Report: The Effects of Toxic Particles in Human Lung Cells - RESEARCH AREA 8. Life Sciences

5a. CONTRACT NUMBER
W911NF-09-1-0296

5b. GRANT NUMBER

5c. PROGRAM ELEMENT NUMBER
611102

6. AUTHORS
John Pierce Wise, Sr

5d. PROJECT NUMBER

5e. TASK NUMBER

5f. WORK UNIT NUMBER

7. PERFORMING ORGANIZATION NAMES AND ADDRESSES
University of Southern Maine
P.O. Box 9300
96 Falmouth St.
Portland, ME 04104 -9300

8. PERFORMING ORGANIZATION REPORT NUMBER

9. SPONSORING/MONITORING AGENCY NAME(S) AND ADDRESS (ES)
U.S. Army Research Office
P.O. Box 12211
Research Triangle Park, NC 27709-2211

10. SPONSOR/MONITOR'S ACRONYM(S)
ARO

11. SPONSOR/MONITOR'S REPORT NUMBER(S)
56448-LS.43

12. DISTRIBUTION AVAILIBILITY STATEMENT
Approved for Public Release; Distribution Unlimited

13. SUPPLEMENTARY NOTES
The views, opinions and/or findings contained in this report are those of the author(s) and should not contrued as an official Department of the Army position, policy or decision, unless so designated by other documentation.

14. ABSTRACT
Six interrelated aims were investigated in this project: 1) Characterize metal nanoparticles; 2) Determine metal particle cytotoxicity in human lung cells; 3) Demonstrate metal particle genotoxicity; 4) Characterize metal particle-induced chromosome instability; 5) Compare silver and gold nanoparticle-induced effects; and 6) Assess metal levels in whale skin biopsies in the Gulf of Mexico. The first five aims focused on three categories of metal particles; nanoparticles, particles associated with metal-on-metal hip implants and microparticles of military concern. We found that silver, gold and titanium dioxide nanoparticles were relatively non-toxic. Only silver

15. SUBJECT TERMS
Final Report, Toxic Particles

16. SECURITY CLASSIFICATION OF:			17. LIMITATION OF ABSTRACT	15. NUMBER OF PAGES	19a. NAME OF RESPONSIBLE PERSON
a. REPORT	b. ABSTRACT	c. THIS PAGE			John Wise
UU	UU	UU	UU		19b. TELEPHONE NUMBER: 207-228-8050

Report Title

Final Report: The Effects of Toxic Particles in Human Lung Cells - RESEARCH AREA 8. Life Sciences

ABSTRACT

Six interrelated aims were investigated in this project: 1) Characterize metal nanoparticles; 2) Determine metal particle cytotoxicity in human lung cells; 3) Demonstrate metal particle genotoxicity; 4) Characterize metal particle-induced chromosome instability; 5) Compare silver and gold nanoparticle-induced effects; and 6) Assess metal levels in whale skin biopsies in the Gulf of Mexico. The first five aims focused on three categories of metal particles; nanoparticles, particles associated with metal-on-metal hip implants and microparticles of military concern. We found that silver, gold and titanium dioxide nanoparticles were relatively non-toxic. Only silver nanoparticles induced cytotoxicity after 120 h exposure time. None of the nanoparticles were genotoxic. Nanoparticles associated with metal-on-metal (CrCoMb) hip implants were found to be somewhat cytotoxic and genotoxic. However their component parts, chromium and cobalt, were found to be both cytotoxic and genotoxic and to induce chromosome instability. Molybdenum was not cytotoxic. We also considered micro-particles of military concern, including nickel, cobalt and depleted uranium (DU). We observed significant cytotoxic and genotoxic effects from all of these particles. More specifically, we found that homologous recombination repair plays a significant role in DU-induced damage. Finally, we measured metal levels in 140 sperm whale sample from the Gulf of Mexico.

Enter List of papers submitted or published that acknowledge ARO support from the start of the project to the date of this printing. List the papers, including journal references, in the following categories:

(a) Papers published in peer-reviewed journals (N/A for none)

Received	Paper
01/05/2016 42.00	Sanjeev Kumar Kandpal, Samantha L. Otterson , Douglas W. Bousfield, David J. Neivandt , Michael D. Mason. Investigation of Laser Induced Structure formation and resultant fluorescence, Optical Materials, (04 2015): 256. doi:
04/09/2014 40.00	Amie L. Holmes, Kellie Joyce, Hong Xie, Carolyne Falank, John M. Hinz, John Pierce Wise. The impact of homologous recombination repair deficiency on depleted uranium clastogenicity in Chinese hamster ovary cells: XRCC3 protects cells from chromosome aberrations, but increases chromosome fragmentation, Mutation Research/Fundamental and Molecular Mechanisms of Mutagenesis, (04 2014): 0. doi: 10.1016 /j.mrfmmm.2014.02.001
08/29/2013 18.00	Joyce T. Au, Gary Craig, Valerie Longo, Pat Zanzonico, Michael Mason, Yuman Fong, Peter J. Allen. Gold Nanoparticles Provide Bright Long-Lasting Vascular Contrast for CT Imaging, American Journal of Roentgenology, (06 2013): 1347. doi: 10.2214/AJR.12.8933
08/30/2013 38.00	Michael M. Mason, John Pierce Wise, Hong Xie. Genotoxicity of metal nanoparticles, Reviews in Environmental Health, (01 2011): 0. doi: 10.1515/REVEH.2011.033
12/10/2013 39.00	Therry The, Amie Holmes, Kelsey Thompson, Michael Mason, Sanjeev Kandpal, Tongzhang Zheng, John Wise. Chronic Exposure to Particulate Nickel Induces Neoplastic Transformation in Human Lung Epithelial Cells, Toxics, (11 2013): 46. doi: 10.3390/toxics1010046
TOTAL:	**5**

Number of Papers published in peer-reviewed journals:

(b) Papers published in non-peer-reviewed journals (N/A for none)

Received Paper

TOTAL:

Number of Papers published in non peer-reviewed journals:

(c) Presentations

Number of Presentations: 0.00

Non Peer-Reviewed Conference Proceeding publications (other than abstracts):

Received Paper

TOTAL:

Peer-Reviewed Conference Proceeding publications (other than abstracts):

Received	Paper	
08/28/2013	22.00	Sanjeev Kumar Kandpal, Aimee Co, Kody Allcroft, Michael D. Mason, Douglas W. Bousfield, David J. Neivandt. Laser-Drawn Features on Nanoparticle Films, 2012 AiChE Annual Meeting. 28-OCT-12, . : ,
08/28/2013	23.00	Sanjeev Kumar Kandpal, Aimee Co, Kody Allcroft, Michael D. Mason, Douglas W. Bousfield, David J. Neivandt. Fluorescence Active Laser Induced Structures, 245th ACS National Meeting. 07-APR-13, . : ,
08/29/2013	25.00	John Pierce Wise, Jr, James Wise, W. Douglas Thompson, Christopher Perkins, John Pierce Wise, Sr. Is Genotoxic Metal Exposure Part of the Toxic Legacy of the Deepwater Horizon Oil Crisis? , Annual Meeting of the Society of Toxicology. 10-MAR-13, . : ,
08/29/2013	26.00	John Pierce Wise, Jr., James Wise, W. Douglas Thompson, Christopher Perkins, John Pierce Wise, Sr.. IS GENOTOXIC METAL EXPOSURE PART OF THE TOXIC LEGACYOF THE DEEPWATER HORIZON OIL CRISIS?, Annual Meeting of the International Association for Aquatic Animal Medicine. 21-APR-13, . : ,
08/29/2013	28.00	John Pierce Wise, Jr, James Wise, Christopher Perkins, W. Douglas Thompson, John Pierce Wise, Sr. Is Exposure to Genotoxic Metals Part of the Toxic Legacy of the Deepwater Horizon Oil Crisis? , Gulf of Mexico Oil Spill and Ecosystem Science Conference. 21-JAN-13, . : ,
08/29/2013	29.00	John Pierce Wise, Sr, Iain Kerr, John Pierce Wise, Jr, Catherine Wise, Sandra Wise, James Wise, Christy Gianios, Bob Wallace, Shouping Huang, Carolyne LaCerte, Amie Holmes. The Gulf of Mexico Offshore Toxicology Study. , Annual meeting of the American Association for the Advancement of Science (AAAS), . 14-FEB-13, . : ,
09/18/2014	21.00	Sanjeev Kumar Kandpal, Kody Allcroft, Michael D. Mason, Douglas W. Bousfield, David J. Neivandt. Laser-Drawn Features on Nanoparticle Films, 16th International Coating Science and Technology Symposium. 09-SEP-12, . : ,

TOTAL: **7**

Number of Peer-Reviewed Conference Proceeding publications (other than abstracts):

(d) Manuscripts

Received		Paper
07/06/2009	1.00	C. LaCerte, H. Xie, A. Aboueissa, J. Wise, Sr.. The Cytotoxicity and Clastogenicity of Particulate Depleted Uraniumin Human Lung Epithelial Cells, (07 2009)
08/31/2011	3.00	Hong Xie, John Pierce Wise, Sr.. Genotoxicity of Metal Nanoparticles, Reviews in Environmental Health (08 2011)
09/18/2014	41.00	Cynthia L. Browning, Therry The, Michael D. Mason, John Pierce Wise Sr.. Titanium Dioxide Nanoparticles Are Not Cytotoxic or Clastogenic in Human Skin Cells, Journal of Environmental and analytical toxicology (08 2014)
10/05/2009	2.00	H. Xie, C. LaCerte, J. Wise, Jr. Depleted Uranium Induces Neoplastic Transformation in Human Lung Epithelia Cells , (10 2009)
11/18/2013	19.00	Sanjeev Kumar Kandpal, Aimee Co, Kody Allcroft, David Neivandt, Douglas Bousfield, Michael Mason. Nanoparticle Derived Laser Induced Fluorescent Micro-Structures, Thin Solid Films (07 2013)
TOTAL:		**5**

Number of Manuscripts:

Books

Received		Book
08/30/2012	4.00	Edward Allgeyer, Gary Craig, Sanjeev Kandpal, Jeremy Grant, Michael Mason. "Gold Nanoparticles", In Introduction to Experimental Biophysics: Biological Methods for Physical Scientists. , Boca Raton, FL: Taylor & Francis Group , (09 2011)
09/06/2012	5.00	Anna Sitarski, Jeremy Grant, Sangeev Kandpal, Michael Mason. "Diagnostics & Treatments", In Emerging Applications of Colloidal Noble Metals in Cancer Nanomedicine. , London, UK: Future Medicine, (01 2012)
TOTAL:		**2**

Received	Book Chapter
08/30/2013	20.00 A Sitarski, Jeremy Grant, Sanjeev Kandpal, Andrew Doolittle, M Newsom, Michael Mason. Engineered Gold Nanoparticles as Contrast Agents for Biological and Medical Imaging, Hackensack, NH: World Scientific Publishing, Co., (12 2013)
TOTAL:	**1**

Patents Submitted

Patents Awarded

Awards

Graduate Students

NAME	PERCENT_SUPPORTED	Discipline
Sean Raph	0.00	
Julieta Martino	0.40	
FTE Equivalent:	**0.40**	
Total Number:	**2**	

Names of Post Doctorates

NAME	PERCENT_SUPPORTED
FTE Equivalent:	
Total Number:	

Names of Faculty Supported

NAME	PERCENT_SUPPORTED	National Academy Member
Hong Xie	0.20	
FTE Equivalent:	**0.20**	
Total Number:	**1**	

Names of Under Graduate students supported

NAME	PERCENT_SUPPORTED
FTE Equivalent:	
Total Number:	

Student Metrics

This section only applies to graduating undergraduates supported by this agreement in this reporting period

The number of undergraduates funded by this agreement who graduated during this period:	0.00
The number of undergraduates funded by this agreement who graduated during this period with a degree in science, mathematics, engineering, or technology fields:.....	0.00
The number of undergraduates funded by your agreement who graduated during this period and will continue to pursue a graduate or Ph.D. degree in science, mathematics, engineering, or technology fields:.....	0.00
Number of graduating undergraduates who achieved a 3.5 GPA to 4.0 (4.0 max scale):.....	0.00
Number of graduating undergraduates funded by a DoD funded Center of Excellence grant for Education, Research and Engineering:.....	0.00
The number of undergraduates funded by your agreement who graduated during this period and intend to work for the Department of Defense	0.00
The number of undergraduates funded by your agreement who graduated during this period and will receive scholarships or fellowships for further studies in science, mathematics, engineering or technology fields:	0.00

Names of Personnel receiving masters degrees

NAME	
Sean Raph	
Total Number:	**1**

Names of personnel receiving PHDs

NAME	
Julieta Martino	
Total Number:	**1**

Names of other research staff

NAME	PERCENT_SUPPORTED
Greer Chapman	1.00
Jamie Gallagher	1.00
FTE Equivalent:	**2.00**
Total Number:	**2**

Sub Contractors (DD882)

Inventions (DD882)

Scientific Progress

Technology Transfer

Final Report
Proposal #: 56448-LS
Agreement #: W911NF-09-1-0296
Title: The Effects of Toxic Particles in Human Lung Cells
Principal Investigator: John Pierce Wise, Sr., Ph.D.
University of Southern Maine
Report Period: August 1, 2010 – July 31, 2015

1. Submissions or Publications under ARO sponsorship **for final reporting period: August 1, 2014- July 31, 2015**.

a. Papers published in peer-reviewed journals – 2
1. Browning, C., The, T., Mason, M.D. and Wise, Sr., J.P. Titanium Dioxide Nanoparticles Are Not Cytotoxic or Clastogenic in Human Skin Cells. Journal of Environmental and Analytical Toxicology, 4-6: 1-6, 2014. http://dx.doi.org/10.4172/2161-0525.1000239.
2. Kandpal SK, Otterson SL, Bousfield DW, Neivandt DJ, Mason MD. Investigation of Laser Induced Structure formation and resultant fluorescence. Optical Materials, 42:256-61, 2015.

b. Papers published in non-peer-reviewed journals - 0

c. Presentations - 21
i. Presentations at meetings, and published in Conference Proceedings (abstracts)
1. Speer, R.M., The, T., and Wise, Sr., J.P. The Cytotoxicity and Genotoxicity of Particulate and Soluble Cobalt in Human Urothelial Cells. Toxicological Sciences, 144: 75, 2015.
ii. Non-Peer-Reviewed Conference Proceeding publications (other than abstracts) – 0
iii. Peer-Reviewed Conference Proceeding publications (other than abstracts) – 0

d. Manuscripts – 2
1. Kandpal, S.K., Co, A., Alcroft, K., Neivandt, D.J., Bousfield, D.W., Mason, M.D. Nanoparticle Derived Laser Induced Fluorescent Micro-Structures. Thin Solid Films. Submitted.
2. Xie, H., Smith, L.J., Holmes, A.L., Zheng, T., Wise, Sr., J.P. The Cytotoxicity and Genotoxicity of Soluble and Particulate Cobalt in Human Lung Epithelial Cells. Sudmitted.

e. Books – 1
i. Book Chapters
1. Co., Aileen, Sitarski, A.M., Grant, J.L., Mason, M.D. "Radiologically Imageable Nanoparticles." Imaging and Visualization in The Modern Operating Room. Springer New York, 2015. 79-88.

f. Honor and Awards – 0

g. Title of Patents Disclosed during the reporting period – 0

h. Patents Awarded during the reporting period – 0

2. Student Supported Personnel Metrics **for final reporting period: August 1, 2014- July 31, 2015** (name, % supported, % Full Time Equivalent (FTE) support provided by this agreement, and total for each category)

a. Graduate Students
i. Julieta Martino – 40%
ii. Total FTE for 1 graduate student supported – 40%

b. Post Doctorates
i. None supported

c. Faculty
i. Hong Xie – 20%
ii. Total FTE for 1 faculty supported – 20%

d. Undergraduate Students
i. None supported

e. Graduating Undergraduate Metrics - 0

f. Master Degrees Awarded – 1
1. “Investigating the Effects of Cobalt on DNA Double Strand Break Repair-Deficient Cells”, Sean Raph, Master’s Thesis, University of Southern Maine, 2015

g. Ph.D.s Awarded – 0
h. Other Research staff
    i. Greer Chapman – 100% for 2 months
    ii. Jamie Gallagher – 100% for 4 months
    iii. Total FTE for 2 staff members supported – 60%

3. “Technology Transfer” – Not applicable

4. Scientific Progress and Accomplishments

Table of Contents

1. Overview

Six interrelated aims were investigated in this project: 1) Characterize metal nanoparticles; 2) Determine metal particle cytotoxicity in human lung cells; 3) Demonstrate metal particle genotoxicity in human lung cells; 4) Characterize metal particle-induced chromosome instability in human lung cells; 5) Compare silver and gold nanoparticle-induced effects in human lung cells; and 6) Assess metal levels in whale skin biopsies in the Gulf of Mexico. The first four aims focused on three categories of metal particles; nanoparticles, particles associated with metal-on-metal hip implants and microparticles of military concern.

Nanotechnology is considered to be the next industrial revolution and to become a 1 trillion dollar industry within the next 10 years. The federal government is already investing billions in nanotechnology development. Nanoparticles are currently in over 300 commercial products including sunscreen, stain-resistant clothing, tires, refrigerators, washing machines and sports equipment. The military is using nanomaterials to develop advances in electronics, munitions, propellants, fuels, nanocomposites, nano-controlled dielectrics and nanoscale photonics. We are at the beginning of the nanotechnology era. However, the same properties that make these particles exciting for technology also make them daunting public health concerns as their toxicity is unknown or poorly understood. Thus, one focus of this study is to determine the effects of gold and silver nanoparticles on human lung cells and titanium dioxide nanoparticles on human skin cells.

Our second category of interest is particles associated with metal-on-metal hip implants. Orthopedic implants restore mobility to hundreds of thousands of patients, including military personnel, each year and these procedures are increasing in younger patients. Studies indicate that total joint replacement therapy is an effective treatment for soldiers allowing them to remain on active duty. However, it is important to fully understand and characterize the adverse health effects from orthopedic implants. Recent studies indicate that patients with metal-on-metal implants have increased rates of bladder cancer only 5-9 years post-procedure and kidney cancer 10 years post-procedure. The underlying cause of the increased cancer risk is unknown, but is most likely due to chemical carcinogens released by the wear and tear of these implants over time. Many implants are made from a cobalt-chromium-molybdenum alloy that wears over time and releases Co, Cr and CoCrMo nanoparticles. Thus, our goal is to investigate the effects of CoCrMo nanoparticles on human urothelial cells.

The last category of interest is microparticles of military concern, including nickel, cobalt and depleted uranium (DU). All of these metal particles are of particular interest to the military as they are used in a number of military applications ranging from munitions to superalloys used in fighter jets. Due to DU's high density and unique combustive properties, the US military has been using DU in military applications since the early 1990s as kinetic penetrators, missile counterweights and tank armor. Upon ignition, DU oxidizes into fine particles raising concerns of exposure to soldiers and civilians in close proximity to exploding DU munitions or DU-armored tanks. The public health concern regarding DU exposure has prompted the use of other metal alloys comprised of nickel, cobalt and tungsten. Cobalt and nickel exhibit strong corrosion and erosion resistance properties making them ideal compounds for military shielding and the aerospace industry. The full toxicological effects of these metal microparticles remains unknown, thus, our goal is to investigate the effects of these particles on human lung cells.

2. Specific Aim #1: Preparation and Characterization of Metal Nanoparticles

2.1. Synthesis and Characterization of Nanoparticles

We generated and tested a silver colloid solution with a mean diameter of ~75 nm, as well as a more commercially relevant size distribution (broader). Size was determined by DLS and TEM (Figure 1). Nanoparticle surface charge was determined and a typical zetapotential distribution and zetapotential versus pH curve are shown in Figure 2. TEM image data as well as the DLS size data show that the larger silver colloid solutions exhibit non-spherical geometry as well as multimodal diameter distributions. Two apparent sizes emerge, around 10 nm and 60 nm. The zeta potential of the particles in the larger distribution (~ -30mV at pH 6.5) is of slightly larger magnitude than those found for the 30 nm particles (~ -20mV at pH 6.5), both of which are consistent with previously reported results.

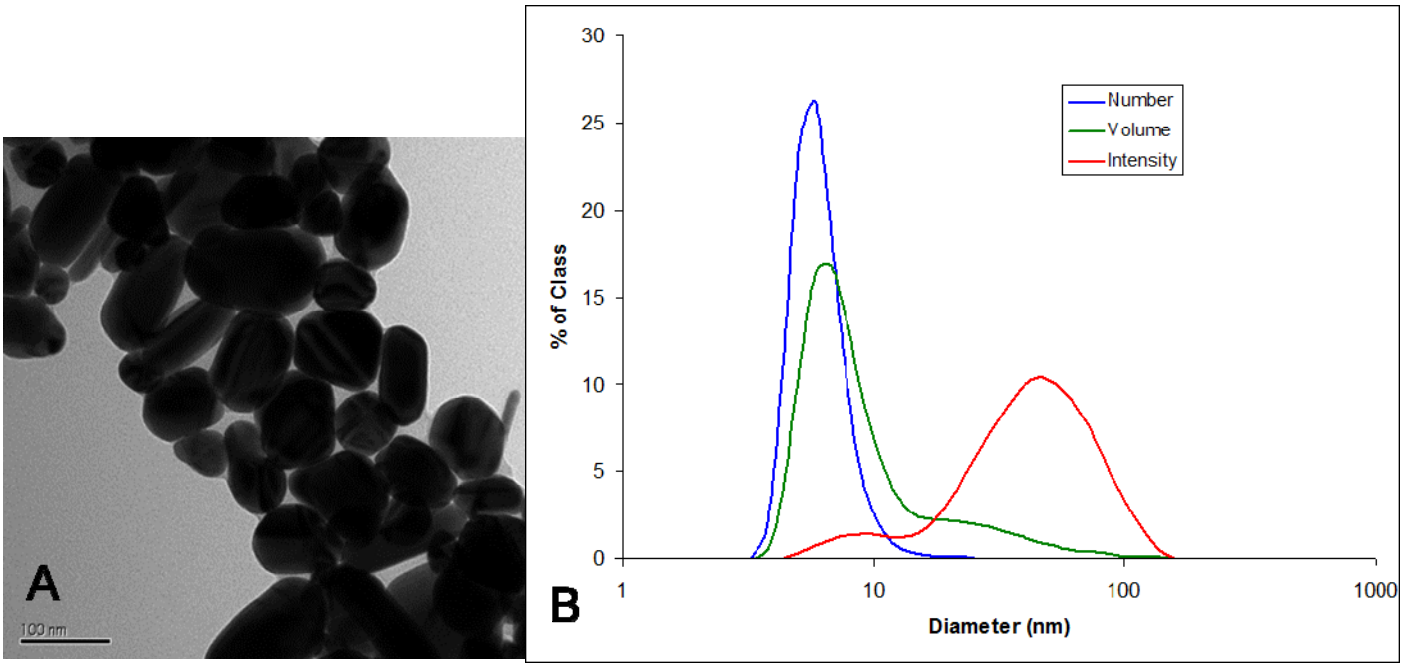

Figure 1. Bare Silver Nanoparticle Size and Shape Characteristics. Larger bare silver nanoparticle size and shape characterizations were determined by transmission electron microscopy and dynamic light scattering (DLS). This figure illustrates the typical sizes and shapes of the as-prepared larger silver nanoparticles. A) Tunneling electron micrograph of filtered as-prepared silver colloids dispersed from water. The particles have an apparent mean diameter of ~ 60 nm. B) Comparison of the size distributions of dilute silver colloids in water calculated based on number (blue), volume (green), and intensity (red).

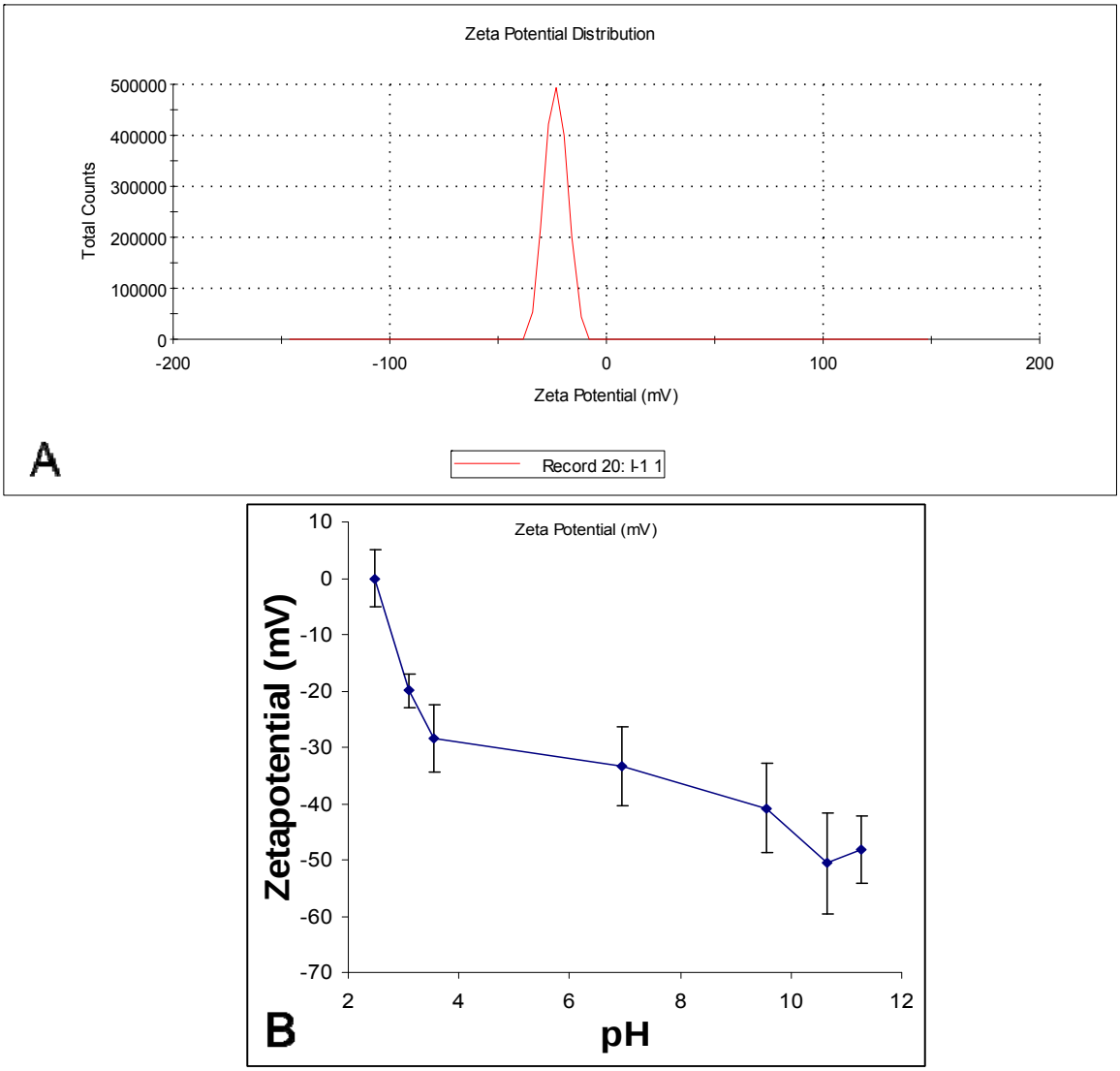

Figure 2. Surface Charge of Bare Silver Nanoparticles. The surface charge (as zetapotential) for larger bare silver nanoparticles was determined using a Malvern zetasizer (electrophoresis). This figure illustrates the typical charge distribution of the as-prepared larger silver nanoparticles. A) Zeta distribution of filtered as-prepared silver colloids dispersed from water. The particles have an apparent mean surface charge of ~-30mV. B) Comparison of the zetapotential versus pH of dilute silver colloids in water.

One of the challenges during this study of toxicological effects of nanoparticles was the production of stable and relevant nanoparticle solutions. Specifically, we encountered extreme difficultly to producing stable colloids at sufficiently high concentration to achieve higher doses for the cell culture studies. This challenge arises from the increased likelihood of nanoparticle aggregation as the nanoparticle density (concentration) is increased. In many cases, aggregation is irreversible and can lead to coalescence, eliminating any correlation between the desired discrete nanoparticle geometry (or size) and any potential toxicological effects. This is exacerbated if one attempts to “grow” nanoparticles using elevated reactant concentrations. To overcome this issue we explored a number of concentration methods which were applied after the colloid completed its growth and reached a semi-stable endpoint. These methods included: slow evaporation, rapid evaporation (under vacuum and heat), centrifugation and resuspension, with and without stabilizers. Final concentrations (metals basis) were determined only for those samples which remained stable overnight, using an inductively coupled plasma mass spectrometry (ICP-MS). Results of this study indicated that colloids with silver content above ~60 ug/ml were not generally stable without the use of stabilizing agents. However, we found that serum could be used effectively as a stabilizing agent during centrifugation. We were able to reach concentrations above 150 ug/ml using this method. The use of serum also eliminates the need for dilution prior to introduction into the cell

culture media, increasing the effective dose to be administered. Sample DLS size distributions before and after concentration in serum are shown in Figure 3.

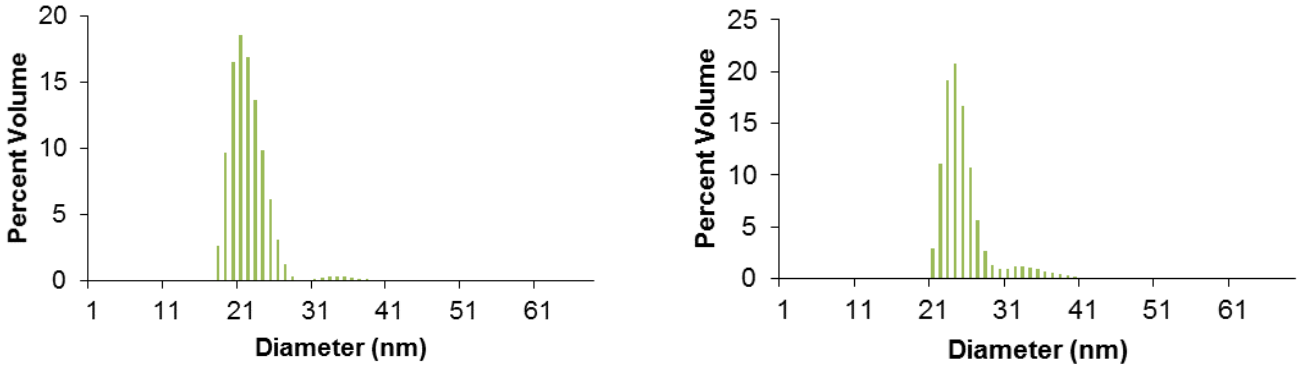

Figure 3. Concentration of Silver Nanoparticles as Measured by DLS. DLS size distributions before (left) and after (right) concentration in serum.

An additional method for producing highly concentrated nanoparticles was developed using biocompatible polyvinyl alcohol (PVOH) as a stabilizing agent. A simple nanoparticle concentration process was developed, using the addition of 1-3 wt% (by total metals mass) of PVOH (MW 5000) just after nanoparticle growth provides a dramatic increase in nanoparticle stability allowing for concentration via centrifugation and resuspension. After slow agitation, the excess PVOH was removed by centrifugation and washed to achieve the desired final concentration. The PVOH physisorbs strongly to the nanoparticles surface. Using this method nanoparticle (metals basis) concentrations in excess of 1000 ug/ml are now possible. The use of PVOH requires that careful PVOH toxicology control experiments be performed, although as only the surface concentration of PVOH (not the solution concentration) is relevant, only extremely small PVOH concentrations remain.

Gold nanoparticle were also produced and characterized. Three sizes were to be studied: ~5 nm, ~20 nm, ~60 nm. Representative TEM images of all three sizes (neat in water) are shown in Figure 4. Here, as with the silver particles, larger particles exhibit non-spherical geometry (crystalline). Sizing of the gold particles is performed in exactly the same manner as that used for the silver nanoparticles. A representative DLS distribution (number, volume, and intensity weighted) is shown in Figure 5.

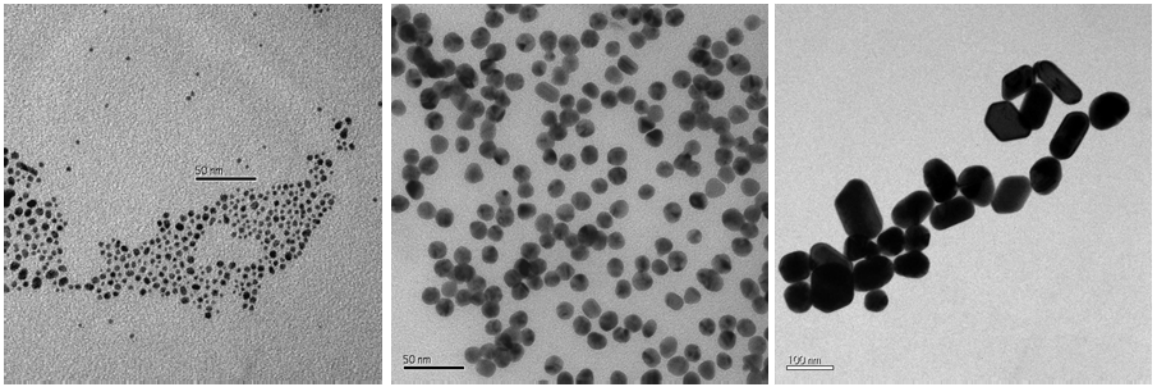

Figure 4. TEM Images of Gold Nanoparticles in the Three Different Sizes.

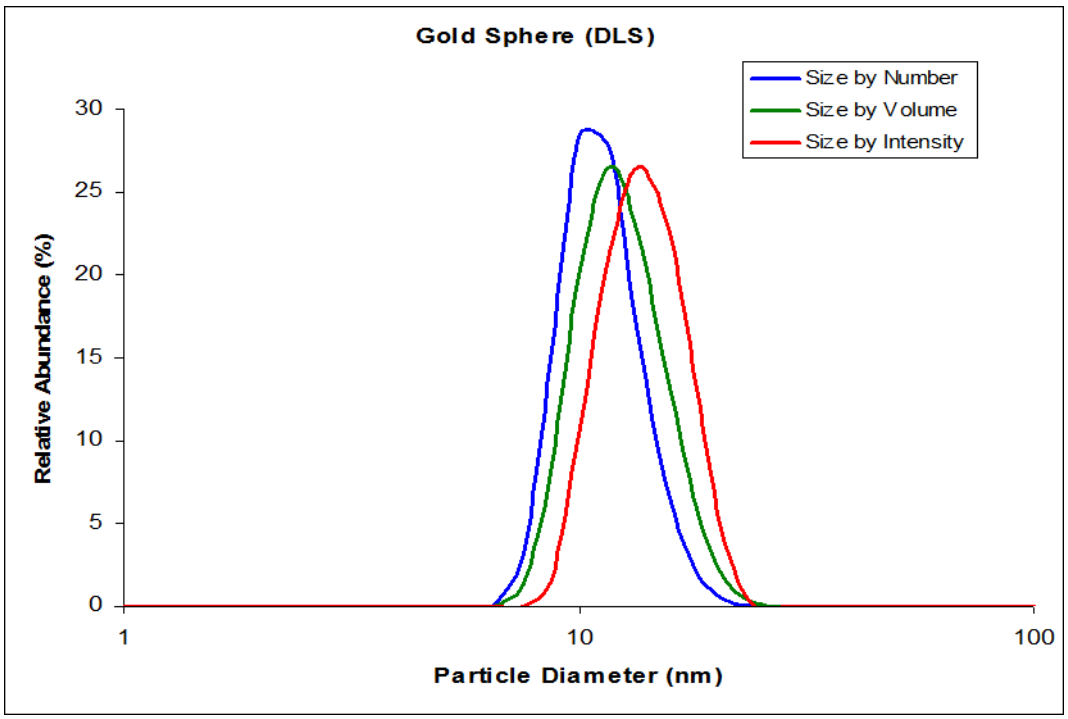

Figure 5. DLS Size Distributions for a Representative Sample of 20 nm Gold Particles. This figure shows the three different weightings confirm the homogeneity (low polydispersity) of the gold nanoparticle solutions.

We expanded this study to include a number of other metal nanoparticle systems. For example, one nanoparticle geometry of specific interest are gold nanostars. These engineered nanoparticles are gaining in popularity as specialized nanoscale reporters for a number of bioengineering applications. For our purposes, they represent a gold nanosphere with a modified surface which we expect to be highly energetic due to local field enhancement near the tips of the surface features. TEM images of a size series of gold nanostars are shown in Figure 6. It is clear from the TEM image data that increased exposure to nanoparticle grown media allows for controlled formation of surface features. Using smaller initial cores allows for some control of the final nanostar diameter, though a lower limit of around 50 nm has been demonstrated in our lab. Surprisingly, stable nanostars with diameters above 150 nm have been achieved. This may be due to the large effective surface charge density that originates at the tips of the surface features. This is expected to impart unusually high electrostatic stabilization. A photograph of the as prepared solutions is shown in Figure 7 and representative DLS size distributions of three nanostar samples are shown in Figure 8.

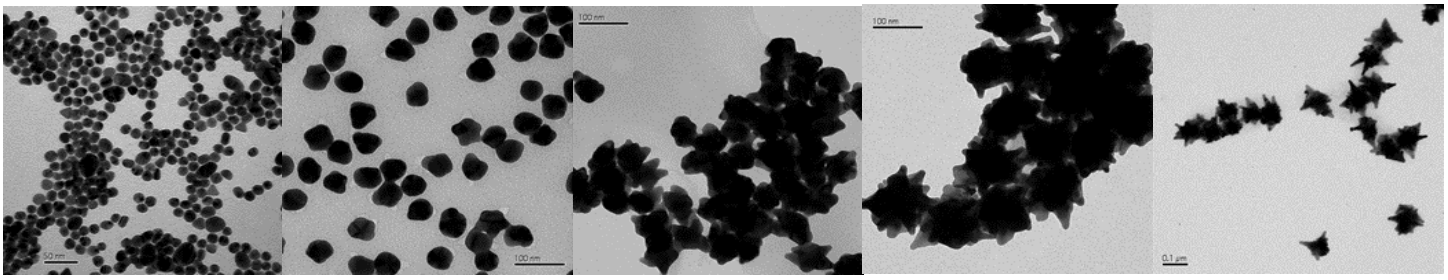

Figure 6. TEM images of gold nanostars. Increasing surface features (left to right), beginning with unmodified gold cores. Scale bar is 100 nm.

Figure 7. Photograph of a series of nanostars increasing in diameter from left to right.

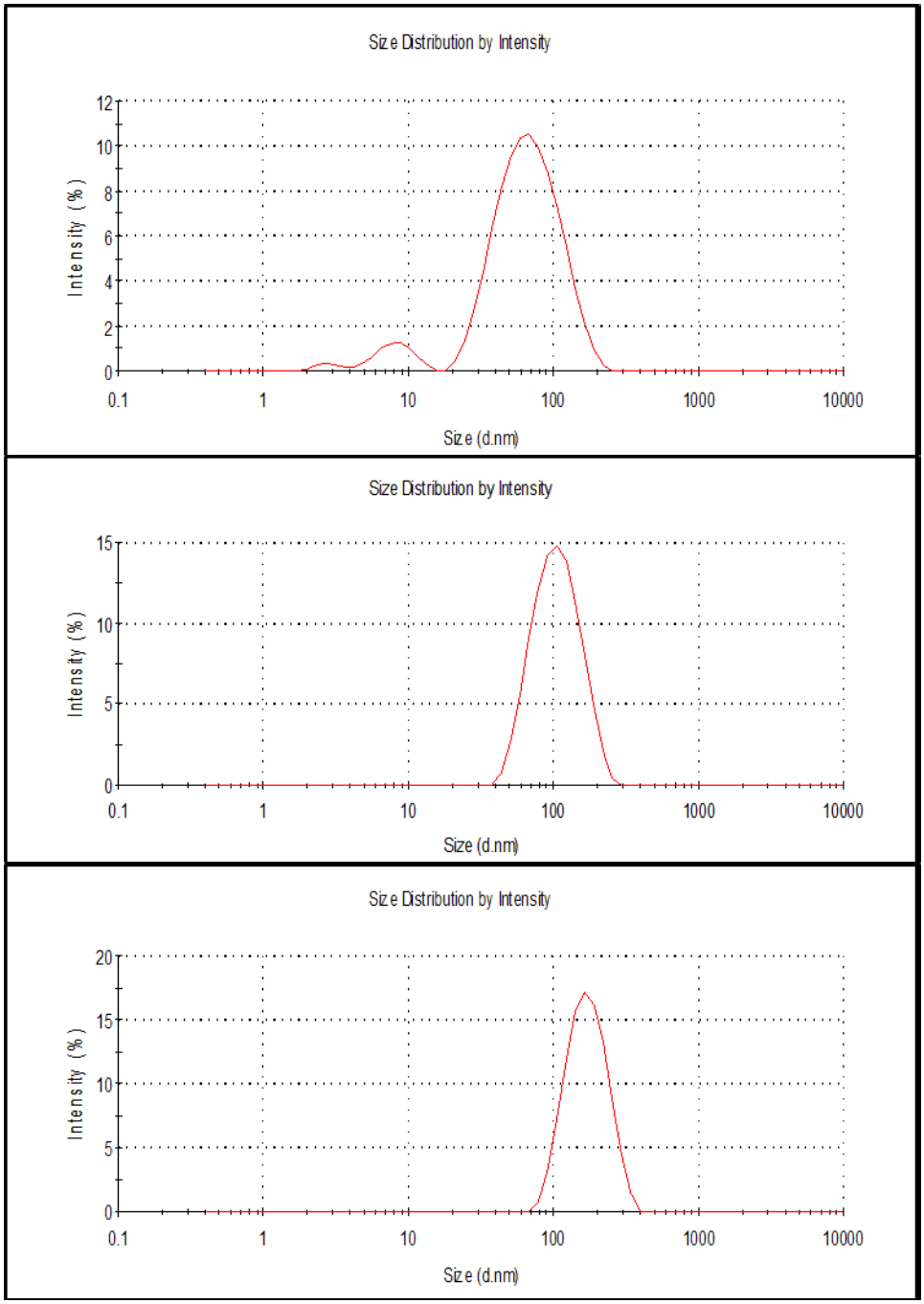

Figure 8. DLS Data for Three Different Nanostar Systems. This figure shows the size distribution for three different gold nanostar systems. A) 75 nm diameter. B) 100 nm diameter. C) 175 nm diameters.

In addition, to the bare particles (characterization data presented here), we also produced 30 nm and the larger distributed size system with surface modifications which include: amine terminated polyethylene glycol (NH2-PEG-SH), neat polytheylene glycol, both thiolated for strong chemisorption and unthiolated for physisorption, and fluorescein isothiocyanate aminopropyltoluene (APT), polyethylene glycol (PEG), mercaptopyridine (MP), and silica (from aminopropyltrimethoxysilane). While the most samples show no visible change in shape or particle size by TEM or DLS, the surface modification has been verified by Raman microspectroscopy (data not shown). The silica modification is somewhat more complicated. A TEM image of a typical silica coated silver nanoparticle is shown in Figure 9. For comparison, a silica coated gold particle is also shown (described below).

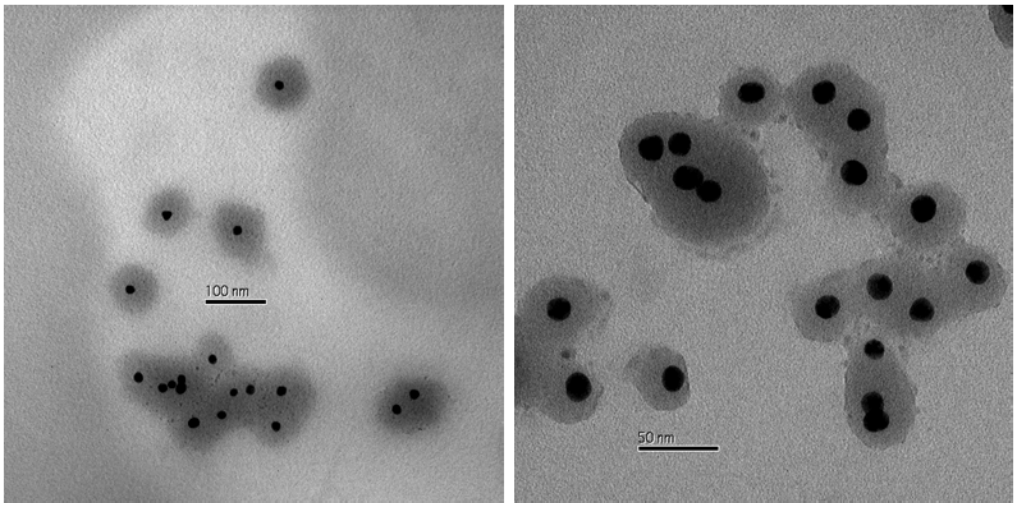

Figure 9. TEM Images of Silver (left) and Gold (right) Nanoparticles Coated with a Layer of Silica.

Finally, we also produced and characterized titanium dioxide nanoparticles which are of significant interest both commercially and scientifically. the base nanoparticles were purchased from Dupont (TiPure – 50nm). These nanoparticles are widely used by industry. The as purchased particles (in water) appear highly agglomerated as indicated by TEM and dynamic light scattering (Figure 10).

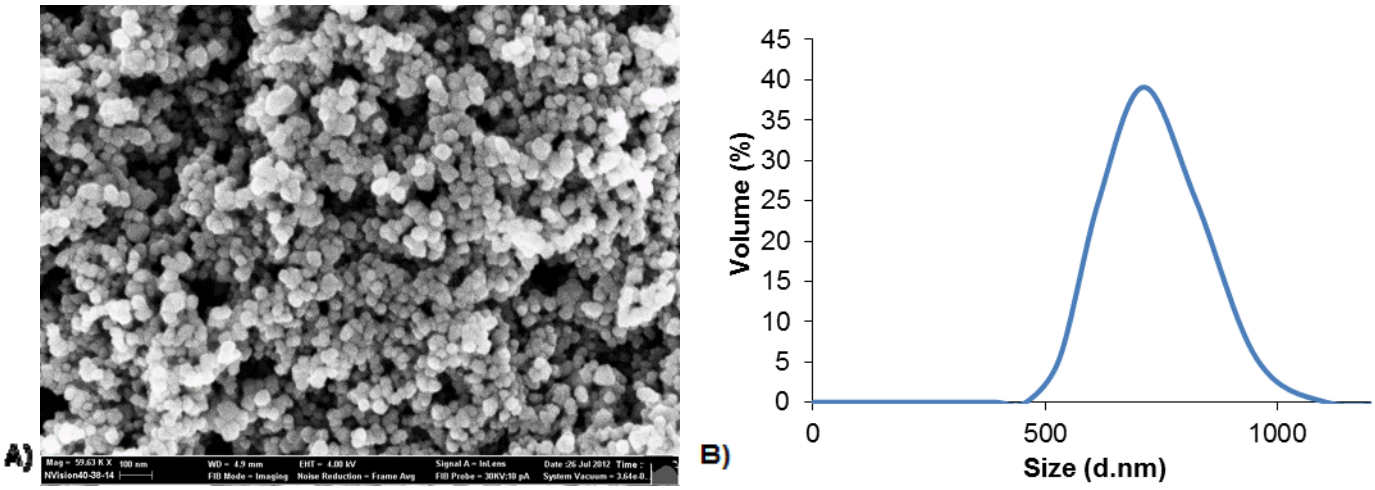

Figure 10. Titanium Dioxide Nanoparticles. TEM (A) and Dynamic Light Scattering size distribution (B) of as purchased titania nanoparticles suspended in water and vortexed for 30 seconds.

2.2. Production of Particles Associated with Metal-on-Metal Hip Implants

Due to the growing interest in more complex nanoparticles systems, we expanded our study to include a number of other metal particle systems. Of particular interest has been cobalt-chromium-molybdenum (CoCrMo) nanoparticles associated with biological implants. For the CoCrMo implants, the wear products of these materials are expected to be nanoparticulate in nature within a relevant size range of 50 nm – 10 um.

Unfortunately, the primary material system of interest, CoCrMo (ASTM 75) proved to be far too large for use as purchased (Figure 11 – red curve). As such a number of size reduction strategies, based on the as-purchased material, were considered. Due to the broad size distribution, including a significant material fraction in the desired 2-10 micron diameter range, a simple size exclusion method was first tested. Here a 45 um dry shaker sieve was employed. The resulting fractions (less than or greater than 45 um) were then separately sized. The dry sizing data, shown in Figure 11 (blue – less than, green – greater than), did indicate some size separation, but not sufficient for our use. While not practical some additional size exclusion was achieved by passing the prescreened (<45 um) particles through successive filtration steps using vacuum and Anatop filters. After several such repeats, the smallest average size obtained was still around 3 microns (Figure 11 – red curve), larger than desired. Unfortunately, this approach resulted in extremely low yields, insufficient for our use.

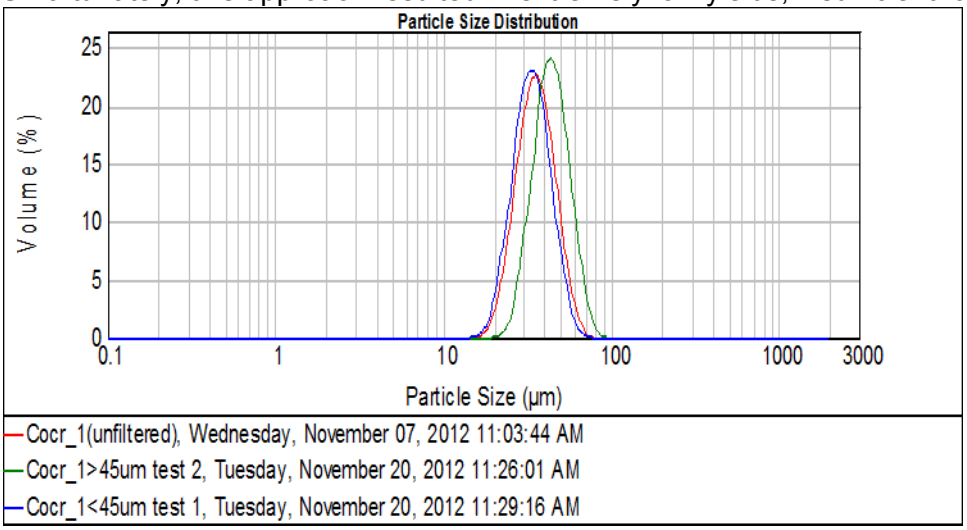

Figure 11. Size Distribution of CoCrMo Particles. CoCrMo dry nanoparticle size distributions obtained using the dry particle sizer, before and after size exclusion using a mechanical sieve.

A second size reduction method was explored which involved dry milling the as-purchased CoCrMo powder with porous alumina milling media (diameter < 2mm) (Figure 12). Generally, Co powders are considered too hard for milling by this method. In fact, we found that after milling for 24 h the milling media appeared to be covered in an extremely fine CoCrMo powder. The remaining CoCrMo was separated from the 'fouled' media by mechanical sieving. Approximately 99% of the initial as-purchased CoCrMo powder was retained in the process. The remaining CoCrMo was separated from the milling media by slow shaking and emersion in boiling water for 24 h. The resulting liquid was decanted, dried and analyzed. Elemental analysis indicated virtually no sample fouling, while dry particle sizing showed a dramatic size reduction (~600 nm diameter). It is our belief that the media does not reduce the particle size, but rather effectively filters out the smaller particles by trapping them in or around surface pores. Interestingly, samples prepared by this method are not long-term stable against sedimentation, but can be fully resuspended via ultrasonication even at concentrations above 1000 ug/mL. While this method produced some useful material, the yield was far too low, and the minimum particle size did not include particles in the 50-500 nm range, as desired.

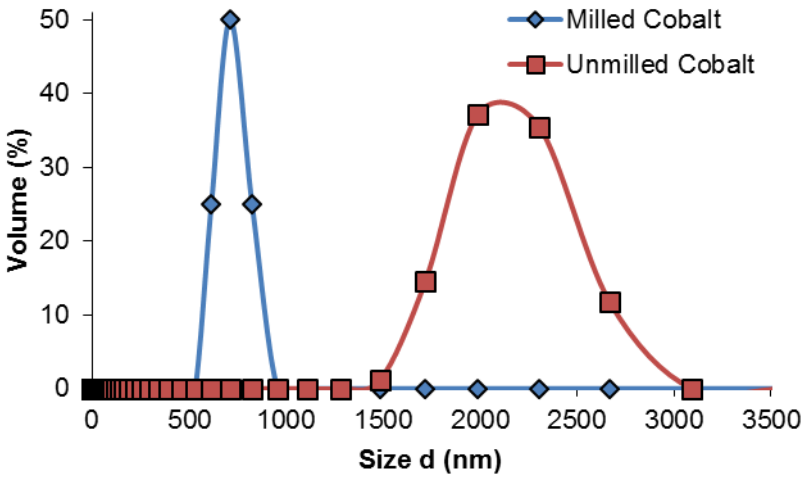

Figure 12. Effect of Milling on CoCrMo Particle Size. Effect of ball milling on mean colloid size. Representative size distributions of the dispersed CoCrMo colloid before (red) and after (blue) 24 milling.

To achieve the desired size fraction, including particles between 50-500 nm, a new approach based on diminution grinding was implemented, using an ASTM 75 hip implant. This approach, illustrated in Figure 13, is effectively a clean metal-on-metal rapid friction method. Here a high frequency wear and a random motion was achieved using the motor from a palm sander. With this approach no contact with foreign materials or milling media is required, reducing the possibility of impurities. The simple device allows for room temperature or low temperature grinding (LN2 bath), and removes particles via vacuum into an air trap and secondary water trap. While not rapid, as much as 100 mg of clean material can be produced in a 24 h period.

Figure 13. Image of new metal on metal grinding apparatus.

2.3. Characterization of Metal Microparticles of Military Concern

We characterized nickel sulfide, a particulate nickel compound, and cobalt oxide, a particulate cobalt compound. While particles greater than ~ 1 um are biologically relevant, they are generally considered to be unstable in solution. This can be observed by the naked eye as nanoparticle suspensions prepared from our as purchased materials almost immediately settled out. Sonication and/or vortexing was sufficient to create a relatively homogeneous suspension, indicating that nanoparticle aggregation was not a dominant factor. Unfortunately, rapid sedimentation eliminates the possibility of using standard solution phase Dynamic light scattering for sample sizing. As such, a new dry particle sizer (Malvern-Morphologi) was used. Sample nickel

sulfide data are shown in Figure 14. Conventional optical imaging is employed on an electrostatically dispersed dry sample (series of images on right). Particle volumes were determined particle by particle using software edge-analysis, and size distributions were accumulated manually as number distributions. The as purchased nickel sulfide, shown in Figure 14, demonstrated a mean particle diameter of around 2 um, which was within the desired size range. As such, no further size reduction was required for this material system. Similar results were obtained for the cobalt oxide nanoparticle system which was prepared as a pure cobalt control (Figure 14 – bottom). For this system the average particle diameter was around 1 um.

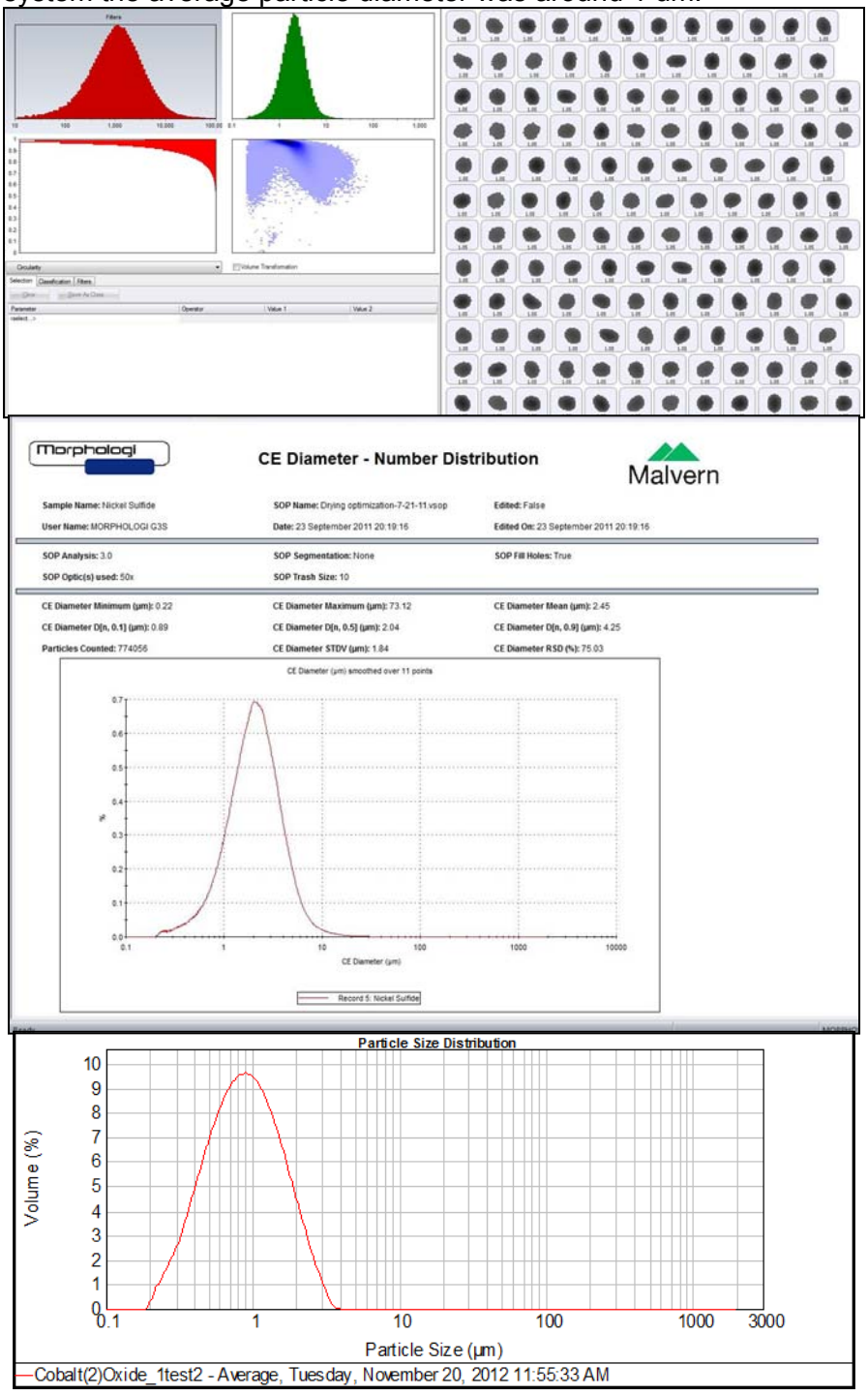

Figure 14. Nickel Sulfide and Cobalt Oxide Size Distributions. Raw dry sizing data for as purchased NiS nanoparticles **(Top)**, and the resultant cumulative size distribution (**Middle**). Cumulative size distribution of CoO as-purchased particles (**Bottom**).

3. Specific Aim #2: Determine Metal Nanoparticle and Microparticle-Induced Cytotoxicity in Human Lung Cells

3.1. Cytotoxicity of Nanoparticles

Our early investigations revealed that concentrations up to 3 or 4 ug/cm^2 bare or functionalized silver nanoparticles induced minimal to no cytotoxicity in human lung cells (Figure 15). In order to determine if higher doses of nanoparticles induced toxicity in human lung cells many technical problems were encountered. Using polyvinyl alcohol (PVA) to stabilize the nanoparticle solution (shown in earlier reports to be non-toxic); we were able to achieve higher concentrations of silver nanoparticles. We compared the cytotoxic effects of silver nanoparticles with and without functional groups added. We found that treatment with bare silver nanoparticle concentrations induced no cytotoxicity in human lung cells after 24 h and treatment; with both the thiolated pegylated and non-thiolated pegylated silver there was a small increase in cytotoxicity after 24 h treatment (Figure 16A). When cells were treated with a chronic exposure there was a concentration-dependent decrease in relative survival for all types of silver nanaoparticles. When a pegylated functional group was added to the silver nanoparticles, the cytotoxicity of the functionalized silver nanoparticles increased after 120 h as compared to the bare silver nanoparticles (Figure 16B).

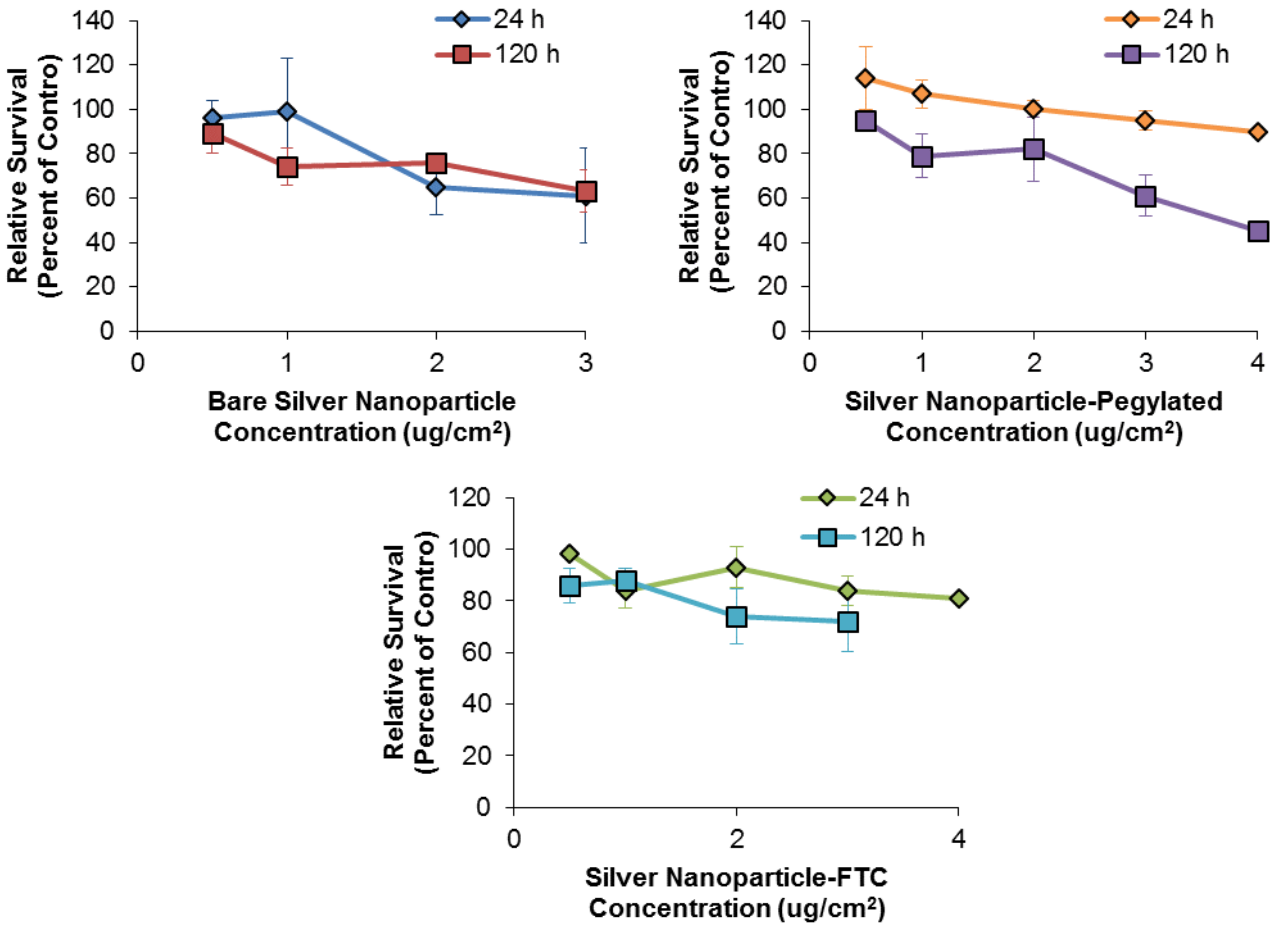

Figure 15. The Cytotoxicity of Bare, Fluoroscein Thiocyanate Functionalized (FTC) and Pegylated Silver Nanoparticles. This figure shows the cytotoxicity of bare, FTC and pegylated silver nanoparticles. A) Bare silver nanoparticles are toxic to human lung fibroblasts after 24 or 120 h exposure. B) Pegylated silver nanoparticles are not toxic to human lung fibroblasts after 24 h but are toxic after 120 h exposure. Error bars represent 3 independent experiments ± the standard error of the mean. C) FTC silver nanoparticles are mildly toxic to human lung fibroblasts after 24 h or 120 h exposure.

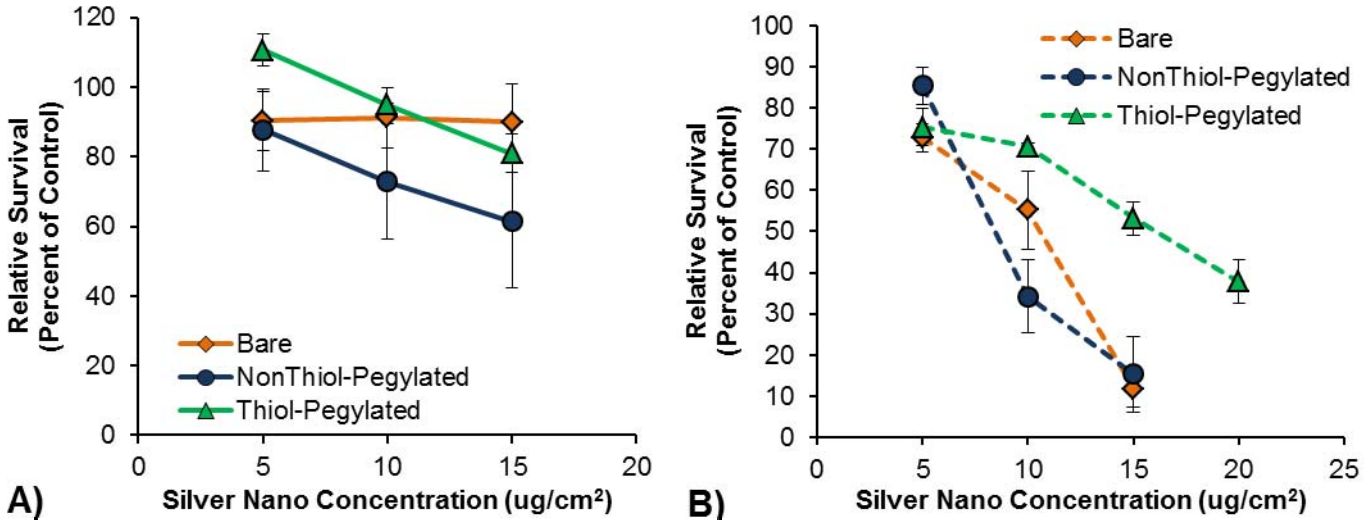

Figure 16. The Cytotoxicity of Silver Nanoparticles in Human Lung Fibroblasts. This figure shows the cytotoxicity of bare and functionalized silver nanoparticles in human lung cells. A) Exposure to silver nanoparticles for 24 h induced minimal cytotoxicity. B) 120 h exposure to silver nanoparticles induces a concentration-dependent increase in cytotoxicity. Data represent 2-3 experiments.

Additionally, we considered the effects of the bare silver nanoparticles in human lung epithelial cells. We found that similar to the human lung fibroblast cells there was minimal cytotoxicity in the epithelial cells after a 24 h treatment. When the treatment times were extended to 120 h the bare silver nanoparticles had a concentration-dependent increase in cytotoxicity (Figure 17).

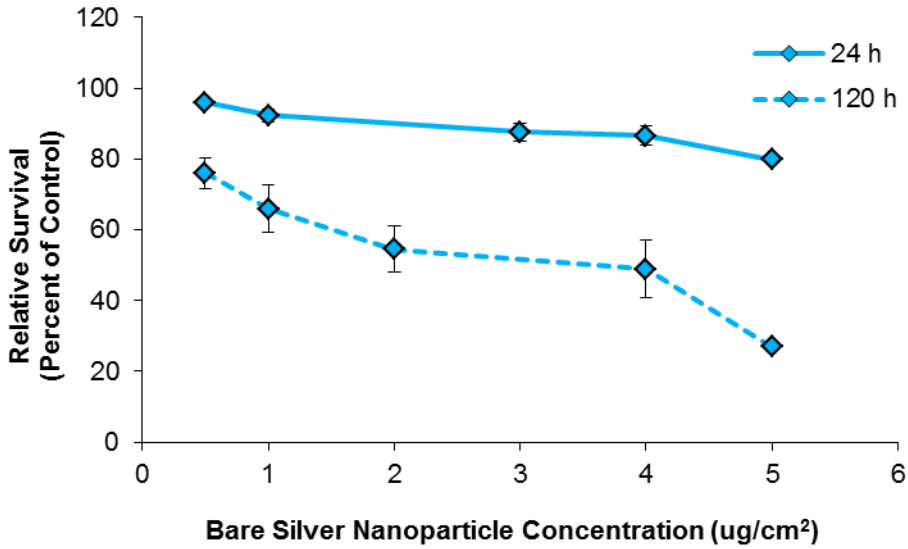

Figure 17. The Cytotoxicity of Silver Nanoparticles in Human Lung Epithelial Cells. This figure shows the cytotoxicity of bare silver nanoparticles in human lung epithelial cells (HBEC2). There was a concentration-dependent increase in cytotoxicity with chronic treatment of bare silver nanoparticles.

We assessed the cytotoxicity of bare gold nanospheres. Concentrations up to 15 ug/cm^2 gold nanoparticles did not induce a cytotoxic effect at 24 or 120 h exposure times (Figure 18). We also considered the cytotocxic effects of gold nanostars, these nanoparticles have a different structure and stability compared to the bare gold nanoparticles and needed to be suspended in polyethylene glycol (PEG) to maintain their stability and prevent agglomeration. We experienced difficulty getting accurate concentrations of the gold nanostars, therefore we treated based on media displacement while we optimize our detection methods. We found that displacing up to 12% of the media with gold nanostars induced no toxicity after a 24 or 120 h exposure (Figure 19A). There was

a small increase in cytotoxicity after 120 h exposure to gold nanostars but this toxicity was due to the PEG vehicle instead of the nanoparticles themselves (Figure 19B).

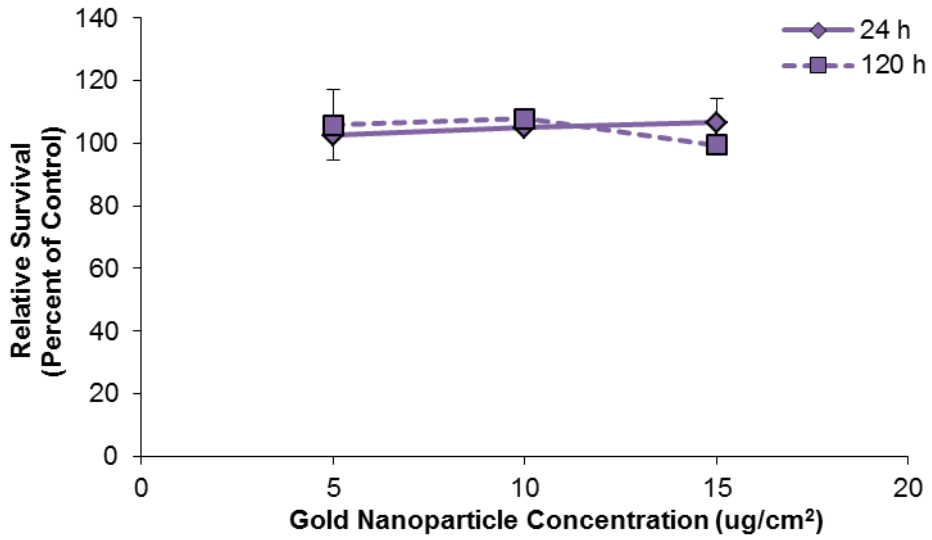

Figure 18. The Cytotoxicity of Bare Gold Nanoparticles. This figure shows that bare gold nanoparticles were not cytotoxic to human lung cells. Data represent the average of 3 experiments ± the standard error of the mean.

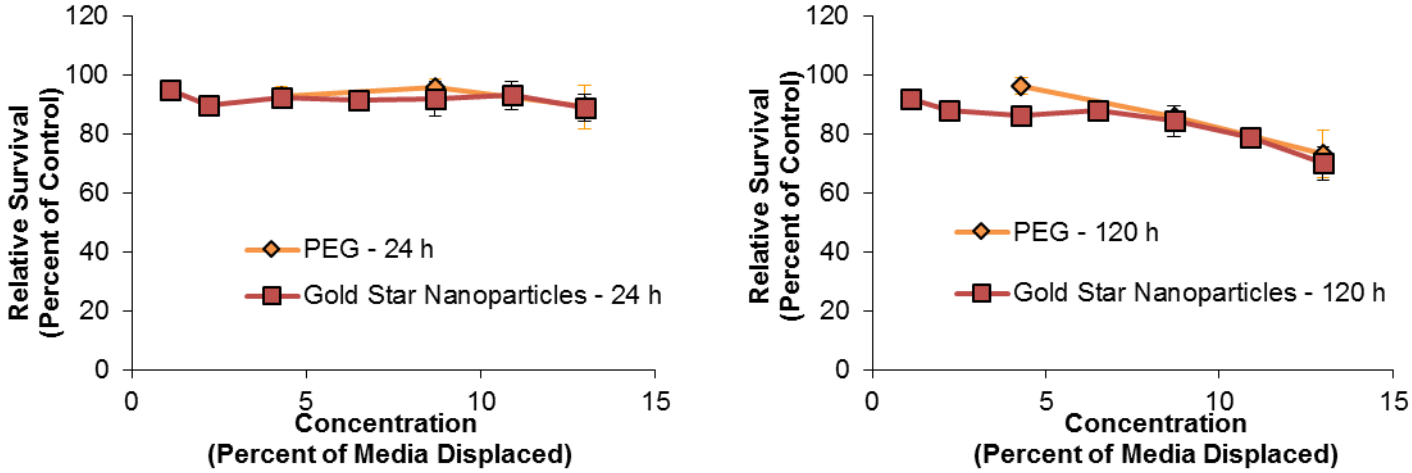

Figure 19. The Cytotoxicity of Gold Nanostars. This figure shows that gold nanostars are not cytotoxic to human lung fibroblast cells after a 24 h (Panel A) or 120 h (Panel B) exposure. Higher concentrations of the PEG vehicle control do induce cytotoxicity after a 120 h exposure. Data represent the average of 2 experiments ± the standard error of the mean.

In addition to assessing the toxicity of silver and gold nanoparticles, we have also investigated the toxicity of titanium dioxide nanoparticles. Titanium dioxide nanoparticles induced no toxicity in human and California sea lion skin cells after 24 or 120 h exposure (Figure 20). Considering the lack of cytotoxicity in response to titanium dioxide nanoparticles, we discontinued the titanium dioxide project, but the human data were incorporated into a paper that has been published: Browning, C., The, T., Mason, M.D. and Wise, Sr., J.P. Titanium Dioxide Nanoparticles Are Not Cytotoxic or Clastogenic in Human Skin Cells. Journal of Environmental and Analytical Toxicology, 4-6: 1-6, 2014.

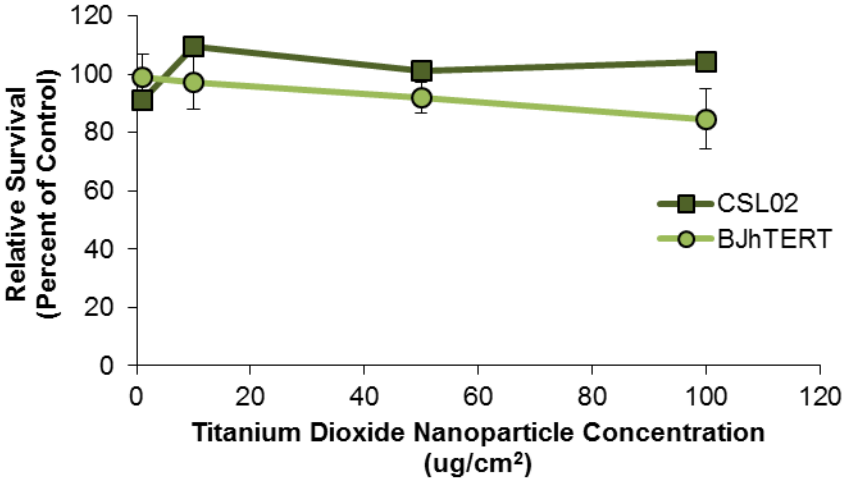

Figure 20. Cytotoxicity of Titanium Dioxide Nanoparticles in Human Skin Cells and California Sea Lion Skin Cells. This figure shows that titanium dioxide nanoparticles did not induce cytotoxicity in California sea lion skin cells (CSL02) or human skin cells (BJhTERT). Data represent one experiment (CSL02) or an average of at least 3 independent experiments +/- the standard error of the mean (BJhTERT).

3.2. Cytotoxicity of Particles Associated with Metal-on-Metal Hip Implants

We assessed the cytotoxic effects of cobalt-chromium-molybdenum (CoCrMo) nanoparticles on human urothelial cells. Recent studies indicate that patients with metal-on-metal implants have increased rates of bladder cancer only 5-9 years post-procedure and kidney cancer 10 years post-procedure. The underlying cause of the increased cancer risk is unknown, but is most likely due to chemical carcinogens released by the wear and tear of these implants over time. Many implants are made from a cobalt-chromium-molybdenum alloy that wears over time and releases Co, Cr and CoCrMo nanoparticles. Thus, our goal was to investigate the effects of CoCrMo nanoparticles on human urothelial cells. CoCrMo nanoparticles induce a concentration- and time-dependent increase in cytotoxicity in human urothelial cells (hTu1-38 cells) and an additional urothelial cell line, Urotsa, clone 57 (Figure 21). CoCrMo nanoparticles induced a similar level of cytotocicty after a 24 h treatment in both cell lines, however the Urotsa cell line was more sensitive to CoCrMo nanoparticles after 120 h of treatment, particularly at the lower treatment concentrations.

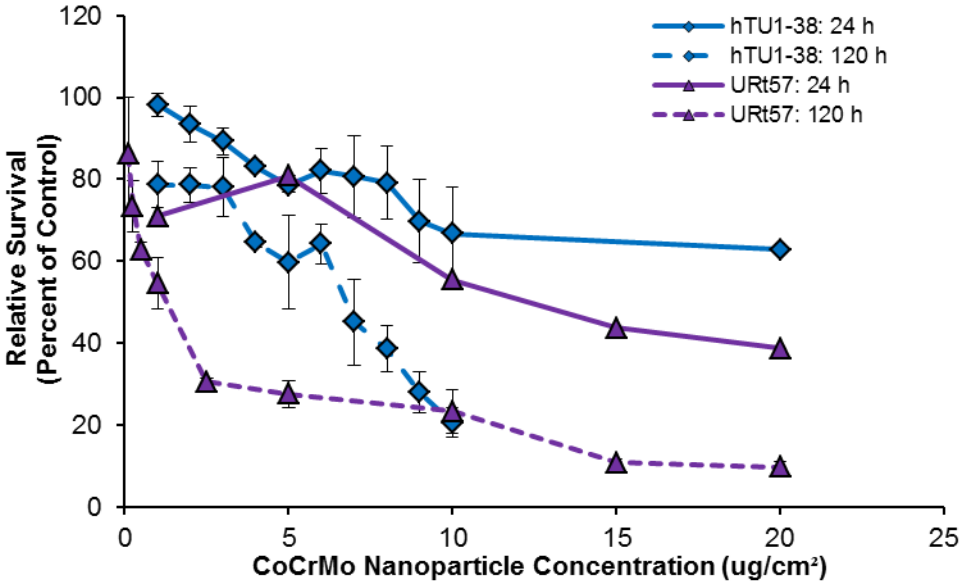

Figure 21. Cytotoxicity of CoCrMo Nanoparticles in Human Urothelial Cells. This figure shows that CoCrMo nanoparticles induced a concentration- and time-dependent increase in cytotoxicity in two types of human urothelial cell lines. Data represent an average of 1-4 experiments +/- the standard error of the mean.

We also generated CoCrMo nanoparticles from an actual hip implant. We found that hip nanoparticles induced a concentration-dependent increase in cytotoxicity in human urothelial cells, hTU1-38 (Figure 22).

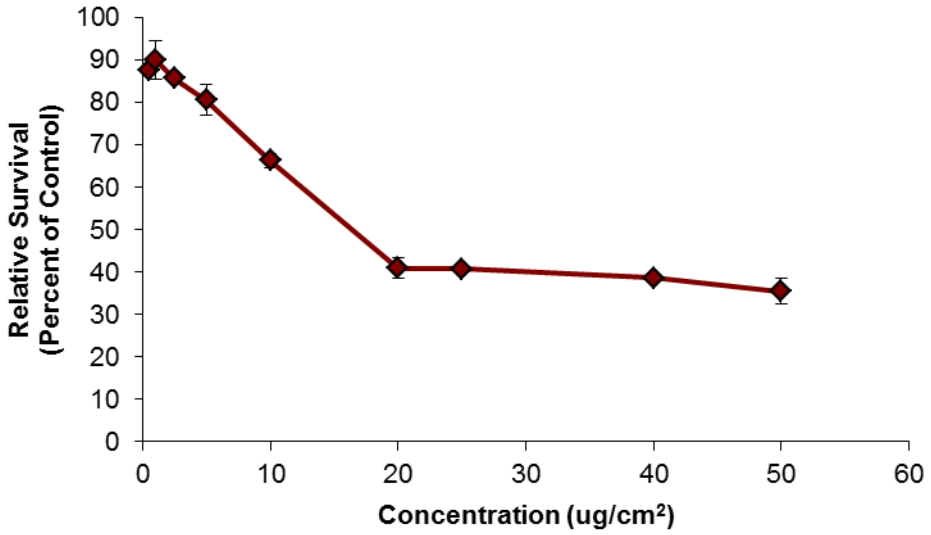

Figure 22. Cytotoxicity of CoCrMo Hip Implant Nanoparticles in Human Urothelial Cells. This figure shows that CoCrMo hip implant nanoparticles induced a concentration-dependent increase in cytotoxicity in human urothelial cells after a 24 h treatment. Data represent an average of 2 experiments +/- the standard error of the mean.

We also considered the effect of individual elements which may be released from hip wear to try to understand the contribution of each type of element to urothelial toxicity. First we needed to trouble shoot the Cr(III) particles by comparing the cytotoxicity of 4 different manufacturers of chromium oxide (Cr_2O_3) particles in our human lung cell model (#1 - Stream Chemicals Cat#100205-440; #2 - Alfa Aesar Cat# AA36258-14; #3 - Sigma-Aldrich Cat#39370-3; #4 – Aldrich Cat#39,370-3); all 4 manufacturer's induced similar cytotoxic effects at 24 and 120 h treatment times (Figure 23 A, B). Next we considered the cytotoxic effect of Cr(III), Cr(VI), cobalt and molybdenum particles in a human urothelial cell line (hTU1-38), their target organ. Chromium oxide, lead chromate and cobalt oxide induced a concentration-dependent increase in cytotoxicity at 24 and 120 h (Figure 24). Molybdenum oxide did not induce cytotoxicity at the concentrations tested (Figure 24 D).

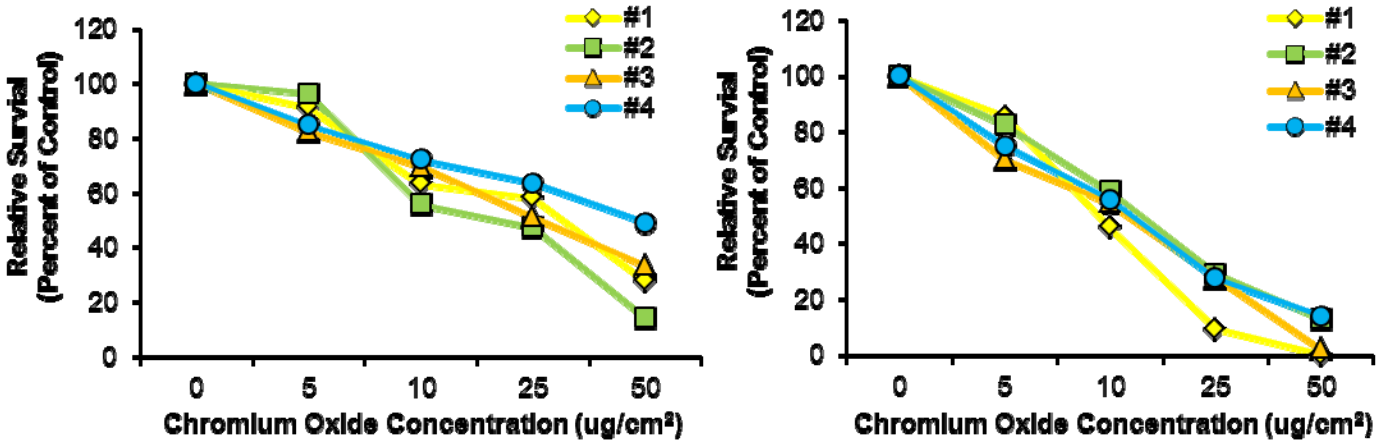

Figure 23. Cytotoxicity of Hip Implant Component Particles (Cr(III)) in Human Lung Cells. This figure shows that Chromium (III) oxide induced a concentration-dependent increase in cytotoxicity in human urothelial cells. A) 24 h B) 120 h. Data represent 1 experiment for each chemical and time point.

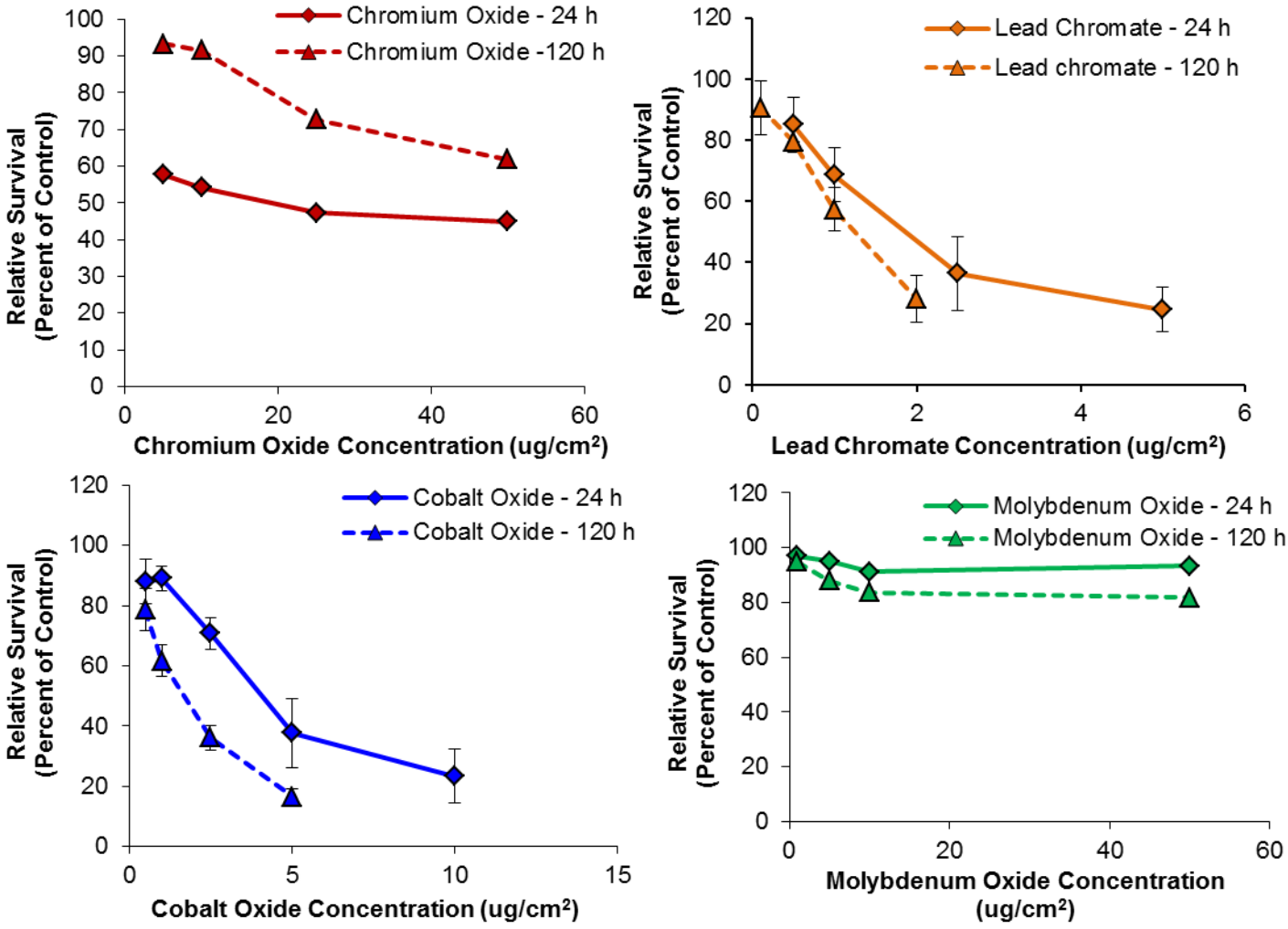

Figure 24. Cytotoxicity of Hip Implant Component Particles in Human Urothelial Cells. This figure shows the cytotoxicity of hip implant component particles in human urothelial cells. A) Chromium oxide (Cr(III)). B) Lead chromate (Cr(VI)). C) Cobalt oxide. D) Molybdenum Oxide. Data represent 1- 3 experiments +/- the standard error of the mean.

3.3. Cytotoxicity of Metal Microparticles of Military Concern

Considering the minimal cytotoxic effects of silver, gold and titanium dioxide nanoparticles, we have expanded our work to include micron-sized particles, specifically nickel, cobalt and depleted uranium (DU) which are of particular concern in military application. Last year we reported our preliminary findings on nickel in human lung fibroblast and epithelial cells and have since completed these studies (Figure 25). Data for the epithelial cells has been published: Holmes, A.L., The, T., Thompson, K., Mason, M., Kandpal, S., Zheng, T., and Wise, Sr., J.P. Chronic Exposure to Particulate Nickel Induces Neoplastic Transformation in Human Lung Epithelial Cells. Toxics, 1(1): 46-59, 2013. doi:10.3390/toxics1010046. In sum, we found that nickel subsulfide induced concentration- and time-dependent increases in cytotoxicity in human lung cells

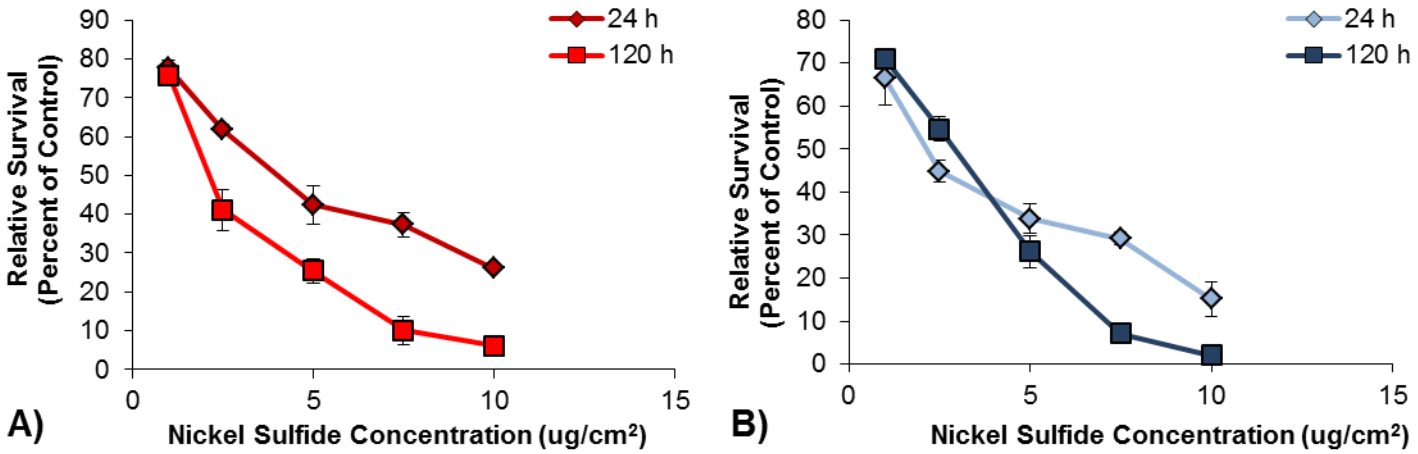

Figure 25. Cytotoxicity of Nickel Subulfide in Human Lung Fibroblast and Epithelial Cells. This figure shows that nickel subsulfide induced a concentration-dependent increase in cytotoxicity in human lung cells after a 24 or 120 h exposure. A) Human lung fibroblasts. B) Human lung epithelial cells. Data represent an average of 3-5 experiments +/- the standard error of the mean.

Cobalt, both particulate and soluble forma, induced a concentration-dependent increase in cytotoxicity in human lung fibroblasts. Cobalt induced similar toxic effects in primary lung epithelial cells. Particulate and soluble cobalt induced a concentration-dependent decrease in relative survival in human lung cells; based on administered concentration, primary epithelial cells appeared to be less sensitive to cobalt oxide and cobalt chloride compared to fibroblast cells (Figure 26).

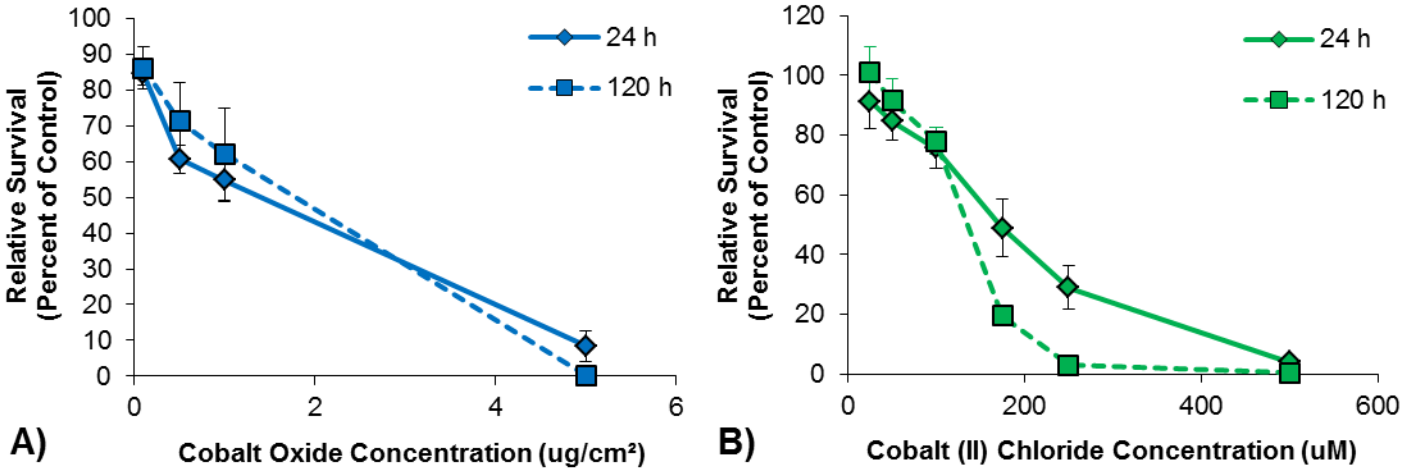

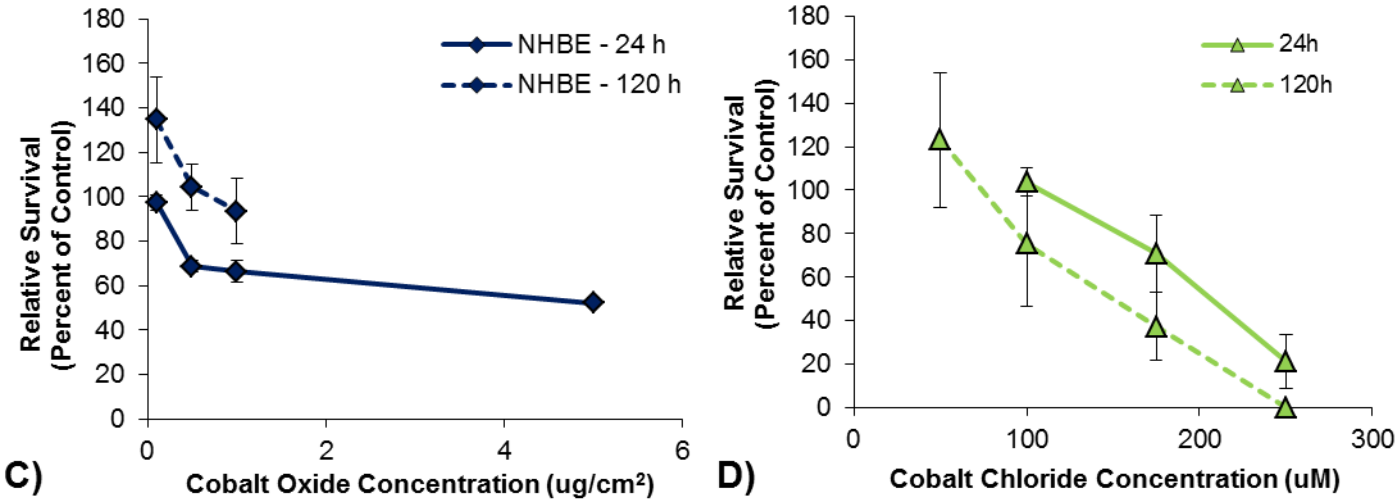

Figure 26. Cytotoxicity of Particulate and Soluble Cobalt in Human Lung Cells. This figure shows that cobalt induced a concentration-dependent increase in cytotoxicity in human lung cells. A) Cobalt oxide-induced cytotoxicity in human lung fibroblast cells after 24 or 120 h exposure. B) Cobalt chloride-induced cytotoxicity in human lung fibroblast cells after 24 or 120 h exposure. C) Cobalt oxide-induced cytotoxicity in human lung epithelial cells (NHBE) after 24 or 120 h exposure. D) Cobalt chloride-induced cytotoxicity in human lung epithelial cells (NHBE) after 24or 120 h exposure. Data represent an average of 2-3 independent experiments +/- the standard error of the mean.

We hypothesized that the difference in response between epithelial and fibroblast cells may be due to differences in uptake. In order to test this, we determined the intracellular Co concentration after exposure to soluble or particulate cobalt in both cell types. Exposure to cobalt oxide or cobalt chloride induced a concentration-dependent increase in intracellular Co levels in both human lung fibroblasts and epithelial cells (Figure 27). Epithelial cells took up less cobalt after cobalt oxide or cobalt chloride exposure compared to fibroblast cells. When we compared the cytotoxicity based on intracellular Co level, we found that epithelial and fibroblast cells exhibited similar level of toxicity after exposure to particulate or soluble cobalt (Figure 14). Thus, the decreased sensitivity of epithelial cells to cobalt was due to differences in uptake.

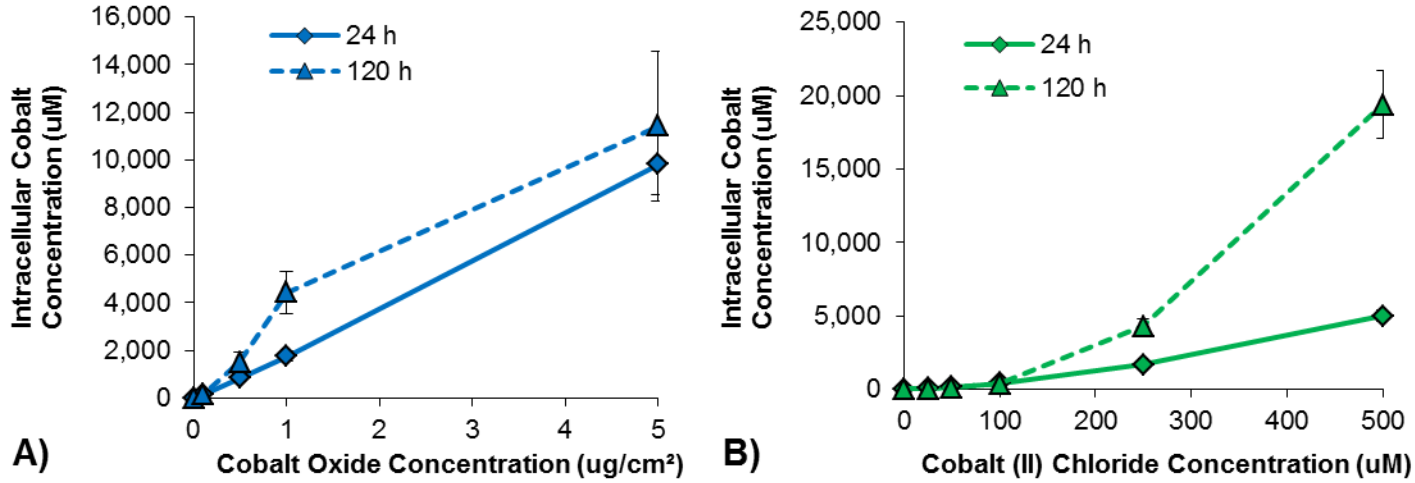

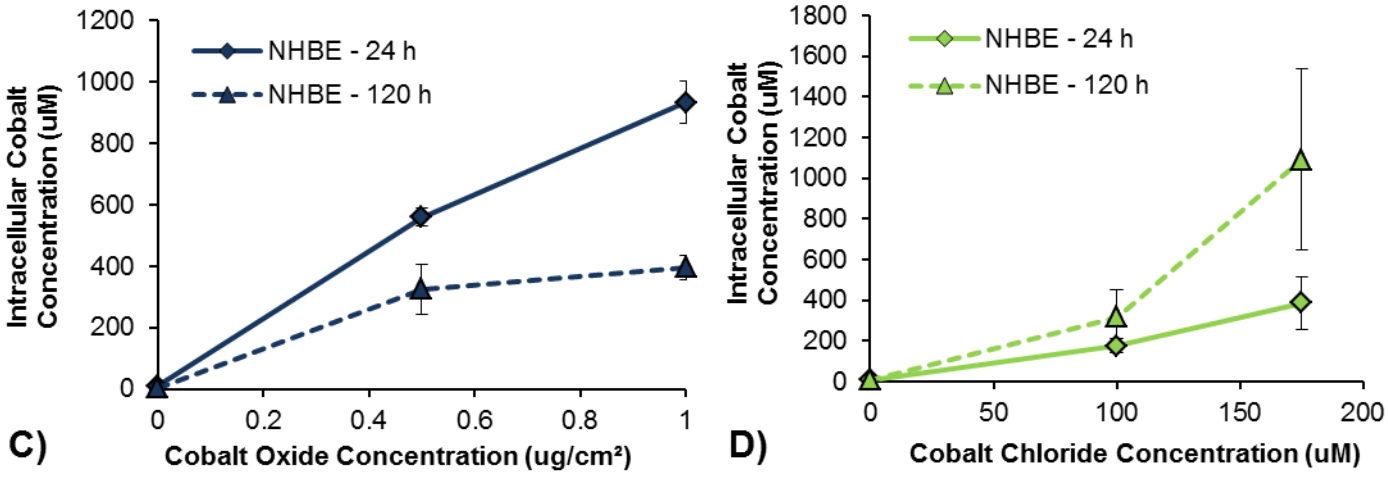

Figure 27. Intracellular Co Ion Levels after Exposure to Particulate and Soluble Cobalt in Human Lung Cells. Intracellular cobalt concentrations increased in a concentration-dependent manner after exposure to particulate or soluble cobalt in human lung cells. A) Cobalt oxide in human lung fibroblasts. B) Cobalt chloride in human lung fibroblasts. C) Cobalt oxide in human lung epithelial cells. D) Cobalt chloride in human lung epithelial cells. Data represent an average of 3 independent experiments +/- the standard error of the mean.

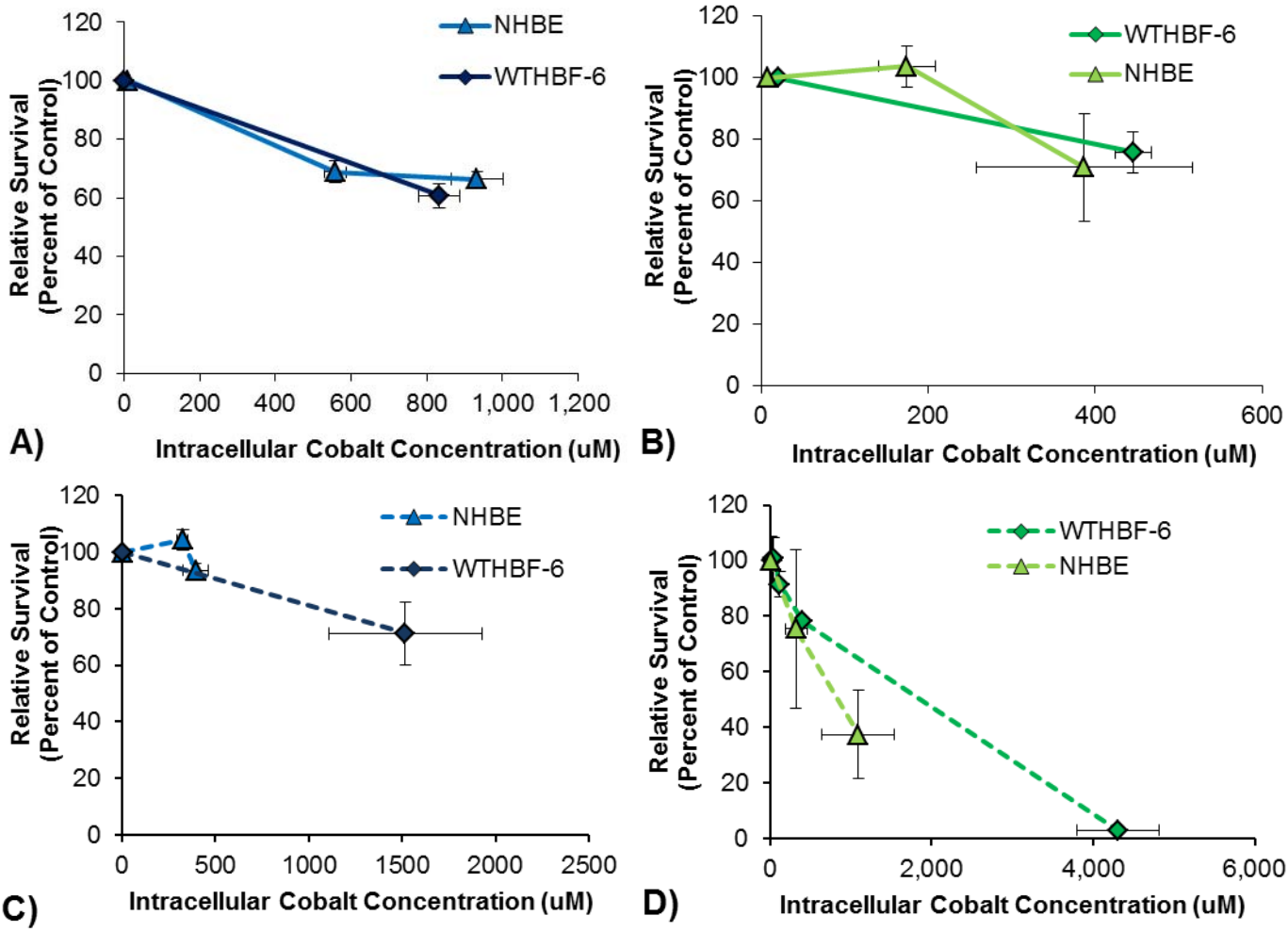

Figure 28. Comparison of Particulate and Soluble Cobalt-Induced Cytotoxicity in Human Lung Fibroblast and Epithelial Cells. Based on intracellular cobalt ion concentrations, soluble and particulate cobalt induced similar levels of cytotoxicity in human lung epithelial (NHBE) and fibroblast (WTHBF-6) cells. A)

Cobalt oxide, 24 h. B) Cobalt chloride, 24 h. C) Cobalt oxide, 120 h. D) Cobalt chloride, 120 h. Data represent an average of 3 independent experiments +/- the standard error of the mean.

Next, we compared the toxicity of particulate and soluble cobalt to determine if solubility played a role in the potency of cobalt compounds. Based on intracellular cobalt levels, soluble cobalt induces greater cytotoxicity than particulate cobalt in human lung fibroblast cells (Figure 29).

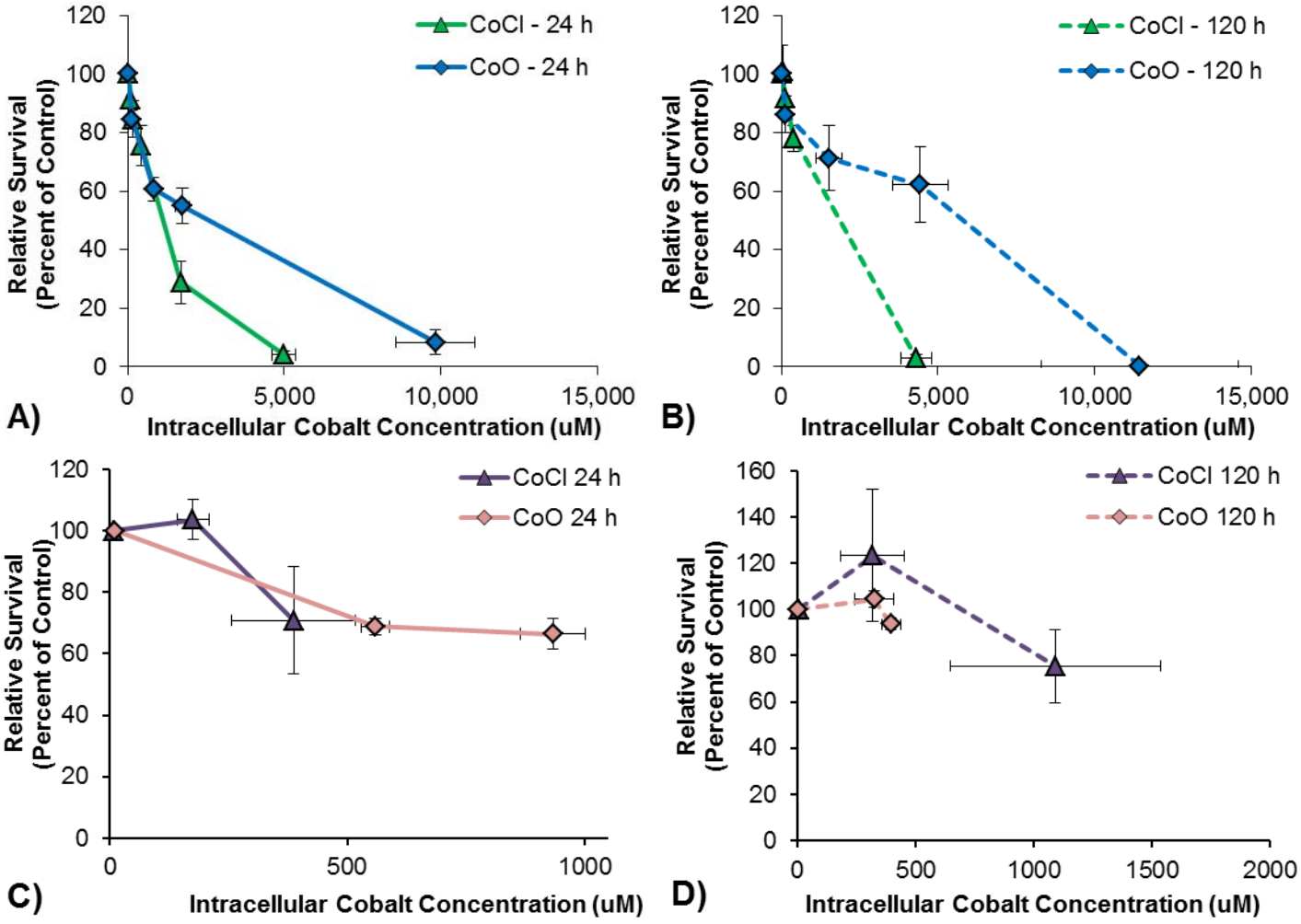

Figure 29. Comparison of Particulate and Soluble Cobalt-Induced Cytotoxicity. Based on intracellular cobalt ion concentration, soluble cobalt was more cytotoxic to human lung fibroblasts than particulate cobalt oxide. A) WTHBF-6 cells, 24 h. B) WTHBF-6 cells 120 h. However in human lung epithelial cells, there was no difference between particulate and soluble forms of cobalt. C) NHBF, 24h. D) NHBF, 120 h. Data represent an average of 3 independent experiments +/- the standard error of the mean.

We also sought to determine the role of the particle and ion in cobalt oxide-induced cytotoxicity using transwell dishes. To determine if intracellular cobalt ion levels originated from ions in the medium as a result of extracellular cobalt oxide dissolution or from particle internalization, cells were treated with cobalt oxide separated by a 0.2 um membrane. The cells on the top of the transwell dish were exposed to only cobalt ions and the cells on the bottom were exposed to cobalt oxide particles and dissolved cobalt ions. Table 1 shows that cells exposed to particles exhibited a much higher intracellular cobalt ion level than cells only exposed to the dissolved cobalt ions. These data indicate that particle internalization and subsequent dissolution is primarily responsible for the intracellular cobalt levels observed after cobalt oxide exposure. Consistent with the uptake data, relative survival was significantly higher in cells exposed to the particles compared to cells exposed only to the dissolved ions (Table 1). This work has been incorporated into two papers, one has been published (Smith, L.J., Holmes, A., Mason, M.D., Zheng, T., and Wise, Sr., J.P. The Cytotoxicity and

Genotoxicity of Soluble and Particulate Cobalt in Human Lung Fibroblast Cells. Toxicology and Applied Pharmacology, 278: 259-265, 2014) and the other is in preparation.

Table 1: Role of Particle-Cell Contact in Cobalt Oxide-Induced Cytotoxicity in Human Lung Fibroblast Cells

Cobalt Oxide Concentration (ug/cm^2)	Well Orientation	Intracellular Cobalt Concentration (uM)	Extracellular Cobalt Concentration (uM)	Relative Survival
0	Bottom	0	0	100 ± 0.0
0	Top	0	0	83.4 ± 7.0
5	Bottom	3,234	59	13.9 ± 2.7
5	Top	92	56	79 ± 13.5

Finally, we considered the effects of co-exposures of nickel and cobalt particles on human lung epithelial cells. Figure 16 shows the effect of cobalt and nickel co-exposures. Figures 30 A and B show the effect of cobalt on nickel toxicity which is exacerbated with chronic exposures. Figures 30 C and D show the effect of nickel co-exposure on cobalt toxicity (Figure 30C) which is exacerbated with chronic exposures (Figure 30D).

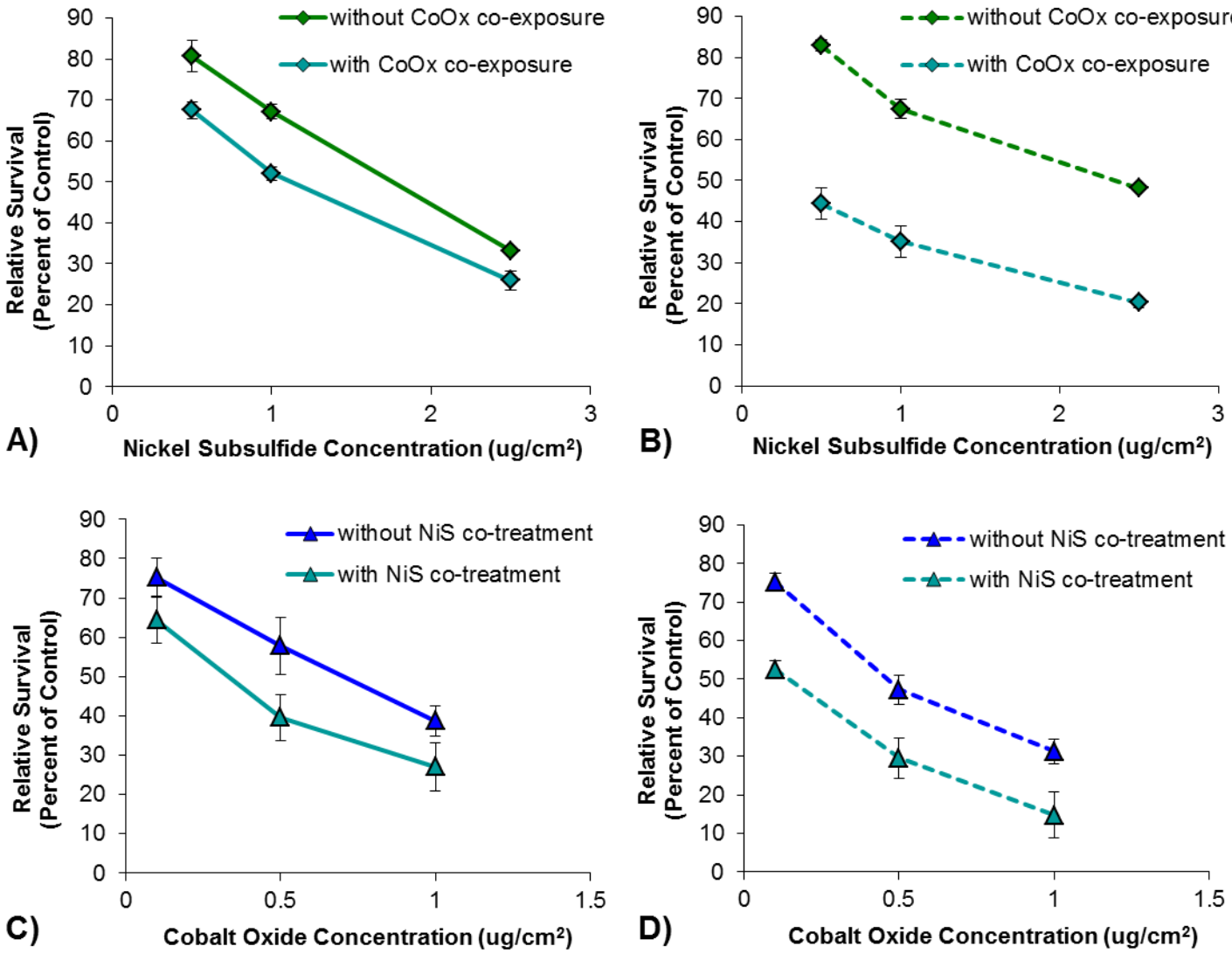

Figure 30. Cytotoxicity of Co-exposures of Particulate Nickel and Cobalt in Human Lung Cells. This figure shows that when human lung epithelial cells are exposed to both nickel and cobalt particles there is an increase in relative survival compared to nickel particles alone or cobalt particles alone. A) 24 h nickel with cobalt co-exposure. B) 120 h nickel with cobalt co-exposure. C) 24 h cobalt with nickel co-exposure. B) 120 h cobalt with nickel co-exposure. Cobalt co-treatments were treated with 0.1 ug/cm^2 cobalt oxide; nickel co-treatments were treated with 1 ug/cm^2 nickel subsulfide. Data represent an average of 3 independent experiments +/- the standard error of the mean.

4. Specific Aim #3: Demonstrate Metal Nanoparticle- and Microparticle-Induced Genotoxicity in Human Lung Cells

4.1. Genotoxicity of Nanoparticles

Our early investigations showed that low concentrations (up to 4 ug/cm^2) of bare, pegylated or FITC-coated silver nanoparticles did not induce chromosome damage (Figure 31). Our initial interpretation was that this lack of effect was due to the inability to achieve sufficient stock concentrations of the silver colloid solutions. However, once the production issues were worked out and we were able to work with higher stock concentrations of silver nanoparticles we found that we were still unbale to achieve a genotoxic effect (Figure 32). Similarly, we found no effect with the thiol-pegylated silver nanoparticles (Figure 33).

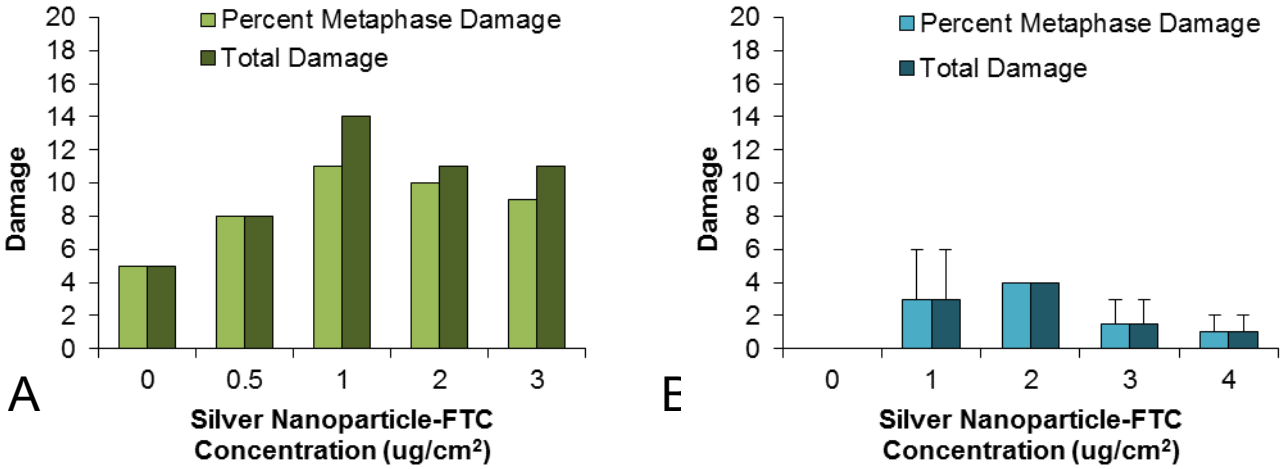

Figure 31. Clastogenicity of FTC Silver Nanoparticles. This figure shows the clastogenicity of FTC silver nanoparticles. A) FTC silver nanoparticles are weakly genotoxic after a 24 h exposure. Data represent one experiment. B) FTC silver nanoparticles are not genotoxic to human lung fibroblasts after a 120 h exposure. Data represent an average of 2 independent experiments ± the standard error of the mean.

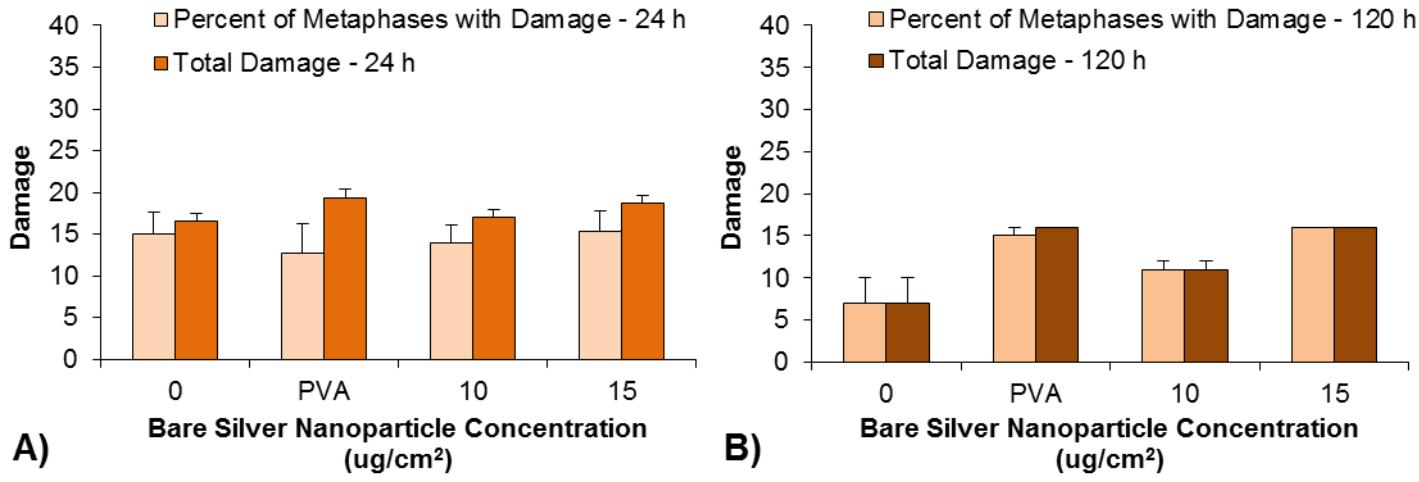

Figure 32. Clastogenicity of Bare Silver Nanoparticles in Human Lung Cells. This figure shows that a 24 or 120 h exposure to bare silver nanoparticles did not induce chromosome damage in human lung cells. PVA = polyvinyl alcohol as the vehicle control. A) 24 h. B) 120 h. Data represent an average of 3 or 4 experiments +/- the standard error of the mean for 24 h and 1 or an average of 2 experiments +/- the standard error of the mean for 120 h.

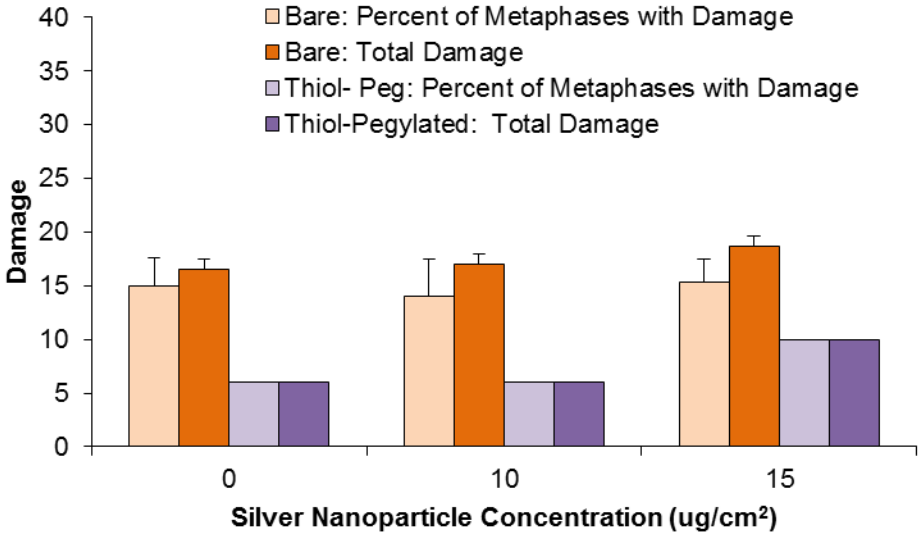

Figure 33. Clastogenicity of Silver Nanoparticles in Human Lung Cells. This figure shows that bare and pegylated silver nanoparticles did not induce chromosome damage in human lung cells after 24 h treatment. Data represent an average of 3 or 4 experiments +/- the standard error of the mean for bare and 1 experiment for pegylated.

As mentioned in the previous section on cytotoxicity, we terminated investigations on the cytotoxicity and genotoxicity of gold nanostars because of the inability to generate concentrated stock solutions to achieve appropriate treatment doses. Instead, we focused on higher concentrations of bare gold nanospheres and found that gold nanospheres induce little or no genotoxicity (Figure 34).

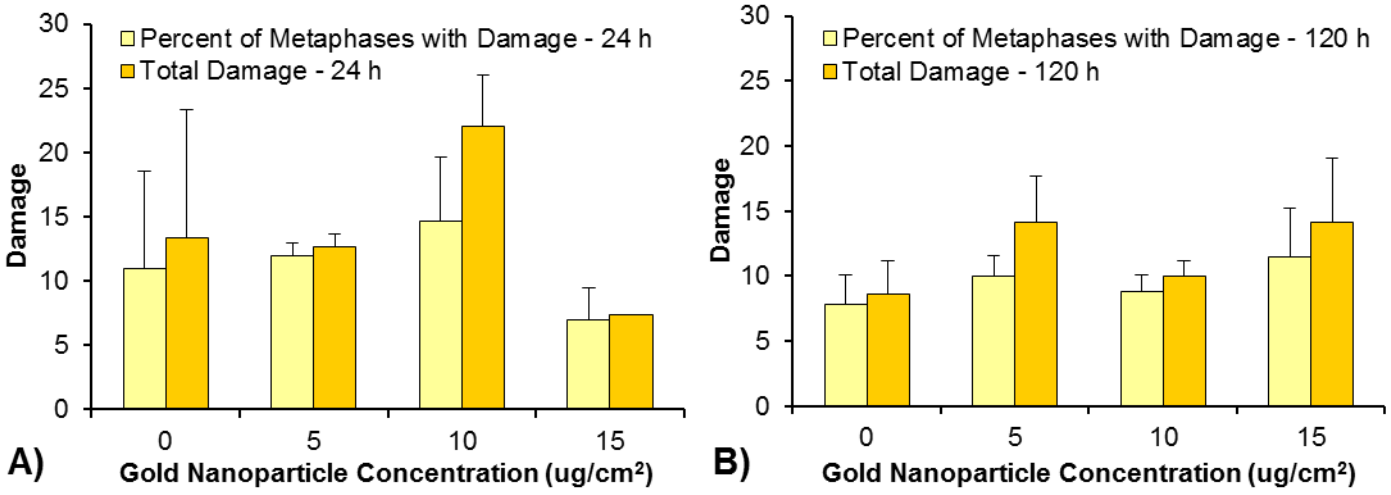

Figure 34. Clastogenicity of Gold Nanoparticles in Human Lung Cells. This figure shows that a 24 or 120 h induced minimal to no chromosome damage in human lung cells. A) 24 h. B) 120 h. Data represent 1 experiment or an average of 3 experiments +/- the standard error of the mean for 24 h or 4-5 experiments +/- the standard error of the mean for 120 h.

We also determined the clastogenicity of titanium dioxide nanoparticles and found that these particles do not induce chromosome damage in human skin cells after an acute or chronic exposure, even at concentrations as high as 100 ug/cm^2 titanium dioxide nanoparticles (Figure 35). Considering the lack of cytotoxicity in response to titanium dioxide nanoparticles, we discontinued the titanium dioxide project, but these data were incorporated into a paper that has been published: Browning, C., The, T., Mason, M.D. and Wise, Sr., J.P. Titanium Dioxide Nanoparticles Are Not Cytotoxic or Clastogenic in Human Skin Cells. Journal of Environmental and Analytical Toxicology, 4-6: 1-6, 2014.

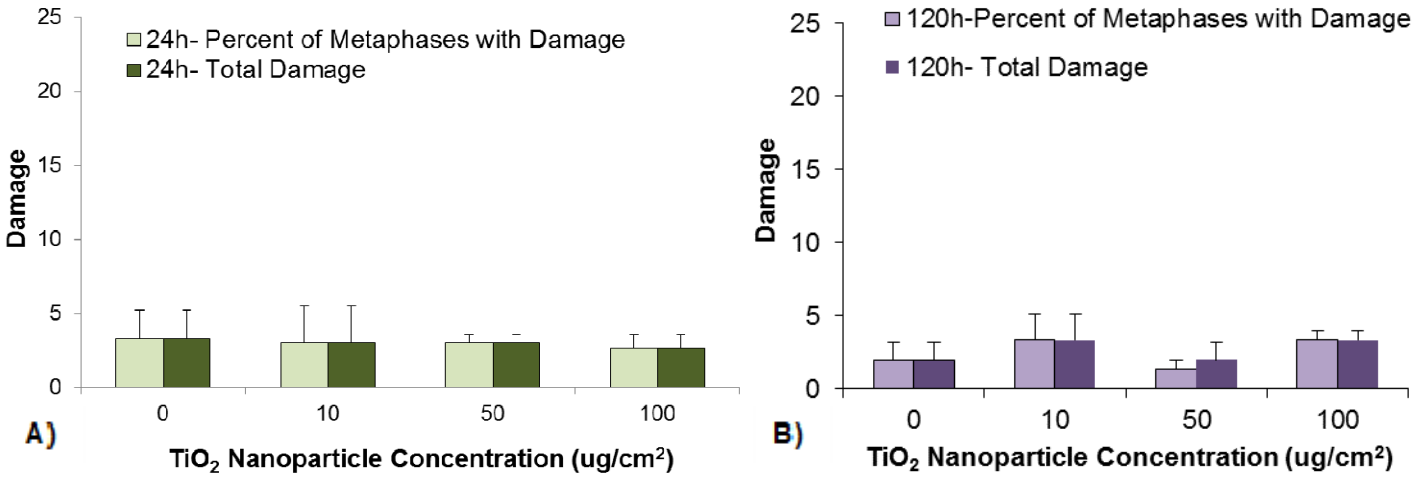

Figure 35. Clastogenicity of Titanium Dioxide Nanoparticles in Human Skin Cells. This figure shows that titanium dioxide nanoparticles do not induce chromosome damage in human skin cells after a 24 h (Panel A) or a 120 h (Panel B) exposure. Data represent an average of 3 independent experiments +/- the standard error of the mean.

4.2. Genotoxicity of Particles Associated with Metal-on-Metal Hip Implants

We assessed the genotoxicity of CoCrMo nanoparticles in human urothelial cells. Our data indicate that CoCrMo nanoparticles induce low levels of chromosome damage that do no increase with dose in human urothelial cells after chronic exposure, but they do induce cell cycle arrest at higher concentrations (Figure 36). No metaphases were observed after exposure to 10 ug/cm^2 CoCrMo nanoparticles for 120 h.

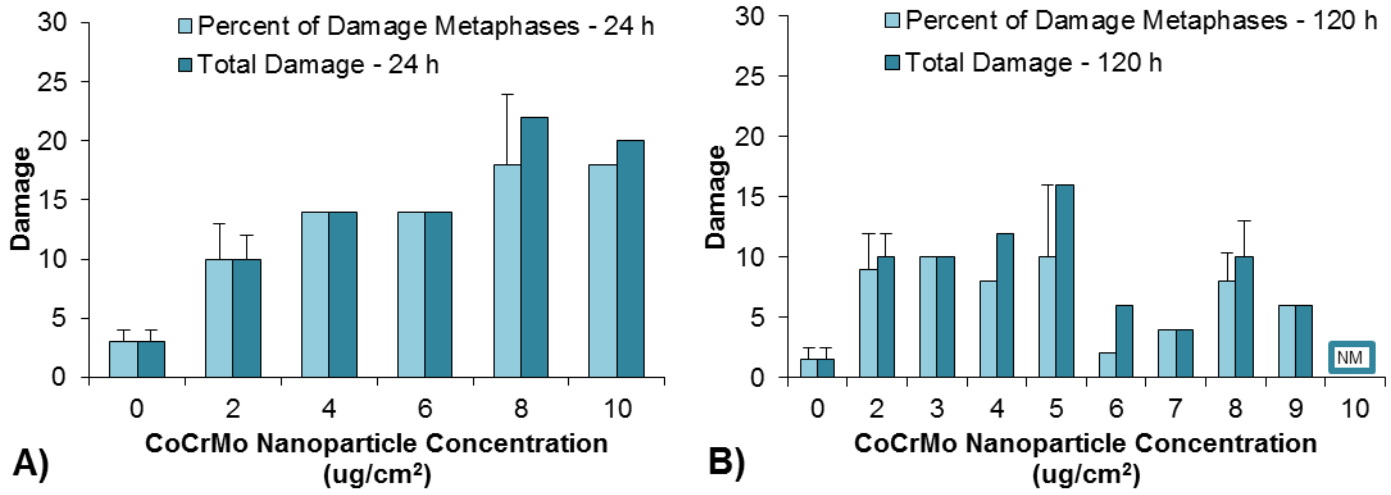

Figure 36. Clastogenicity of CoCrMo Nanoparticles in Human Urothelial Cells. This figure shows that CoCrMo nanoparticles induced a concentration-dependent increase in chromosome damage in human urothelial cells after 24 h treatment. Chronic exposures to CoCrMo nanoparticles does not induce a

concentration-dependent increase. 10 ug/cm^2 CoCrMo nanoparticles exhibited no metaphases (NM). Data represent 1-2 experiments +/- the standard error of the mean.

We also considered CoCrMo nanoparticles generated from an actual hip implant. Figure 37 shows preliminary data on the genotoxicity of these hip nanoparticles in the human urothelial cell line, hTU1-38.

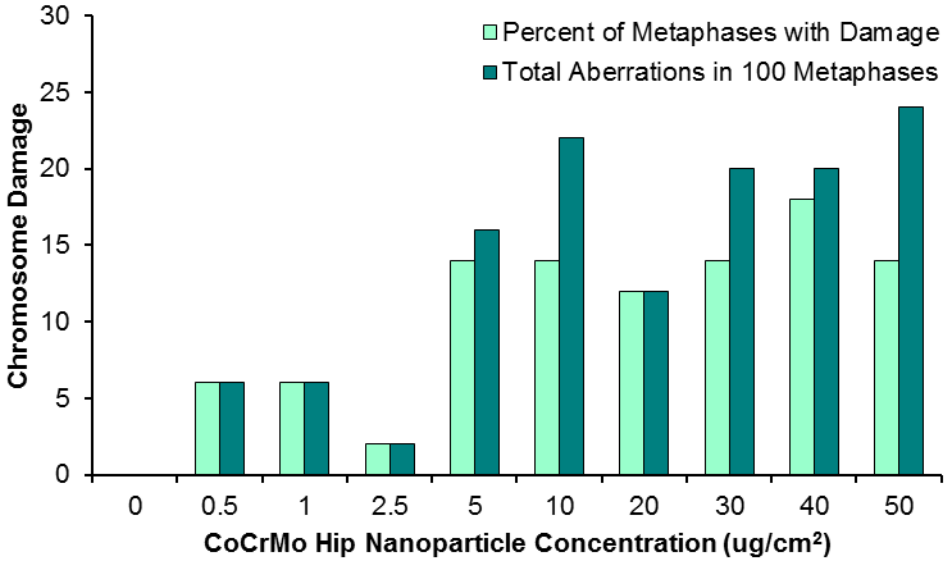

Figure 37. Clastogenicity of CoCrMo Hip Nanoparticles in Human Urothelial Cells. This figure shows that chronic exposure to CoCrMo nanoparticles generated from an actual hip implant induced low levels of chromosome damage in human urothelial cells after 24 h treatment. Data represent one experiment.

We also considered the effect of the individual elements which may be released from hip wear to try to understand the contribution of each type of element to urothelial toxicity. We considered the genotoxic effect of Cr(III), Cr(VI), Co and Mo particles in a human urothelial cell line (hTU1-38), their target organ. Chromium oxide did not induce an increase in the amount of chromosome damage after 24 h treatment (Figure 38 A); 120 h chromosome analysis is pending. Lead chromate and cobalt oxide induced a concentration-dependent increase in genotoxicity at 24 and 120 h (Figure 38 B,C,D, and E).

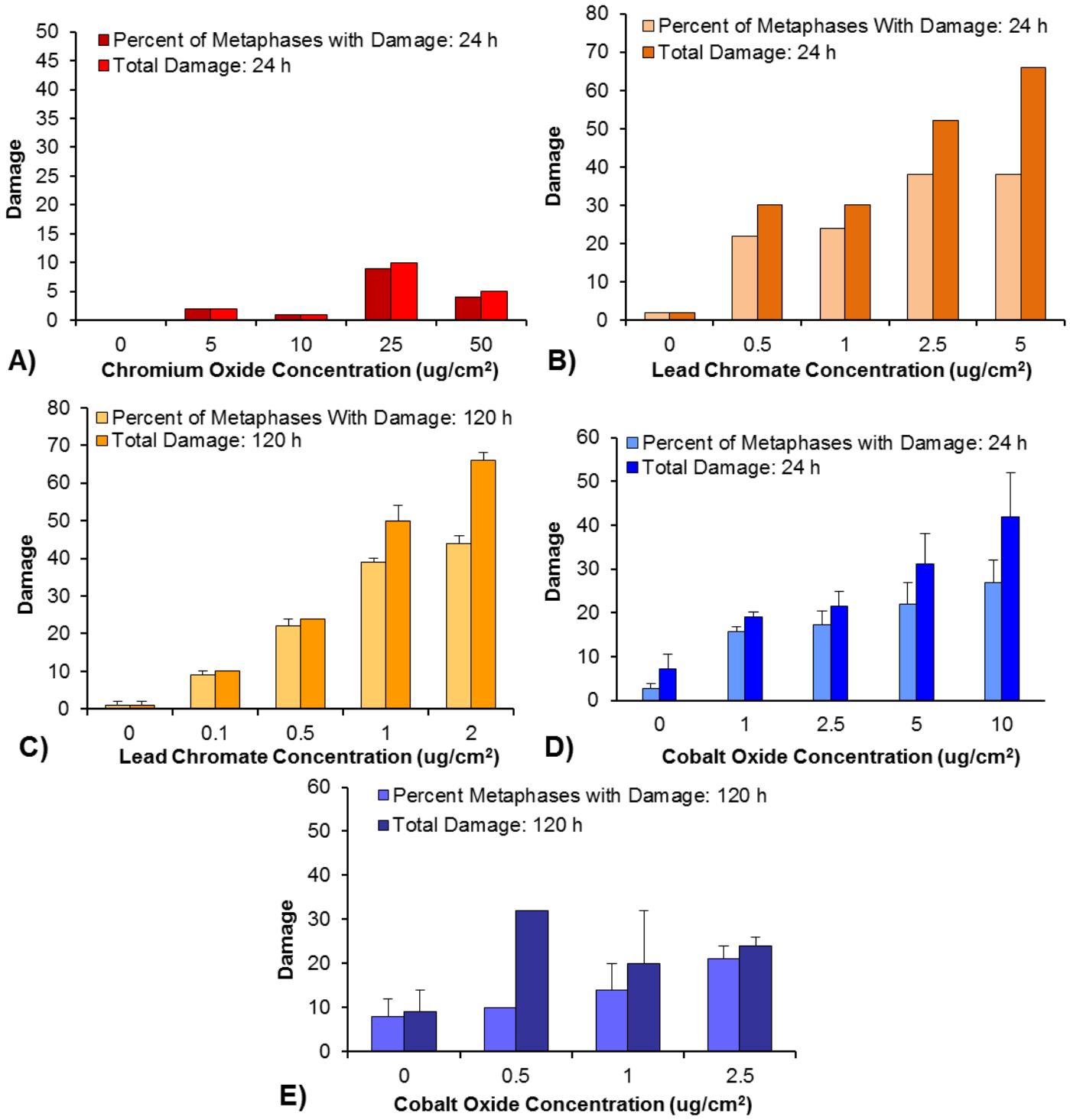

Figure 38. Genotoxicity of Hip Implant Component Particles in Human Urothelial Cells. This figure shows the genotoxic effect of hip implant component particles in human urothelial cells after 24 or 120 h treatment. A) 24 h Chromium oxide (Cr(III)). B) 24 h Lead chromate (Cr(VI)). C) 120 h Lead chromate (Cr(VI)). D) 24 h Cobalt oxide. E) 120 h Cobalt oxide. Data represent 1-4 experiments +/- the standard error of the mean.

4.3. Genotoxicity of Metal Microparticles of Military Concern

We evaluated the clastogenicity of nickel and cobalt compounds. We found a concentration-dependent increase in chromosome damage in both human lung fibroblasts and epithelial cells with nickel treatment (Figure 39-40). More chronic exposures induced cell cycle arrest after exposure to 1 ug/cm^2 nickel subsulfide

(Figure 39 B). In human lung epithelial cells, we found that nickel subsulfide induced both a concentration- and time-dependent increase in chromosome damage (Figure 40). The findings in epithelial cells were published this year in Holmes, A.L., The, T., Thompson, K., Mason, M., Kandpal, S., Zheng, T., and Wise, Sr., J.P. Chronic Exposure to Particulate Nickel Induces Neoplastic Transformation in Human Lung Epithelial Cells. Toxics, 1(1): 46-59, 2013. doi:10.3390/toxics1010046.

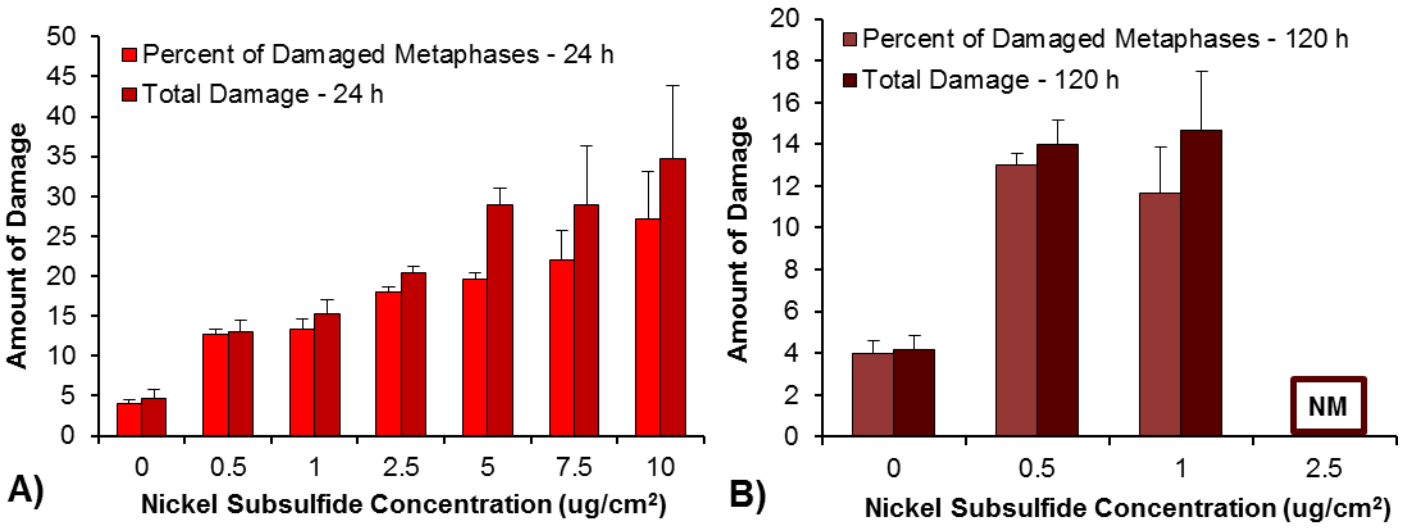

Figure 39. Clastogenicity of Nickel Sulfide in Human Lung Fibroblast Cells. This figure shows that both acute and chronic exposure to nickel subsulfide induced a concentration-dependent increase in chromosome damage in human lung fibroblast cells. Chronic exposure induced cell cycle arrest at low concentrations (2.5 ug/cm^2 nickel sulfide and above) compared to 24 h. A) 24 h. B) 120 h. NM = no metaphases. Data represent an average of 3 independent experiments +/- the standard error of the mean.

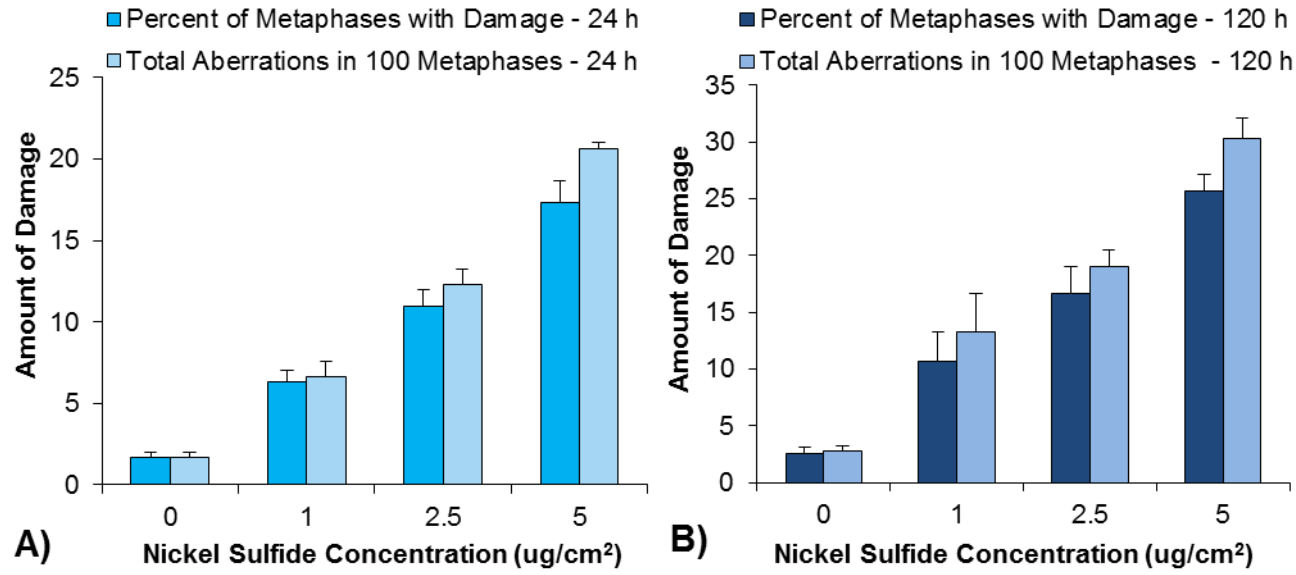

Figure 40. Clastogenicity of Nickel Sulfide in Human Lung Epithelial Cells. This figure shows that acute and chronic exposure to nickel subsulfide induced a concentration-dependent increase in chromosome damage in human lung epithelial cells. A) 24 h. B) 120 h. Data represent an average of 3 independent experiments +/- the standard error of the mean.

Exposure to particulate cobalt for 24 or 120 h induced a concentration-dependent increase in chromosome damage (Figure 41). Interestingly, acute exposure to cobalt oxide induced more chromosome damage than chronic exposure. Exposure to 2.5 ug/cm^2 cobalt oxide for 120 h resulted in cell cycle arrest and no

metaphases were observed. Cobalt chloride induced a small increase in chromosome damage after 24 h exposure which decreased with more chronic exposures (Figure 42). Despite the low level of chromosome damage, cobalt chloride-treated cells exhibited cell cycle arrest after a 24 h exposure to 500 uM cobalt chloride or a 120 h exposure to 250 uM cobalt chloride. Data for the 24 h exposures has been published: Smith, L.J., Holmes, A., Mason, M.D., Zheng, T., and Wise, Sr., J.P. The Cytotoxicity and Genotoxicity of Soluble and Particulate Cobalt in Human Lung Fibroblast Cells. Toxicology and Applied Pharmacology, 278: 259-265, 2014.

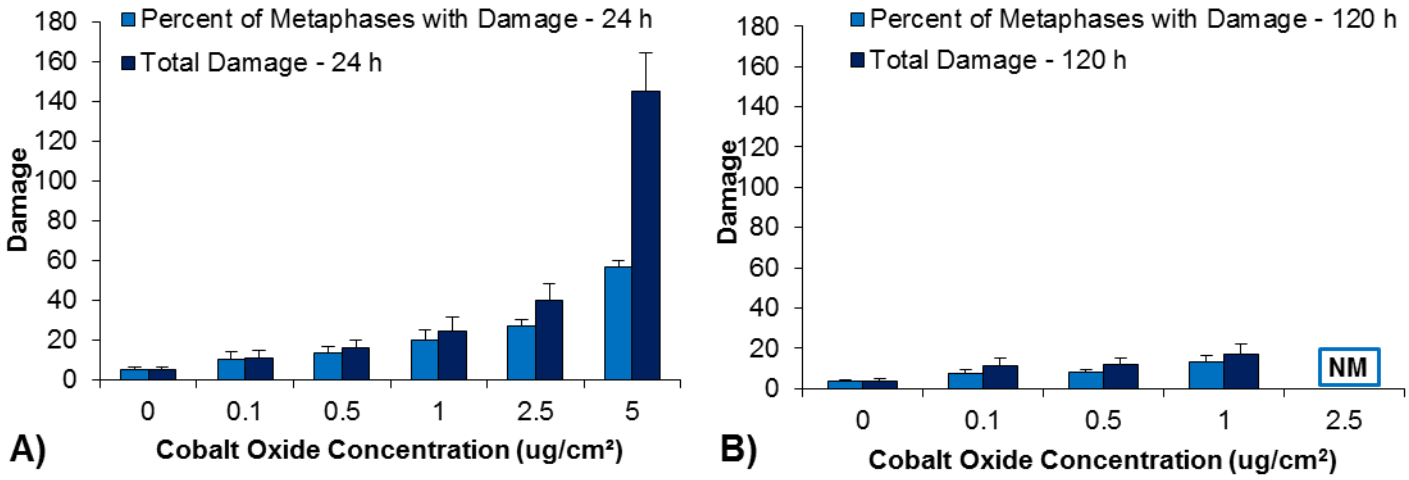

Figure 41. Clastogenicity of Cobalt Oxide in Human Lung Cells. This figure shows that exposure to cobalt oxide induced chromosome damage in human lung cells. A) A 24 h exposure induced a concentration-dependent increase in chromosome damage. B) Exposure to cobalt oxide for 120 h induced a small concentration-dependent increase chromosome damage with no metaphase (NM) observed at 2.5 ug/cm^2 cobalt oxide. Data represent an average of 3 independent experiments +/- the standard error of the mean.

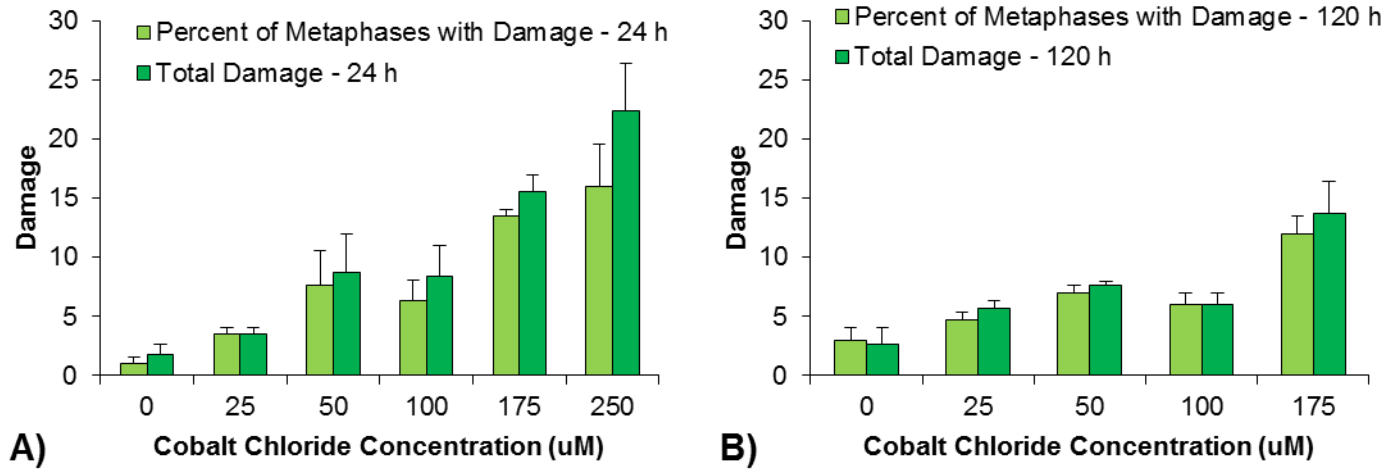

Figure 42. Clastogenicity of Cobalt Chloride in Human Lung Cells. This figure shows that exposure to cobalt chloride induced a minimal increase in chromosome damage in human lung cells. A) Exposure to cobalt chloride for 24 h induced a small concentration-dependent increase in chromosome damage. B) Exposure to cobalt chloride for 120 h induces minimal chromosome damage in human lung cells. Data represent an average of 3 independent experiments +/- the standard error of the mean.

Next, we investigated if cobalt induced similar clastogenic effects in primary lung epithelial cells. Particulate and soluble cobalt induced a concentration-dependent increase in chromosome damage in lung epithelial cells (Figure 43 A,C). Based on intracellular cobalt concentrations, cobalt oxide induced similar levels of

chromosome damage in lung fibroblast and epithelial cells (Figure 43 B). Cobalt chloride also induced similar levels of chromosome damage in lung epithelial and fibroblast cells at lower concentrations, but at higher concentrations, lung epithelial cells appeared to be more prone to cobalt chloride-induced genotoxicity (Figure 43 D).

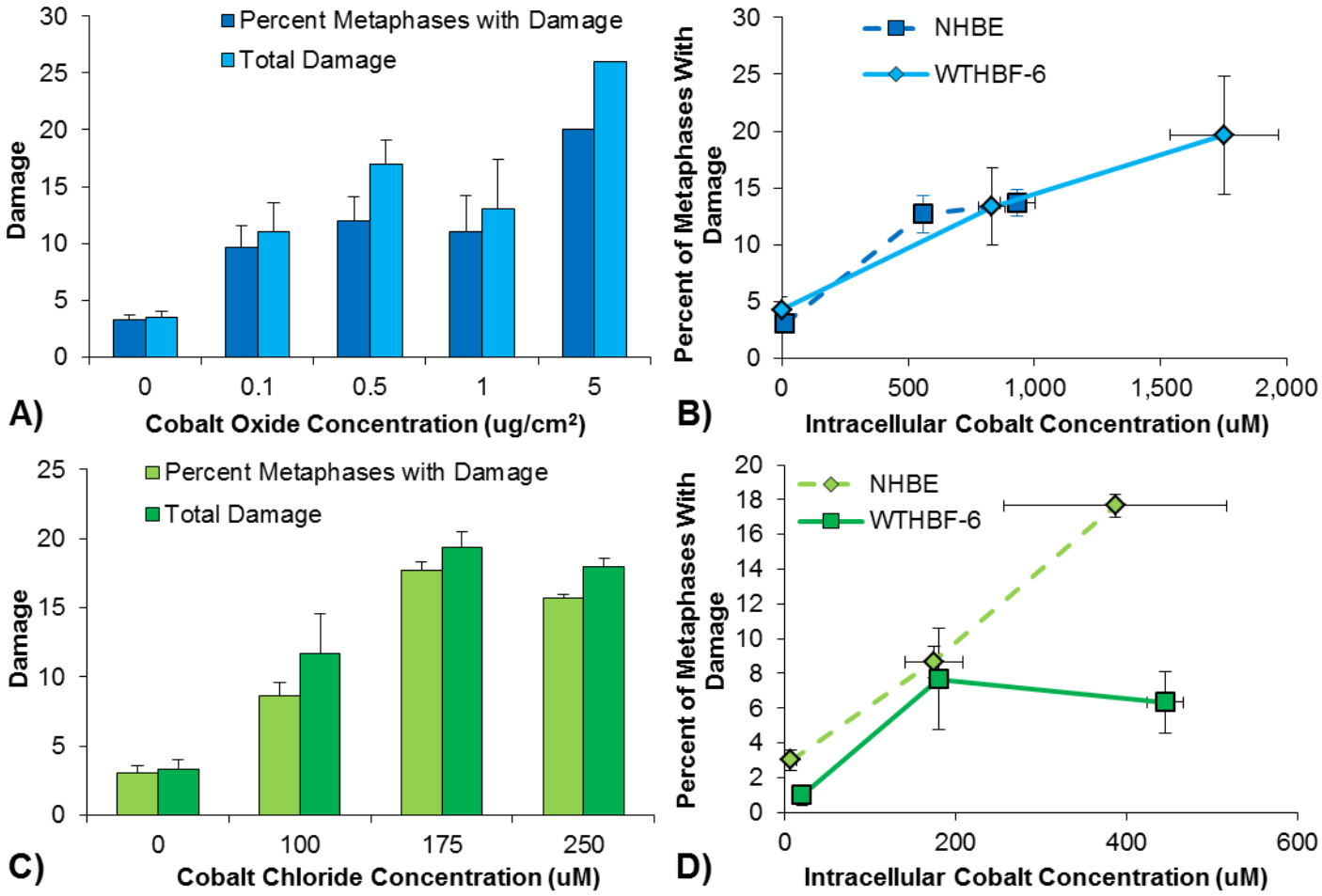

Figure 43. Clastogenicity of Particulate and Soluble Cobalt in Human Lung Epithelial Cells. This figure shows that exposure to cobalt chloride or cobalt oxide induced chromosome damage in human lung epithelial cells. A) Exposure to cobalt oxide for 24 h induced a concentration-dependent increase in chromosome damage in human lung epithelial cells. B) Based on intracellular cobalt concentration, cobalt oxide induced similar levels of chromosome damage in human lung epithelial (NHBE) and fibroblast (WTHBF-6) cells. C) Exposure to cobalt chloride for 24 h induced a small concentration-dependent increase in chromosome damage in human lung epithelial cells. D) Based on intracellular cobalt concentration, cobalt chloride induced similar levels of chromosome damage in human lung epithelial (NHBE) and fibroblast (WTHBF-6) cells at lower concentrations. Data represent an average of 3 independent experiments +/- the standard error of the mean.

When we compared particulate and soluble cobalt based on intracellular cobalt concentration, we found that acute exposure to soluble and particulate cobalt induced similar levels of chromosome damage (Figure 44 A). Interestingly, cells exposed to cobalt chloride exhibited cell cycle arrest at a much lower intracellular cobalt concentration than after particulate cobalt exposure. However, with cobalt oxide, metaphases with high levels of chromosome damage were still observed at intracellular cobalt ion concentrations up to 9,800 uM. Chronic exposure to particulate and soluble cobalt revealed a similar trend as acute exposure (Figure 44 B). These data are now complete and being prepared for publication.

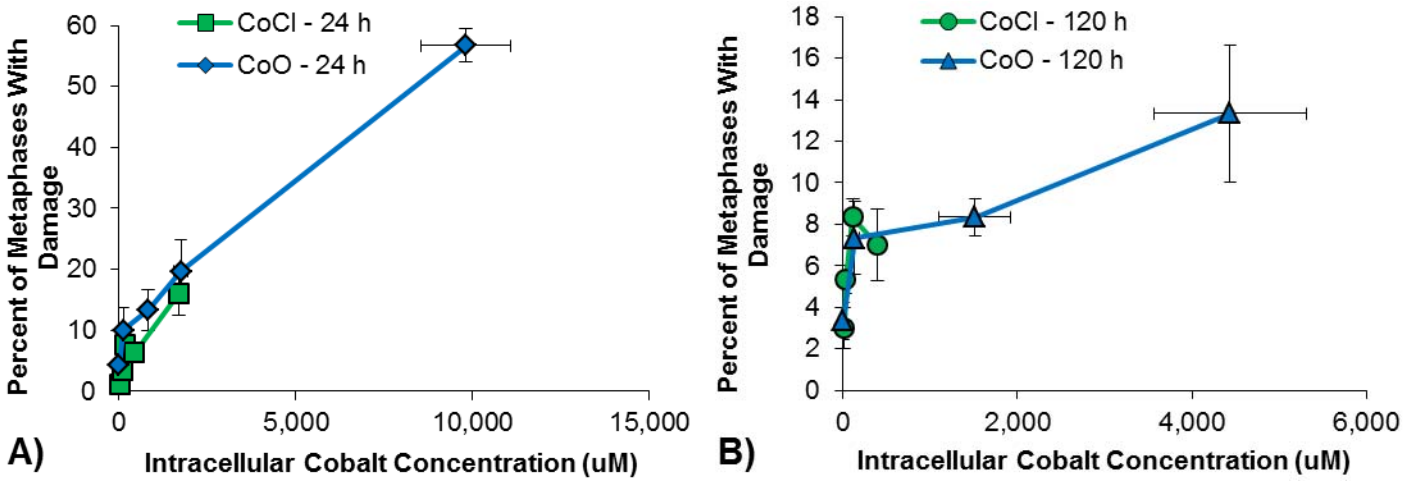

Figure 44. Comparison of Particulate and Soluble Cobalt-Induced Clastogenicity. Particulate and soluble cobalt induced similar levels of chromosome damage based on intracellular cobalt levels. Cell cycle arrest was observed at a lower intracellular cobalt level with cobalt chloride compared to cobalt oxide. A) 24 h. B) 120 h. Data represent an average of 3 independent experiments +/- the standard error of the mean.

Next, we sought to determine the role of the particle and ion in cobalt oxide-induced clastogenicity using transwell dishes. Table 2 shows that cells exposed to particles exhibited much higher levels of chromosome damage compared to cells only exposed to the dissolved cobalt ions, indicating that particle internalization is required for cobalt oxide-induced clastogenicity. These data were included in the Smith, L.J., et al., 2014 publication.

Table 2: Role of Particle-Cell Contact in Cobalt Oxide-Induced Clastogenicity in Human Lung Fibroblast Cells

Cobalt Oxide Concentration (ug/cm^2)	Well Orientation	Intracellular Cobalt Concentration (uM)	Extracellular Cobalt Concentration (uM)	Percent of Metaphases with Damage	Total Damage
0	Bottom	0	0	4.3 ± 0.9	5.3 ± 0.7
0	Top	0	0	6.0 ± 1.0	6.7 ± 1.7
5	Bottom	6854	54	45.0 ± 5.7	103.3 ± 29.4
5	Top	140	58	8.7 ± 1.3	10.3 ± 1.7

We also considered the effect of co-exposures of nickel and cobalt as exposures to both metal particulates is frequent. Co-exposure to cobalt does not exacerbate the effect of nickel exposure in human lung epithelial cells (Figure 45). The effects of co-treatment with cobalt and nickel are similar to the effect of adding the effects of the individual exposures at both 24 and 120 h treatment times.

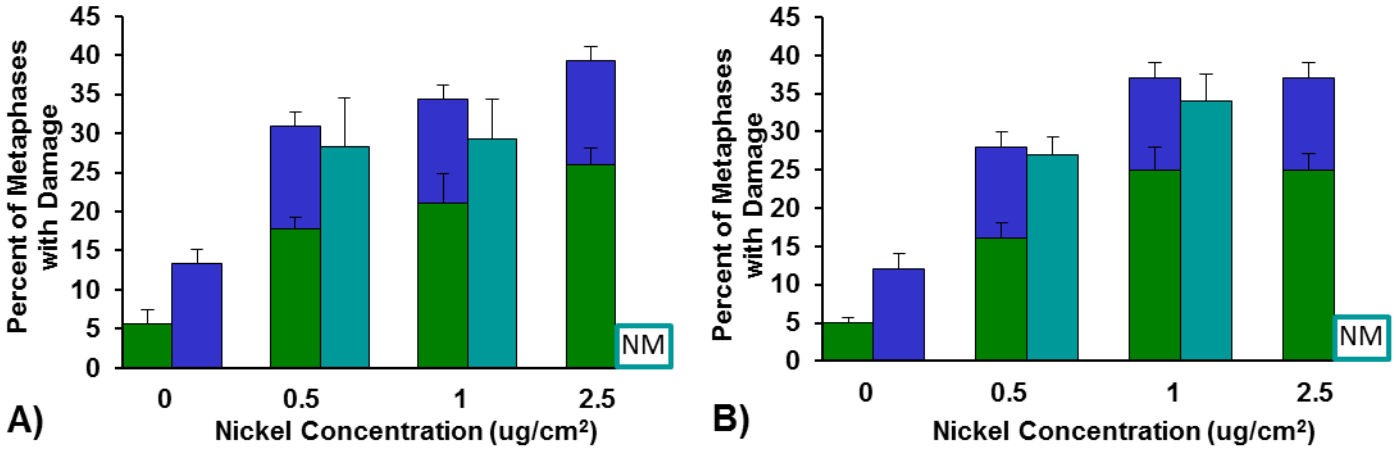

Figure 45. Clastogenicity of Nickel and Cobalt Co-Exposure in Human Lung Epithelial Cells. This figure shows the clastogenicity of nickel and cobalt co-treatments in human lung epithelial cells. A) 24 h. B) 120 h. NM = no metaphases. Data represent an average of 3 independent experiments +/- the standard error of the mean.

Under previous grants we have address the clastogenicity and carcinogenicity of particulate DU in human lung epithelial cells. This year, we extended those studies and began to investigate DU-induced DNA double strand break formation and repair. We found that exposure to 25 ug/cm^2 uranium trioxide induced DNA double strand breaks in human lung epithelial cells but no time-dependent increase was observed (Figure 46).

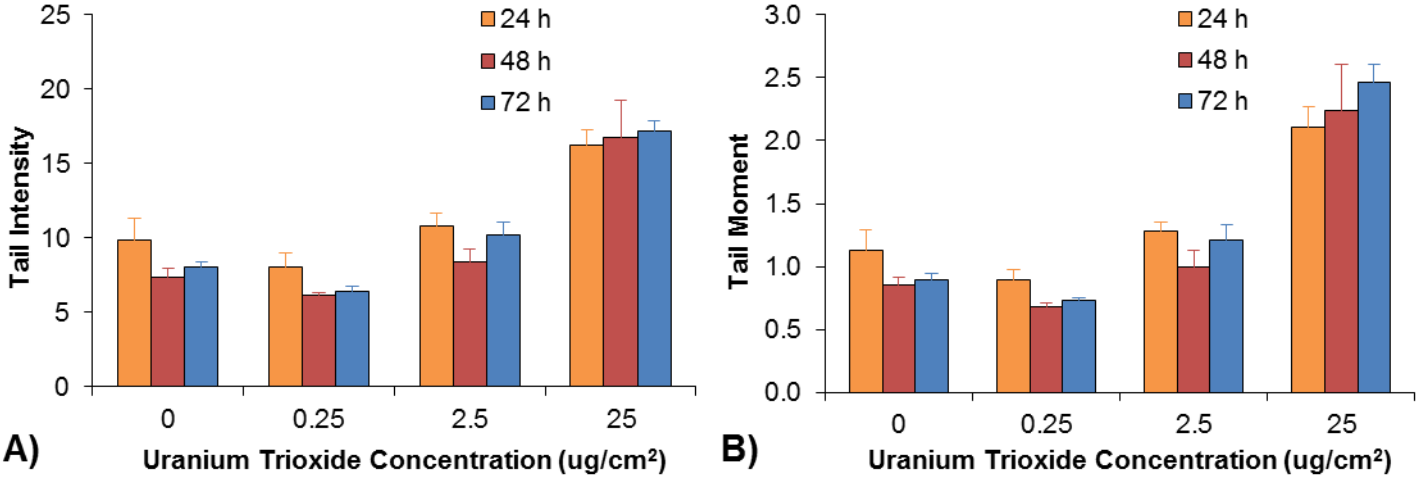

Figure 46. DNA Double Strand Break Induction after Exposure to Particulate DU. This figure shows that DU induced DNA double strand breaks after exposure to 25 ug/cm^2 uranium trioxide in human lung epithelial cells. A) Tail intensity. B) Tail moment. Data represent an average of 3 independent experiments +/- the standard error of the mean.

Next we investigated the effects of DU on DNA repair protein expression. Data show that DU-induced DNA double strand breaks activate ATM kinase activity, promoting the phosphorylation of proteins involved in both checkpoint activation and DNA repair (Figure 47 A, B). Interestingly, Rad51, an important protein in HR repair pathway and Tip60, a histone acetyltransferase, are inhibited (Figure 47 A, E, G). In addition, we tested the foci formation of some of these proteins. We found that pATM foci declined over time and were reduced at the highest concentration (25 ug/cm^2) (Figure 47 C). Nuclear Rad51 foci increased after uranium treatment at all time points (Figure 47 F). These data suggest that DU may affect the HR repair pathway and histone modification coordinated DNA repair.

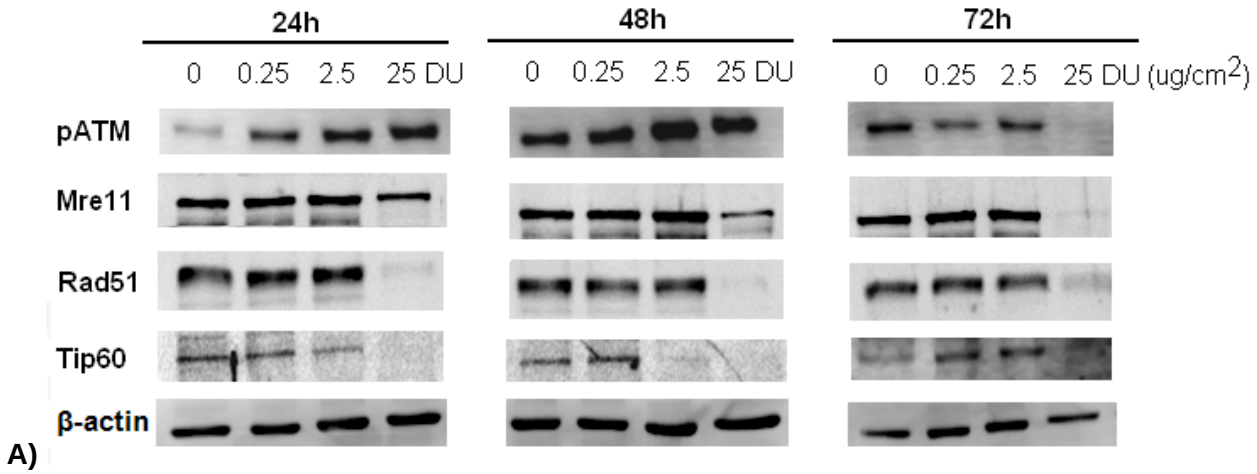
24h
48h
72h
0 0.25 2.5 25 DU
0 0.25 2.5 25 DU
0 0.25 2.5 25 DU (ug/cm2)
pATM
Mre11
Rad51
Tip60
β-actin

A)

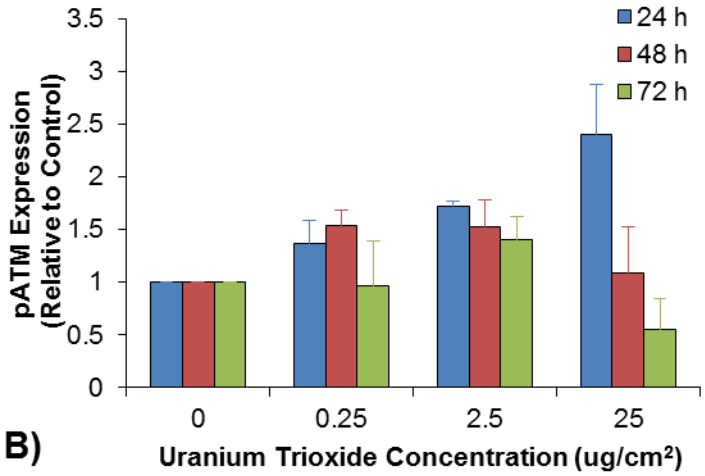
24 h
48 h
72 h
pATM Expression (Relative to Control)
Uranium Trioxide Concentration (ug/cm²)

B)

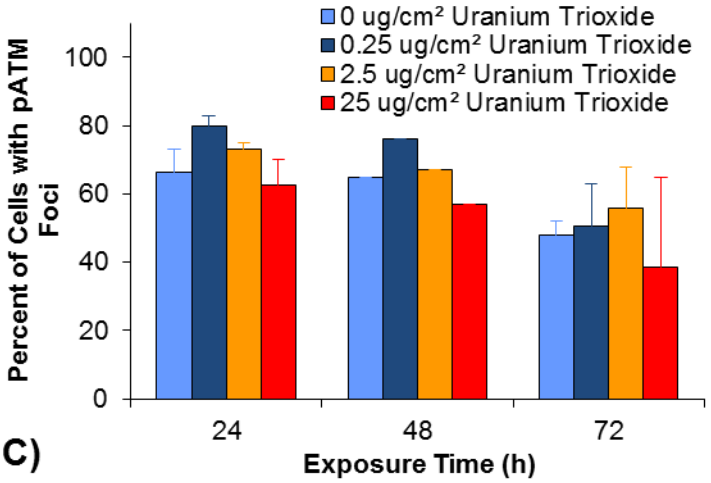
0 ug/cm² Uranium Trioxide
0.25 ug/cm² Uranium Trioxide
2.5 ug/cm² Uranium Trioxide
25 ug/cm² Uranium Trioxide
Percent of Cells with pATM Foci
Exposure Time (h)

C)

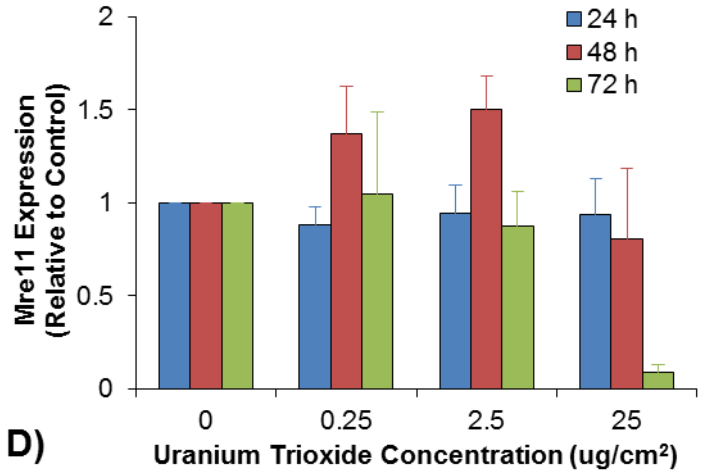
24 h
48 h
72 h
Mre11 Expression (Relative to Control)
Uranium Trioxide Concentration (ug/cm²)

D)

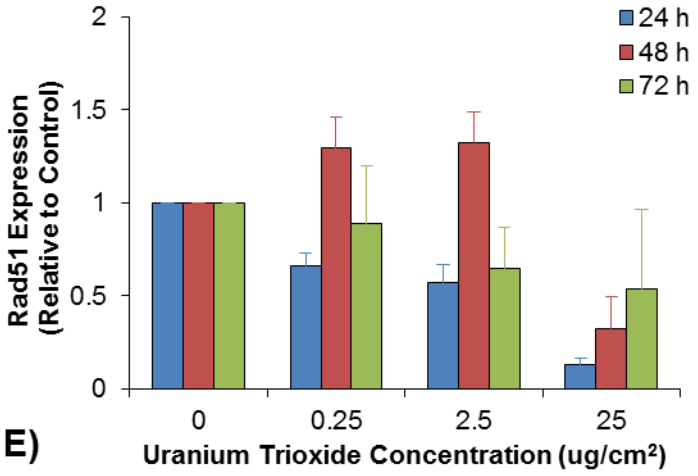
24 h
48 h
72 h
Rad51 Expression (Relative to Control)
Uranium Trioxide Concentration (ug/cm²)

E)

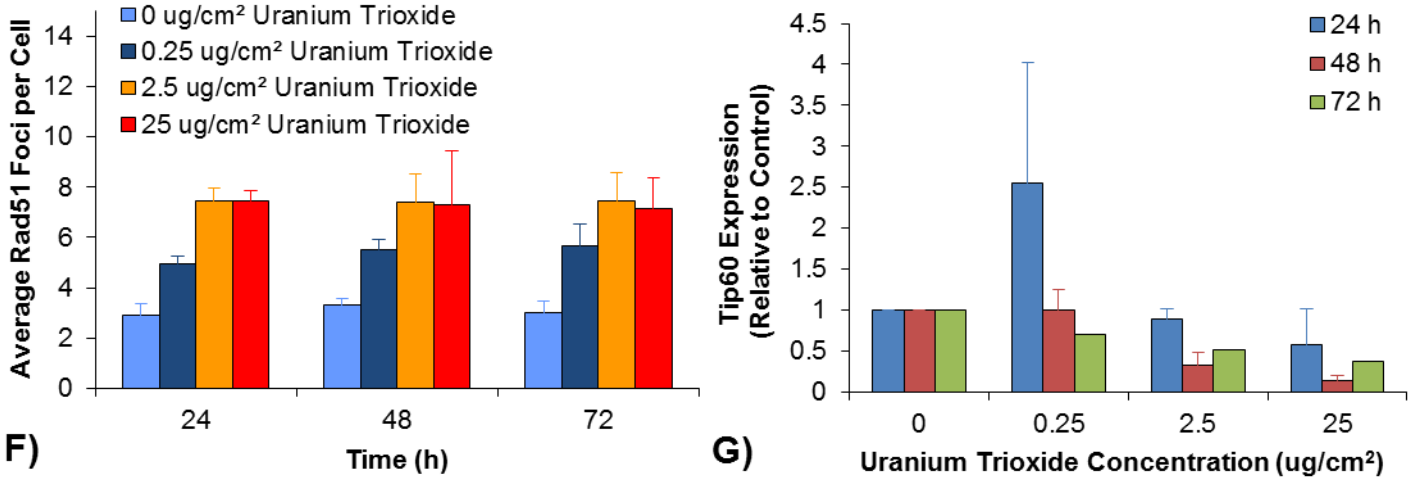

Figure 47. Exposure to DU Changes DNA Double Strand Break Repair Protein Levels. This figure shows that chronic exposure to DU induces alterationsin DNA double strand break repair protein, Mre11, pATM, Rad51 and Tip60 expression levels. A) Representative western blot image for pATM, Mre11, Rad51 and Tip60. B) Exposure to uranium trioxide for 24 and 48 h increases pATM expression levels while a 72 h exposure decreases pATM expression at a high concentration. C) Number of cells with pATM foci declines over the time while reduction occurs at a high concentration. D) Exposure to DU for 24 h induces no change on Mre11 level while 48 h exposure induces an increase at lower concentrations. Exposure to uranium trioxide eliminated Mre11 expression at high concentrations at 72 h. E) 24 h and 72 h exposure induces a concentration-dependent decrease in Rad51 expression level while 48 h exposure only decreases Rad51 expression at 25 ug/cm^2 uranium trioxide. F) Uranium trioxide induces increase in Rad51 foci level with all three time points. G) Tip60 expression increases after exposure to low concentrations (0.25 ug/cm^2) of uranium trioxide for 24 h but decreases at higher concentrations. 48 h and 72 h exposure induces a concentration-dependent decrease in Tip60 levels. Data represent an average of 2-6 experiments +/- the standard error of the mean.

We investigated he role of homologous recombination repair in DU-induced DNA damage using a series of CHO cell lines deficient in XRCC3 or RAD51D. This work was published: Holmes, A.L., Joyce, K., Falank, C., Xie, H. Hinz, J. and Wise, Sr., J.P. The Impact of Homologous Recombination Repair Deficiency on Depleted Uranium Clastogenicity in Chinese Hamster Ovary Cells: XRCC3 Protects Cells from Chromosome Aberrations, but Increases Chromosome Fragmentation. Mutation Research, 762: 1-9, 2014. We found that loss of XRCC3 altered the degree of DU-induced chromosome damage. At 0.5 ug/cm^2 uranium trioxide, XRCC3-deficient cells exhibited more chromosome damage than the wild-type and XRCC3-complemented cells, but as the uranium trioxide concentration increased, more chromosome damage was observed in the XRCC3-proficient cells (Figure 48 A,B). Closer inspection of the data shows that the different response observed between doses for XRCC3-deficient cells was due to chromosome fragmentation. Specifically, we observed a dramatic increase in chromosome fragmentation after exposure to 5 and 10 ug/cm^2 uranium trioxide in HR-proficient cells (AA8 and 1SFwt8), but this aberration was not present in XRCC3-deficient cells (irs1SF). If we exclude this particular aberration from the analysis, then, the data show that DU induces more chromosome damage in XRCC3-deficient (irs1SF) at all doses compared to HR-proficient cells (AA8 and irs1SF) (Figure 48 C,D). Specific aspects concerning the chromosome fragmentation data are discussed in more detail below

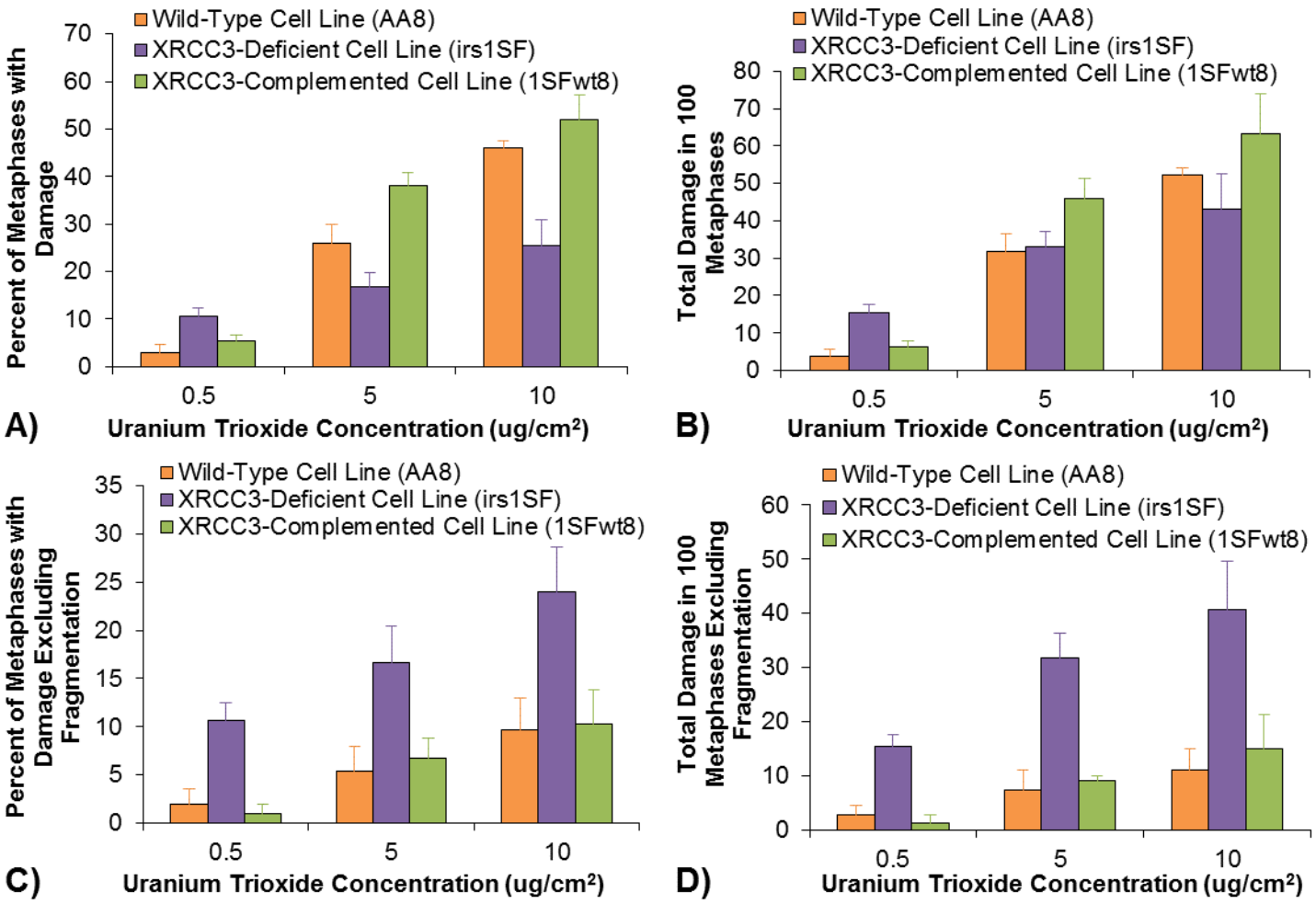

Figure 48. Loss of XRCC3 Alters DU-Induced Clastogenicity. This figure shows that exposure to DU for 24 h induced a concentration-dependent increase in genotoxicity in the XRCC3 series of cell lines. A) At 0.5 ug/cm^2 uranium trioxide, XRCC3-deficient cells (irs1SF) exhibited more metaphases with damage while at higher concentration, uranium trioxide induced less metaphases with damage in XRCC3-deficient cells (irs1SF) compared to the parental (AA8) and XRCC3-complemented cells (1SFwt8). Control values for AA8, irs1SF and 1SFwt8 were 3.3, 21.3 and 6.7 percent of metaphases with damage, respectively and controls were subtracted from treated values. B) Exposure 0.5 ug/cm^2 uranium trioxide induce more damaged chromosomes in XRCC3-deficient cells (irs1SF) compared to the parental (AA8) and XRCC3-complemented cells (1SFwt8), but at higher doses, total chromosome damage levels were similar for all three cell lines. Control values for AA8, irs1SF and 1SFwt8 were 3.3, 21.3 and 6.7 damaged chromosomes, respectively and controls were subtracted from treated values. C) When chromosome fragmentation was excluded from the analysis, uranium trioxide induced more metaphases with damage in XRCC-deficient (irs1SF) cells compared to wild-type (AA8) and XRCC3-complemented (1SFwt8) cells at all doses. Control values for AA8, irs1SF and 1SFwt8 were 3.3, 21.3 and 6.7 percent of metaphases with damage, respectively and controls were subtracted from treated values. D) Excluding chromosome fragmentation, uranium trioxide induced more total chromosome damage in XRCC-deficient (irs1SF) cells compared to wild-type (AA8) and XRCC3-complemented (1SFwt8) cells at all doses. Control values for AA8, irs1SF and 1SFwt8 were 3.3, 21.3 and 6.7 damaged chromosomes, respectively and controls were subtracted from treated values. Data represent an average of at least 3 experiments +/- standard error of the mean.

The XRCC3 series revealed an interesting trend in the spectrum of damage. XRCC3-deficient cells exhibited more chromosome breaks and fusions and little to no chromosome fragmentation compared to XRCC3-proficient cells (Figure 49). For example, exposure to 10 ug/cm^2 induced 31 breaks, 13 fusions and only 2 fragmented chromosomes in 100 metaphases in XRCC3-deficient cells whereas wild-type and XRCC3-complemented cells exhibited 11 and 14 breaks, 0 and 1 fusion and 41 and 48 fragmented chromosomes in

100 metaphases, respectively. Chromatid lesions were the most common breaks observed and chromatid exchanges were the most common form of fusion. Thus, XRCC3 protects cells against simple chromosome breaks and complex fusions after DU exposure and also plays a role in DU-induced fragmentation of the X chromosome.

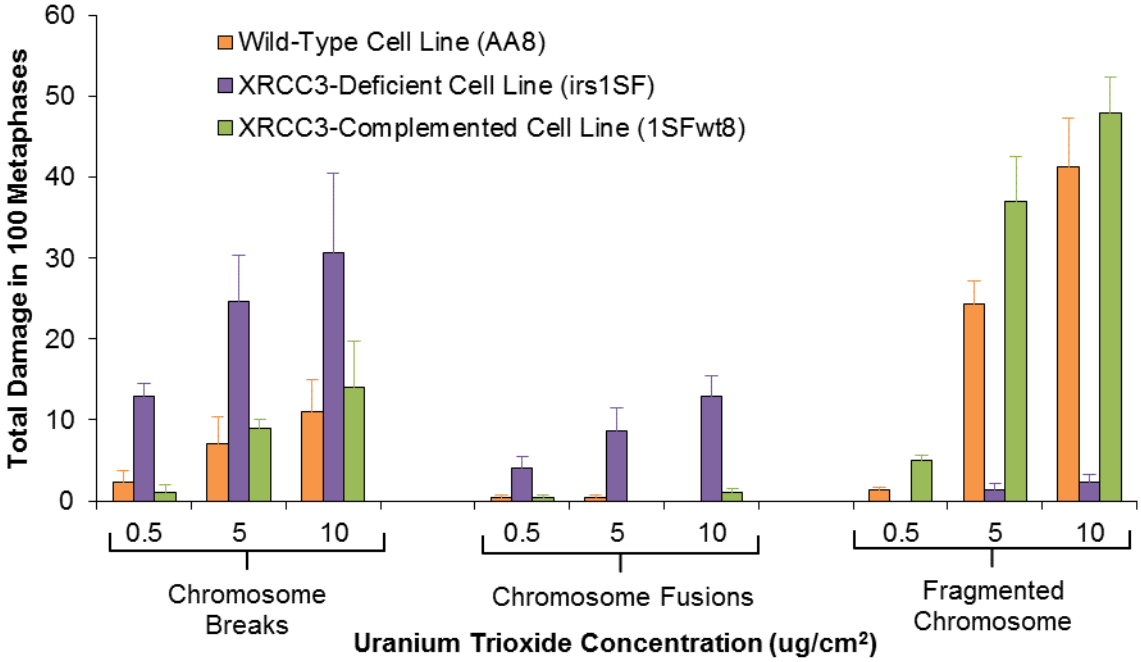

Figure 49. XRCC3-Deficient Cells Exhibit an Altered Chromosome Damage Spectrum After DU Exposure. This figure shows that loss of XRCC3 alters the spectrum of chromosome damage observed after DU exposures. XRCC3-deficient cells (irs1SF) exhibited more chromosome breaks and fusions and less chromosome fragmentation after a 24 h exposure to uranium trioxide exposure compared to wildtype (AA8) and XRCC3-complemented (1SFwt8) cells. Control values for AA8, irs1SF and 1SFwt8 were 3, 24 and 12 chromosome breaks and 0, 2 and 0 chromosome fusions, respectively and controls were subtracted from treated values. No fragmented chromosomes were observed in the controls. Data represent an average of at least 3 experiments +/- standard error of the mean.

We also investigated the role of RAD51D in DU-induced chromosome damage. In contrast to XRCC3, loss of RAD51D did not affect DU-induced chromosome damage with RAD51D-deficient cells exhibiting similar percent of metaphases with damage and total damage compared to the wild-type, parental and RAD51D-complemented cells (Figure 50). When we assessed the spectrum of chromosome damage, we found that all four cells exhibited a similar concentration-dependent increase in breaks and chromosome fragmentation and minimal to no chromosome fusions were observed after exposure to DU (Figure 51). For example, 5 ug/cm^2 uranium trioxide induced 7, 11, 13 and 10 chromosome breaks and 24, 34, 34 and 34 fragmented chromosomes in 100 metaphases in wild-type (AA8), parental (51D1 lox), RAD51D-deficient (51D1) and RAD51D-complemented (51D1.3) cells, respectively. Chromosome fragmentation was the most prevalent aberration observed and occurred in the X chromosome. Chromatid and isochromatid lesions were the most common form of break. Thus, RAD51D, unlike XRCC3, does not appear to protect cells from DU-induced chromosome damage. Future work is aimed at investigating the mechanism of XRCC3-dependent chromosome fragmentation after DU exposure.

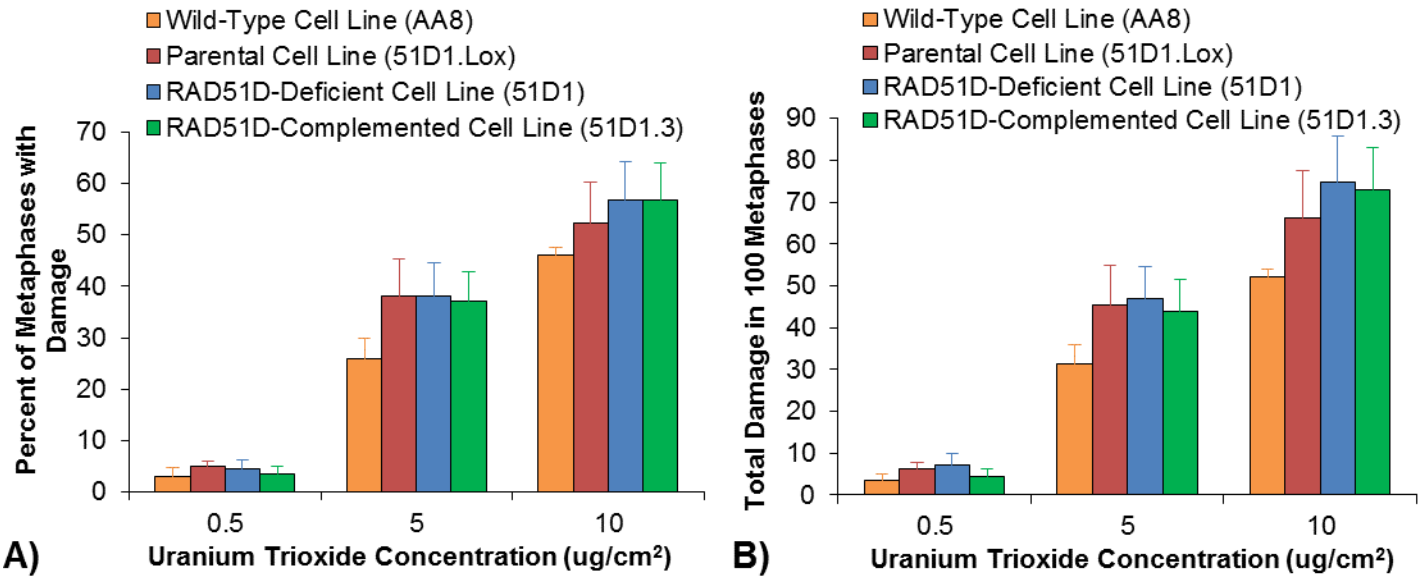

Figure 51. Loss of RAD51D Does Not Affect DU-Induced Clastogenicity. This figure shows that a 24 h DU exposure induced a concentration-dependent increase in chromosome damage in the RAD51D series of cell lines. A) Similar percentages of metaphases with damage were observed in parental cells (AA8 and 51D1 lox), RAD51D-deficient cells (51D1) and RAD51D-complemented cells (51D1.3) after DU exposure. Control values for AA8, 51D1 lox, 51D1 and 51D1.3 were 3.3, 4.6, 6.8 and 5.8 percent of metaphases with damage, respectively and controls were subtracted from treated values. B) Parental cells (AA8 and 51D1 lox), RAD51D-deficient cells (51D1) and RAD51D-complemented cells (51D1.3) exhibited similar levels of total chromosome damage after DU exposure. Control values for AA8, 51D1 lox, 51D1 and 51D1.3 were 3.7, 5.2, 6.8 and 6 damaged chromosomes, respectively and controls were subtracted from treated values. Data represent an average of at least 3 experiments +/- standard error of the mean.

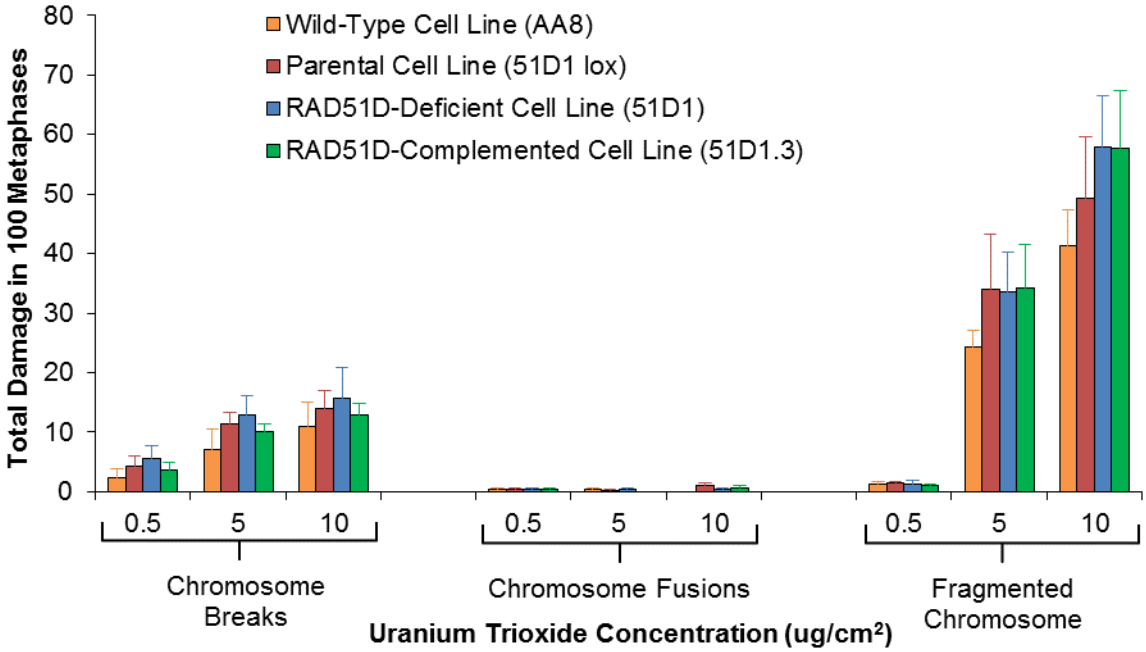

Figure 52. RAD51D Deficiency Does Not Alter the Spectrum of Damage Induced After DU Exposure. This figure shows that loss of RAD51D does not alter the spectrum of chromosome damage observed after DU exposures. Parental cells (AA8 and 51D1 lox), RAD51D-deficient cells (51D1) and RAD51D-complemented cells (51D1.3) exhibited similar levels of total breaks, fusions and fragmented chromosomes after DU exposure. Chromosome breaks include chromatid breaks and gaps, isochromatid breaks and gaps, acentric fragments and double minutes. Chromosome fusions include chromatid exchanges, rings and dicentrics.

Control values for AA8, 51D1 lox, 51D1 and 51D1.3 were 3.3, 4.8, 6.8 and 5.8 chromosome breaks and 0, 0.4, 0 and 0.2 chromosome fusions, respectively and controls were subtracted from treated values. No fragmented chromosomes were observed in the controls. Data represent an average of at least 3 experiments +/- standard error of the mean.

This work was published: Holmes, A.L., Joyce, K., Falank, C., Xie, H. Hinz, J. and Wise, Sr., J.P. The Impact of Homologous Recombination Repair Deficiency on Depleted Uranium Clastogenicity in Chinese Hamster Ovary Cells: XRCC3 Protects Cells from Chromosome Aberrations, but Increases Chromosome Fragmentation. Mutation Research, 762: 1-9, 2014. We showed for the first time that XRCC3, but not RAD51D, is involved in protecting cells against DU-induced chromosome damage and chromosome instability while also playing a role in inducing fragmentation of the X chromosome. These data implicate HR repair as one repair pathway involved in repair of DU-induced DNA double strand breaks and also suggest that it may be responsible for DU-induced chromosome fragmentation.

5. Specific Aim 4. Characterize Metal Nanoparticle- and Microparticle-Induced Chromosome Instability in Human Lung Cells

5.1. Nanoparticle-Induced Chromosome Instability

Similar to our genotoxic studies, we found that exposure to the highest achievable concentrations of bare silver, functionally modified silver, or gold nanoparticles did not induce aneuploidy (Figure 53).

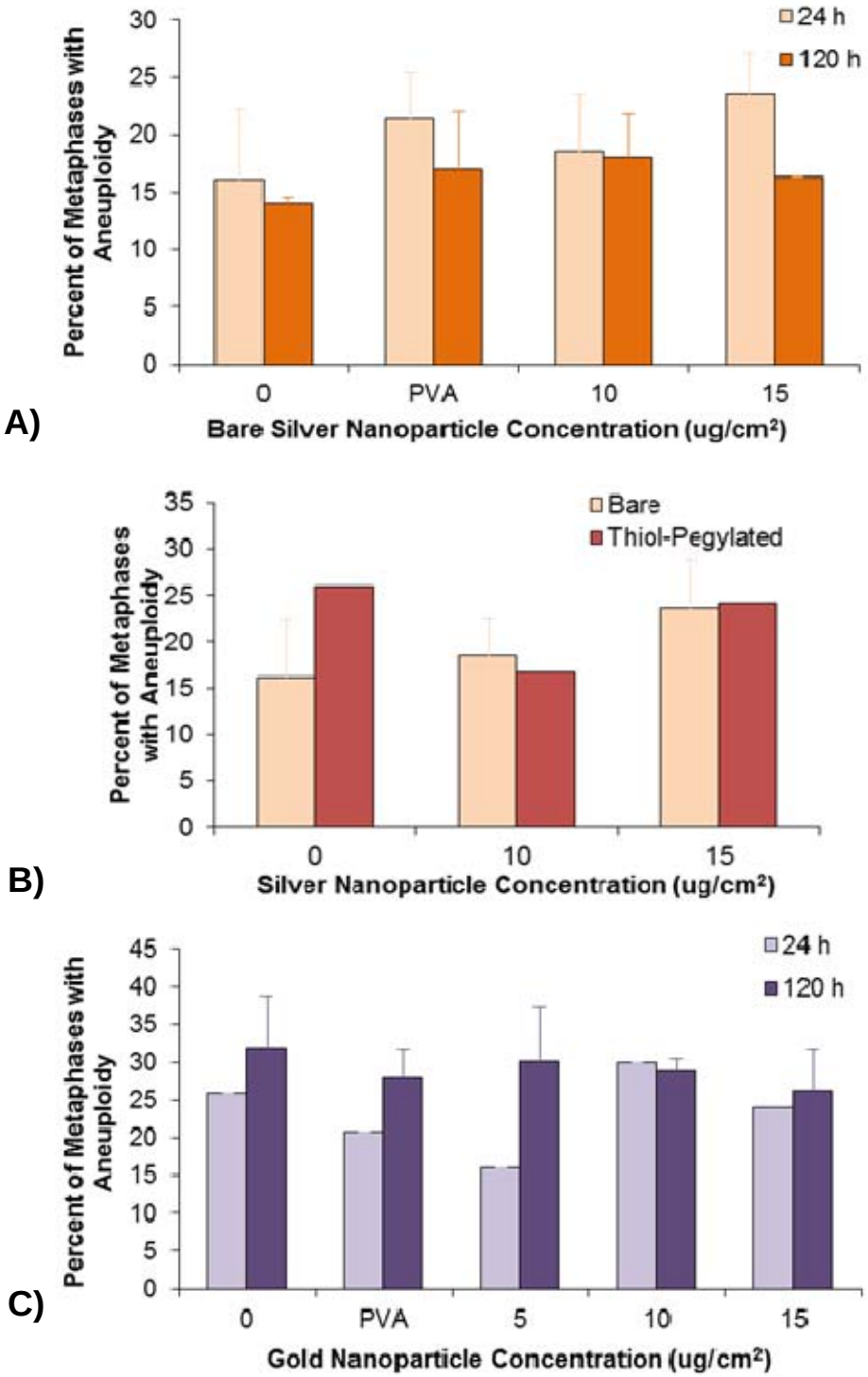

Figure 53. Aneugenic Effects of Silver and Gold Nanoparticles in Human Lung Cells. This figure shows that exposure to silver and gold nanopartilces did not induce aneuploidy. **A)** Bare silver nanoparticles for 24 or 120 h. Data represent the average of 2 or 3 experiments +/- the standard error of the mean. **B)** PEGylated silver nanoparticles did not induce aneuploidy after 24 h exposure. Data represent an average of 3 or 4 experiments +/- the standard error of the mean for bare and 1 experiment for PEGylated. **C)** Bare gold nanoparticles for 24 or 120 h did not induce aneuploidy. Data represent 1 experiment for 24 h or the average of 2 or 3 experiments +/- the standard error of the mean for 120 h.

5.2. Metal-on-Metal Hip Implant Particle-Induced Chromosome Instability

We assessed the effects of CoCrMo nanoparticles on chromosome number. Data indicate that chronic exposure to CoCrMo nanoparticles do not induce aneuploidy in human urothelial cells (Figure 54A). We also

found that nanoparticles generated from an actual hip implant also do not induce aneuploidy in human urothelial cells after 24 h exposure (Figure 54B).

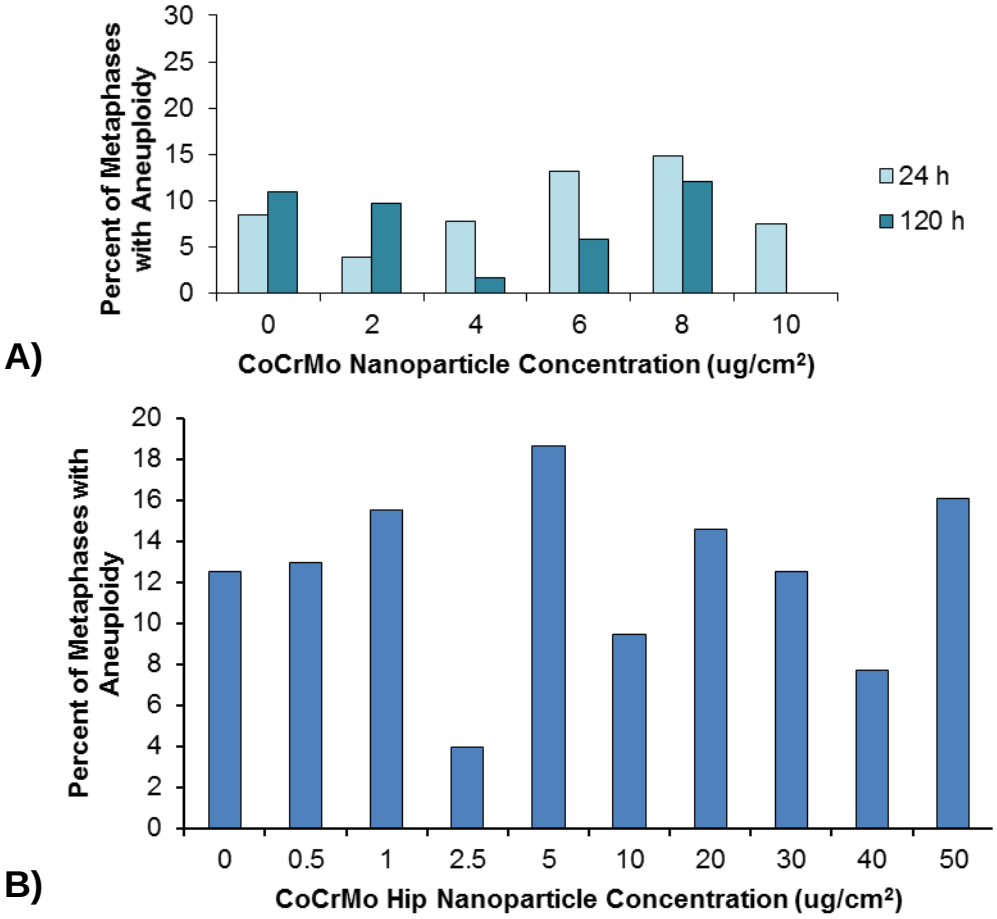

Figure 54. Aneugenic Effects of CoCrMo Nanoparticles in Human Urothelial Cells. This figure shows that exposure to CoCrMo nanoparticles and CoCrMo hip nanoparticles does not induce aneuploidy. A) CoCrMo nanoparticles, 24 and 120 h. Data represent 1 experiment for each time point. **B)** CoCrMo nanoparticles generated from an actual hip implant, 24 h only. Data represent 1 experiment.

5.3. Metal Microparticles of Military Concern-Induced Chromosome Instability

We also assessed the aneugenic effects of micron-sized metal particles. We found that a 24 or 120 h exposure to nickel sulfide induced minimal to no increase in aneuploidy in human lung fibroblast or epithelial cells (Figure 55). For example, exposure to 5 ug/cm^2 nickel sulfide for 24 h induced aneuploidy in 16 percent of metaphases in human lung fibroblasts. Background aneuploidy was 11 percent of metaphases with aneuploidy (Figure 55 A). Chronic exposure also induced no increase in aneuploidy with concentrations at or above 2.5 ug/cm^2 nickel sulfide inducing no metaphases in lung fibroblast cells (Figure 50 A). In human lung epithelial cells, exposure to 5 ug/cm^2 induced 31 and 28 percent of metaphases with aneuploidy after 24 or 120 h, respectively, compared to background levels of 19 percent of metaphases with aneuploidy (Figure 55 B).

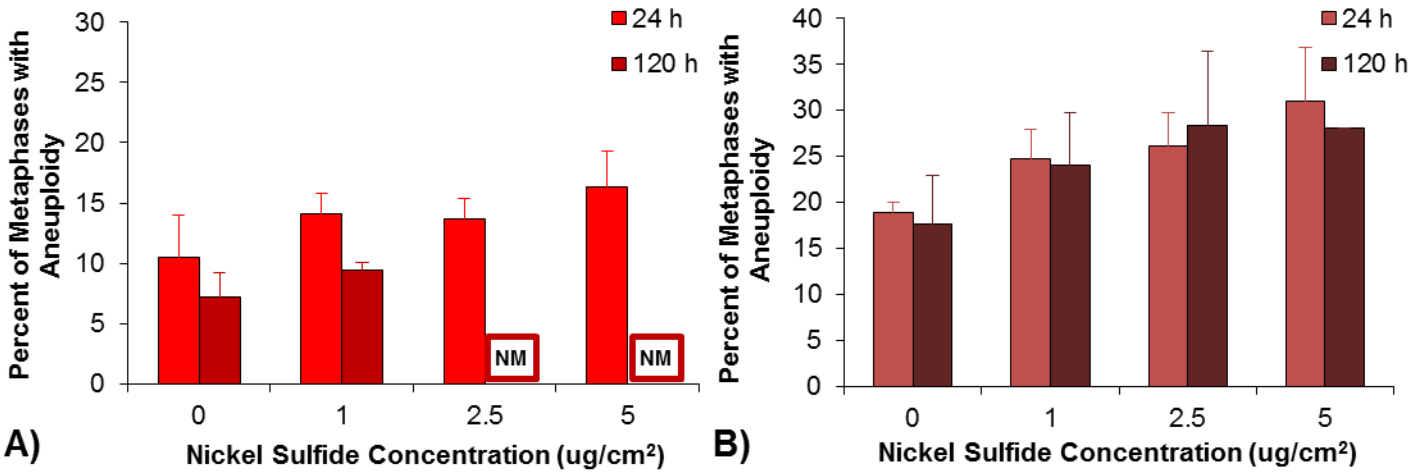

Figure 55. Aneugenic Effects of Nickel Sulfide in Human Lung Cells. This figure shows that exposure to nickel sulfide for 24 or 120 h induced a small increase in aneuploidy in human lung fibroblast and epithelial cells. A) Human lung fibroblast cells. Exposure to 2.5 or 5 ug/cm^2 nickel sulfide for 120 h induced no metaphases (NM). B) Human lung epithelial cells. Data represent the average of 2 or 3 experiments +/- the standard error of the mean.

Particulate nickel induces transformation in vitro as measured by the foci formation assay. This data was finalized and published: Holmes, A.L., The, T., Thompson, K., Mason, M., Kandpal, S., Zheng, T., and Wise, Sr., J.P. Chronic Exposure to Particulate Nickel Induces Neoplastic Transformation in Human Lung Epithelial Cells. Toxics, 1(1): 46-59, 2013. doi:10.3390/toxics1010046. Briefly, we found that nickel subsulfide induced concentration- and time-dependent increases in both cytotoxicity and genotoxicity in human lung epithelial cells (BEP2D). Chronic exposure to nickel subsulfide readily induced cellular transformation, inducing 2.55, 2.9 and 2.35 foci per dish after exposure to 1, 2.5 and 5 µg/cm^2 nickel subsulfide, respectively. Sixty-one, 100 and 70 percent of the foci isolated from 1, 2.5, and 5 µg/cm^2 nickel subsulfide treatments formed colonies in soft agar and the degree of soft agar colony growth increased in a concentration-dependent manner. We concluded that chronic exposure to particulate nickel induces genotoxicity and cellular transformation in human lung epithelial cells.

We also investigated the aneugenic effects of cobalt compounds on human lung cells. Particulate cobalt induced a small concentration- and time-dependent increase in aneuploidy in human lung fibroblast cells (Figure 56 A). For example, the percentage of metaphases with aneuploidy after exposure to 1 ug/cm^2 of cobalt oxide increased from 16 percent in the control to 21 percent. Chronic exposure (120 h) to cobalt oxide showed a significantly higher percent of aneuploidy compared to acute exposure (24 h). For example, exposure to 0.1, 0.5, and 1 ug/cm^2 of cobalt oxide for 24 h resulted in approximately 15, 19, and 21 percent of metaphases with aneuploidy, respectively; while, exposure for 120 h resulted in approximately 19, 31, and 34 percent of metaphases with aneuploidy at these same concentrations.

Soluble cobalt also induced a small concentration- and time-dependent increase in aneuploidy in human lung fibroblast cells (Figure 56 B). Chronic exposure (120 h) to cobalt chloride showed a similar percent of metaphases with aneuploidy compared to acute exposure (24 h). For example, exposure to 25, 50, 100, and 175 uM of cobalt chloride for 24 h resulted in 8, 11, 12, and 18 percent of metaphases with aneuploidy cells, respectively; and, exposure for 120 h resulted in approximately 14, 14, 14, and 18 percent of metaphases with aneuploidy at these same concentrations.

We also considered co-exposures of nickel and cobalt in human lung epithelial cells. Cobalt oxide did not increase the aneugenic effect of nickel sulfide after 120 h treatment (Figure 57).

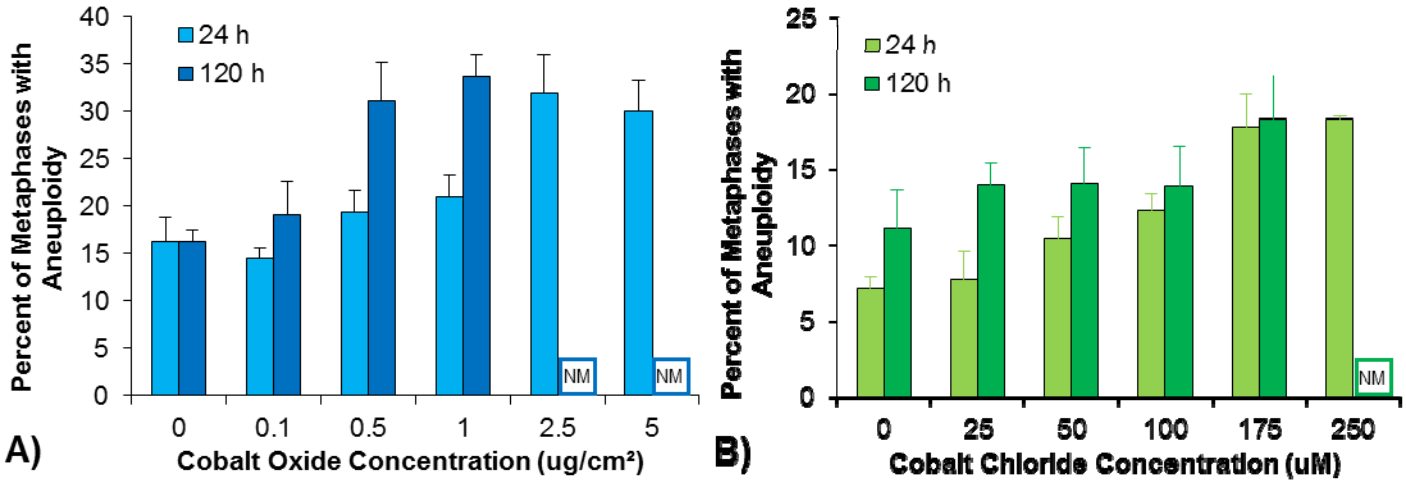

Figure 56. Aneugenic Effects of Cobalt in Human Lung Cells. This figure shows that exposure to cobalt for 24 or 120 h induces aneuploidy in human lung fibroblast cells. A) Cobalt oxide. No metaphases (NM). B) Cobalt chloride. No metaphases (NM). Data represent the average of 3 experiments +/- the standard error of the mean.

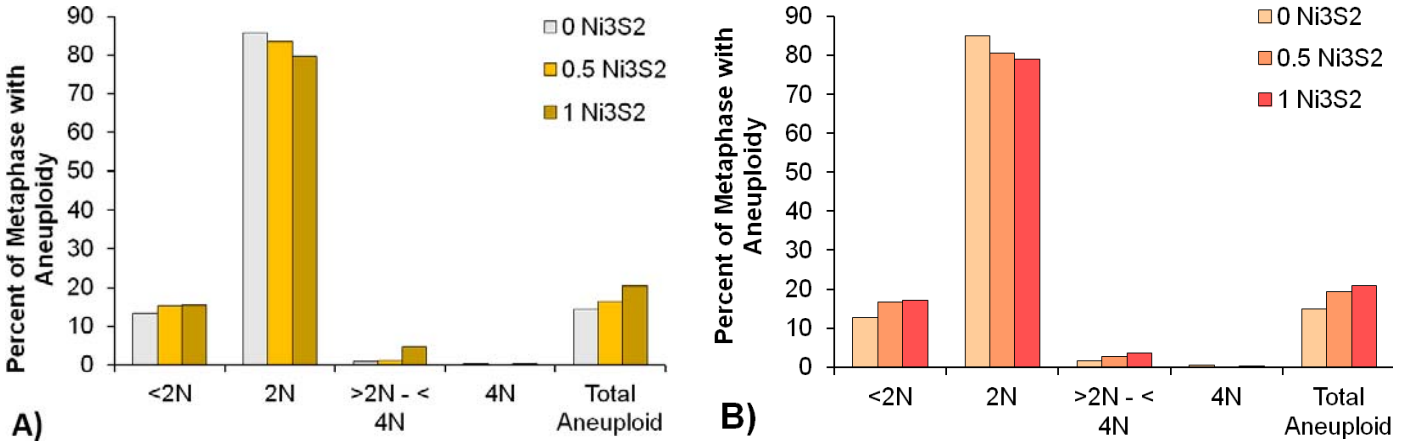

Figure 57. Aneugenic Effects of Co-Treatment with Nickel and Cobalt in Human Lung Cells. This figure shows that cobalt does not exacerbate the anuegenic effect of nickel after 120 h treatment in human lung epithelial cells. A) Nickel sulfide treatment alone. B) Nickel treatment with 0.1 ug/cm^2 cobalt oxide. Data represent the average of 1-2 experiments.

Previously, we discovered that more chronic exposures to DU induced hypercondensation of metaphase chromosomes. For example, exposure to 2.5 ug/cm^2 uranium trioxide for 24, 48 or 72 h induced 3, 5 or 18 percent of metaphases with hypercondensed chromosomes, respectively. We investigated the mechanism of DU-induced hypercondensation. One hypothesis was that DU is prolonging mitosis allowing metaphase chromosomes to hypercondense. We investigated this hypothesis using the time-lapse video microscope to measure the length of mitosis (Figure 58). We found that chronic exposure to DU increased the length of mitosis (Figure 59). Average mitotic length in control cells was approximately 25 minutes while exposure to 2 ug/cm^2 uranium trioxide for 72 h increased mitotic length to 30 minutes (Figure 59 A). When we classified mitotic length into four categories, we found that chronic exposure to DU decreased the percentage of cells with mitosis lasting less than 25 minutes and increased the percentage of cells with mitosis lasting 25-34 and 35-44 (Figure 59 B). These data suggest that DU increases mitotic length. Future work is aimed at continuing to investigate the mechanism of DU-induced chromosome hypercondensation.

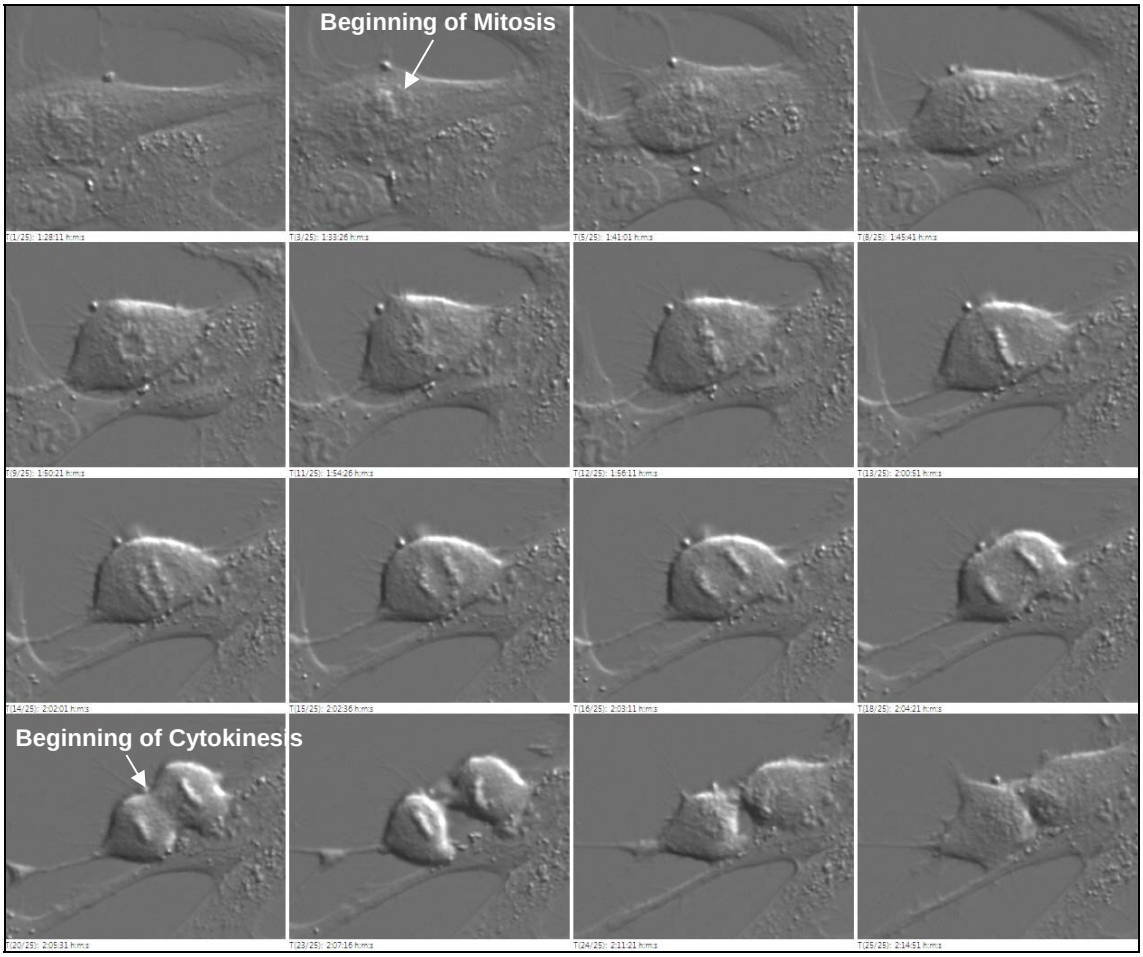

Figure 58. Time Lapse Image of Mitotic Progression. This figure represents a series of pictures showing normal mitotic progression in a control cell starting with nuclear envelope breakdown in prophase, chromosomes lining up along the metaphase plate in metaphase, chromosomes segregating to two poles in anaphase and telophase, and lastly cleavage furrow formation and ultimately cytokinesis. The duration of mitosis was 33 minutes.

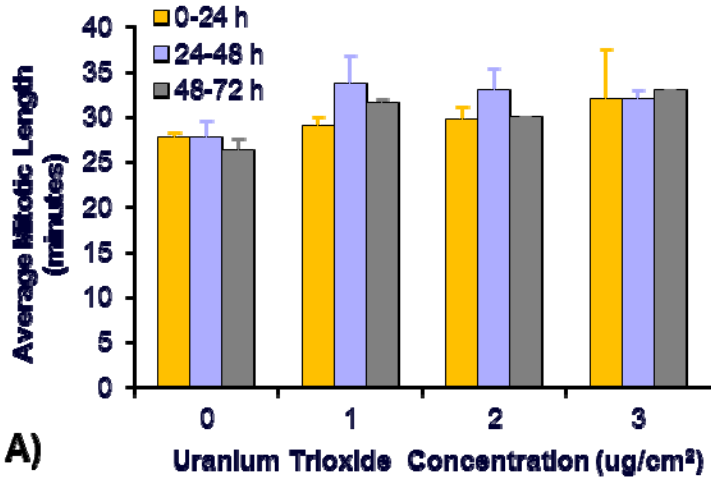

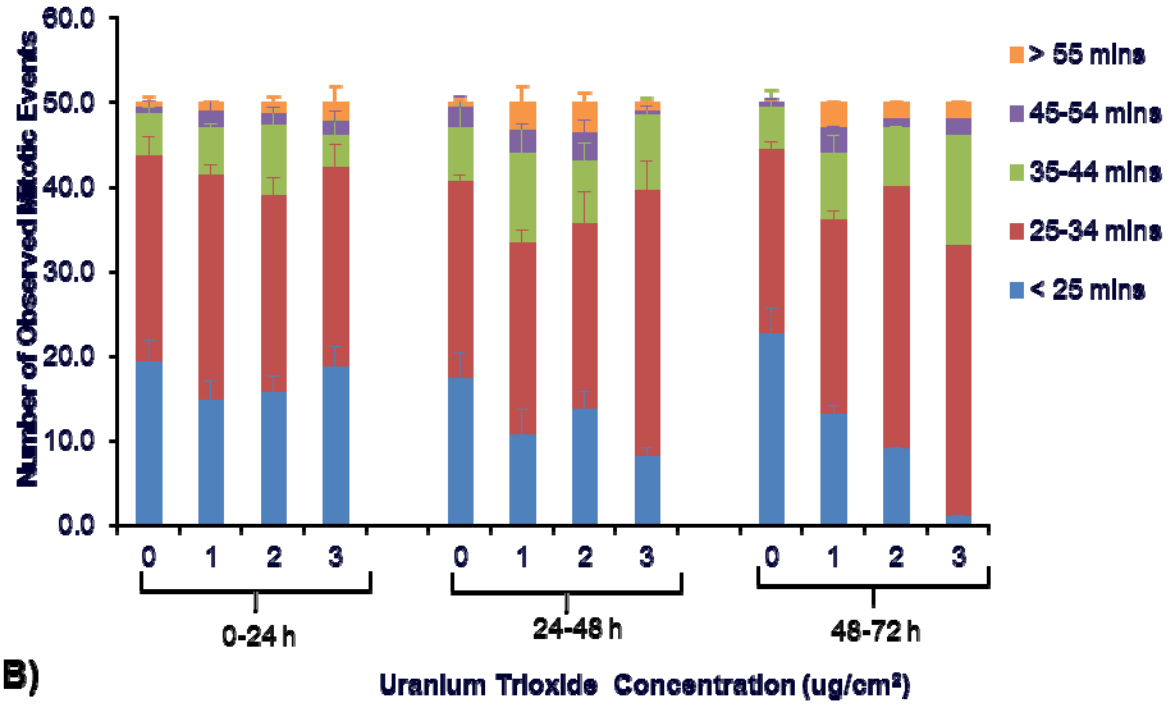

Figure 59. Mitotic Length after DU Exposure. This figure shows that DU increases mitotic length. A) DU increased average mitotic length. B) DU decreased the percentage of cells undergoing mitosis in less than 25 minutes but increased the percent of cells with mitosis lasting 25-34 and 35-44 minutes. Data represent three experiments.

6. Specific Aim 5. Compare Silver and Gold Nanoparticle-Induced Effects in Human Lung Cells

In general effects of both silver and gold nanoparticles were found to be negative. The only comparison we were able to draw directly was between bare gold and silver nanoparticles (Figure 60). We were unable to achieve high enough stock concentrations of the functionalized gold nanoparticles for further cytotoxicity comparisons. All genotoxicity and aneuploidy data for gold and silver nanoparticles were negative.

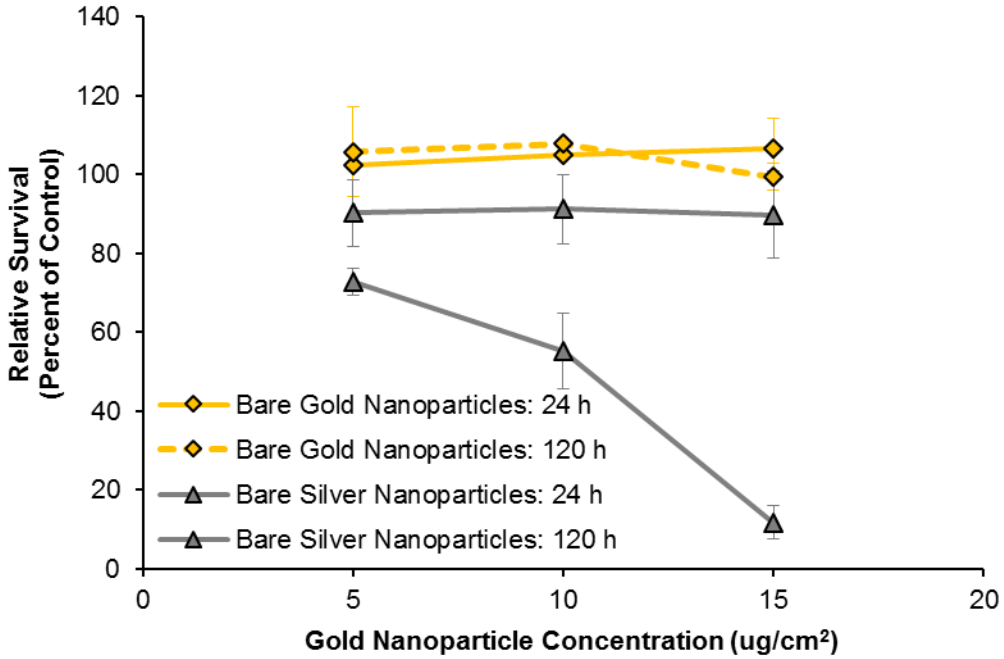

Figure 60. Comparison of Bare Gold and Silver Nanoparticles. This figure shows that only the 120 h treatment time for silver nanoparticles induced cytotoxicity.

7. New Specific Aim 6. Assessment of Metal Levels in Whale Skin Biopsies from the Gulf of Mexico

One concern to whales and marine life in the Gulf of Mexico is the leaching of metals into the marine environment from unexploded ordinances. We launched a research expedition to collect sperm and Bryde's whale biopsies in the Gulf of Mexico to characterize the impact of metals on these whales. To date, we have spent approximately 9 months at sea spanning over three years and have collected 241 whale biopsies. Previously, we analyzed metal levels in 42 sperm whales collected in 2010. This data was published: Wise, Jr., J.P., Wise, J., Wise, C.F., Wise, S.S., Gianios, Jr. ,C., Xie, H., Thompson, W.D., Perkins, C. Falank, C. and Wise, Sr., J.P. Concentrations of the Genotoxic Metals, Chromium and Nickel, in Whales, Tarballs, Oil Slicks and Released Oil from the Gulf of Mexico in the Immediate Aftermath of the Deepwater Horizon Oil Crisis: Is Genotoxic Metal Exposure Part of the Deepwater Horizon Legacy? Environmental Science and Technology, 48(5): 2997–3006 2014. DOI: 10.1021/es405079b. In addition, we have results on 91 sperm whale skin biopsies collected in 2011 and 2012. Data for all metals are shown in Figure 61 and for specific toxic metals of concern found in oil in Figure 62 for sperm whales, respectively.

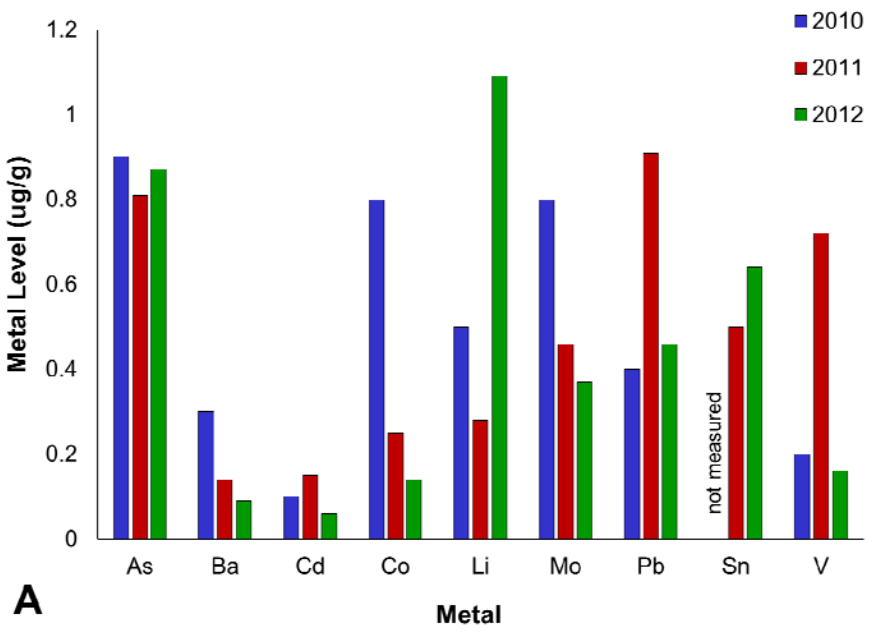
2010
2011
2012
Metal Level (ug/g)
1.2
1
0.8
0.6
0.4
0.2
0
not measured
As
Ba
Cd
Co
Li
Mo
Pb
Sn
V
Metal

A

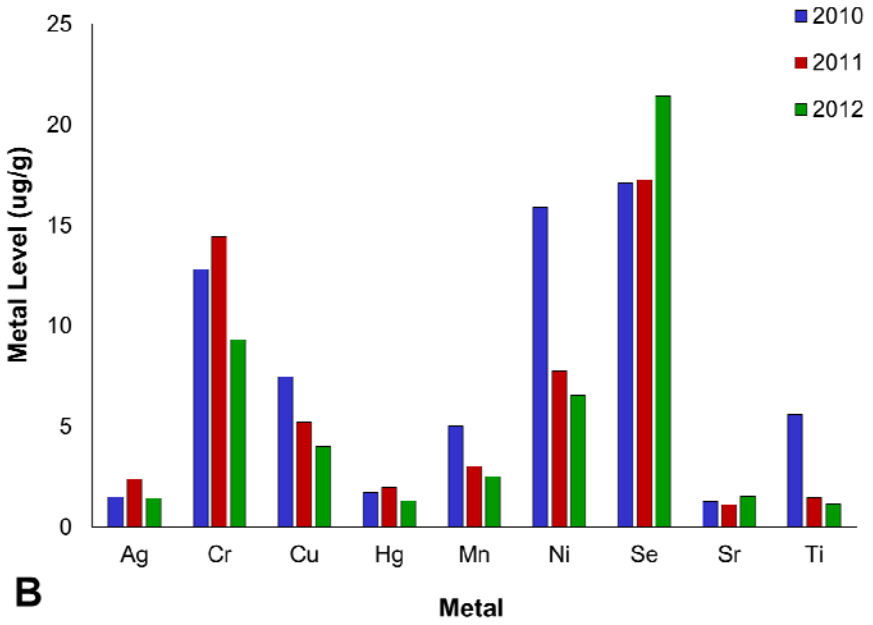
2010
2011
2012
Metal Level (ug/g)
25
20
15
10
5
0
Ag
Cr
Cu
Hg
Mn
Ni
Se
Sr
Ti
Metal

B

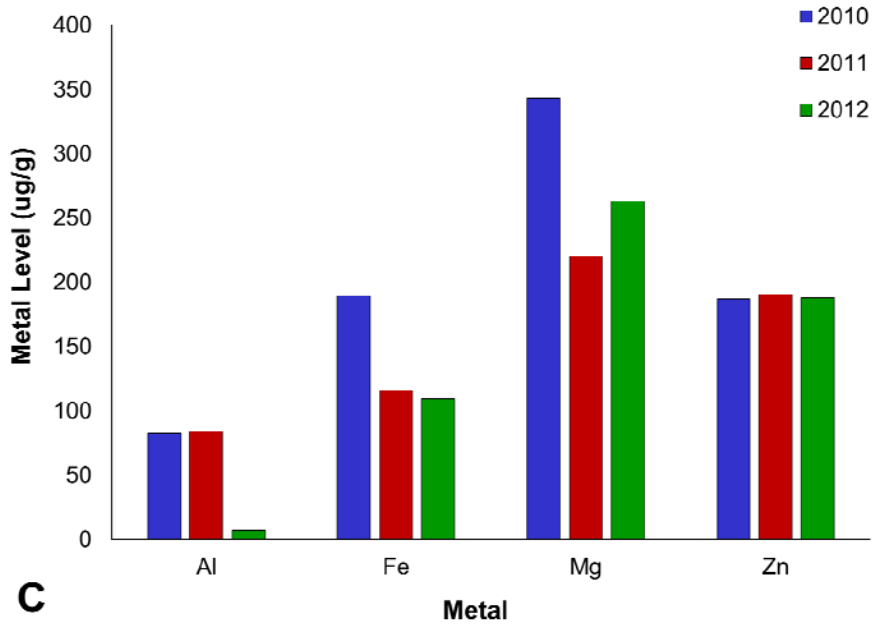
2010
2011
2012
Metal Level (ug/g)
400
350
300
250
200
150
100
50
0
Al
Fe
Mg
Zn
Metal

C

Figure 61. Average Metal Levels in Sperm Whales from the Gulf of Mexico in 2010, 2011, and 2012. This figure shows the average levels of various metals found in sperm whales in the northern Gulf of Mexico across 3 years. Data represent 40 individual animals in 2010; 53 individual animals in 2011; and 47 individual animals in 2012.

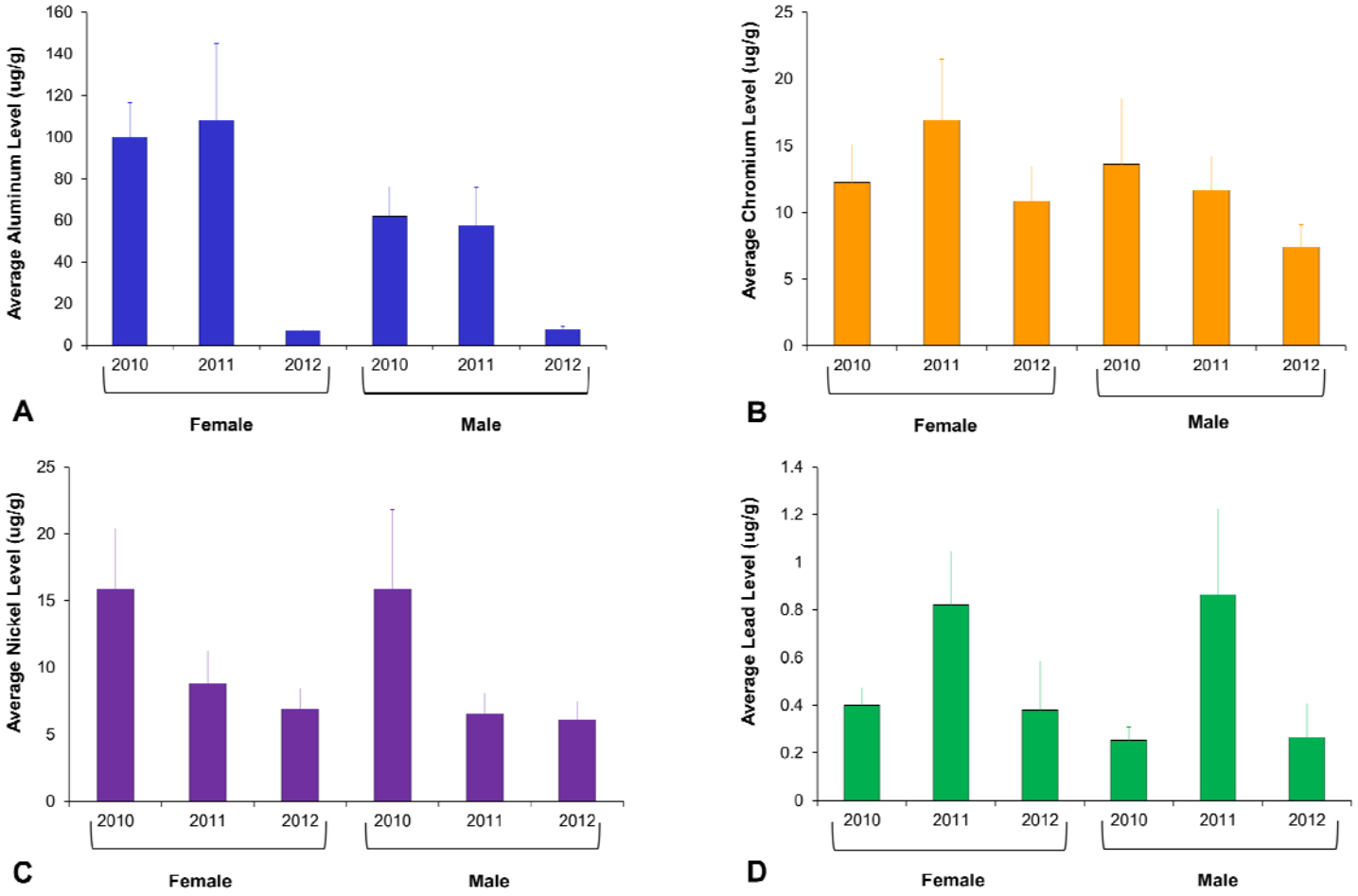

Figure 62. Levels of Toxic Metals in Male and Female Sperm Whales. This figure shows that most levels of toxic metals decreased in subsequent years following the Deepwater Horizon Event. Lead levels were higher in 2011.